The Thesis Committee for Christopher Paul Armstrong
Certifies that this is the approved version of the following thesis:

3D Seismic Geomorphology and Stratigraphy of the Late Miocene to Pliocene Mississippi River Delta: Fluvial Systems and Dynamics

APPROVED BY

SUPERVISING COMMITTEE:

Co-supervisor: _____

David Mohrig

Co-supervisor: _____

Ronald Steel

_____

Wonsuck Kim

3D Seismic Geomorphology and Stratigraphy of the Late Miocene to Pliocene Mississippi River Delta: Fluvial Systems and Dynamics

by

Christopher Paul Armstrong, B.S.

Thesis

Presented to the Faculty of the Graduate School of

The University of Texas at Austin

in Partial Fulfillment

of the Requirements

for the Degree of

Master of Science in Geological Sciences

The University of Texas at Austin

May 2012

Acknowledgements

I would like to thank David Mohrig, Ron Steel, and Wonsuck Kim for giving so freely of their time, guidance, and knowledge as well as Thomas Hess for providing valuable geophysical insights and many hours of software and data loading help and advice. I am most thankful to Anjali Fernandes for her mentoring and support and to all the students in my co-advisors' research groups for their feedback and support. For funding, I would like to thank The University of Texas at Austin Graduate School, The Jackson School of Geosciences, the RioMAR Research Consortium, and The National Center for Earth-surface Dynamics. I would also like to thank WesternGeco® for generously donating the seismic dataset, PaleoData®, Inc. for providing biostratigraphic data, and the Louisiana Department of Natural Resources for making well log data available. Additionally, this project would not have been possible without the generous license donations of Seismic Micro-Technology's (SMT®) Kingdom Suite interpretation software, Landmark® GeoProbe interpretation software, and CGG Veritas Hampson-Russel® petrophysical software.

Abstract

3D Seismic Geomorphology and Stratigraphy of the Late Miocene to Pliocene Mississippi River Delta: Fluvial Systems and Dynamics

Christopher Paul Armstrong, M.S. Geo.Sci.

The University of Texas at Austin, 2012

Supervisors: David Mohrig and Ronald Steel

This study uses a 1375 km^2 3D seismic dataset located in the late Miocene to Pliocene Mississippi River Delta in order to investigate the external characteristics, lithology, and evolution of channelized deposits within the seismic survey. Fluvial thicknesses range from about 11 m to 90 m and widths range from about 100 m to 31 km. Channel fill can be generalized as sandy with low impedance and high porosity (~ 35%), though heterogeneity can be high. Three distinct fluvial styles were recognized: incised valleys, channel-belts, and distributive channel networks. Fluvial styles were interpreted as a result of changes in sea-level and a speculative late Miocene to Pliocene Mississippi River Delta sea-level curve constructed using these relationships. Additionally, a characteristic interval between the major changes in fluvial style was found. These fluvial systems interact with and are affected by other elements in the landscape. Growth faults in particular are common within the survey area; however, the dynamic between fluvial systems and growth fault related subsidence has been poorly understood and so was also a focus of this project. Previous work as well as this study found little evidence that growth faults are able to affect the course or geometry of the majority of small (with most < 500 m in width and < 20 m in depth) channels. However, the relationship between growth faults and larger scale channel-belt systems (between 1 km and 5 km in width and > 25 m in depth) has not been previously evaluated in this area. In contrast to the majority

of small distributary channels found within the survey, channel-belts appear to be steered by growth faults. Fluvial response or insensitivity to fault induced subsidence is related to the relative timescales of avulsion and faulting. Channel-belts are longer lived features than more ephemeral small distributary channels. Channel-belts, due to their relatively low mobility compared to small channels, are more likely to experience punctuated faulting events which results in greater apparent sensitivity to faulting than seen in small channels.

Table of Contents

List of Tables

List of Figures

Chapter 1: Introduction

1.1 Research overview and objectives

This study concerns late Miocene to Pliocene fluvial stratigraphy imaged within a volume of 3D seismic data covering 1375 km^2 of the modern Mississippi River Delta. Two fundamental aspects of fluvial systems within the interval are explored. The first aspect investigated is the planform expression and geometry of paleo-rivers as well and their lithology. The second aspect studied is the effect that spatial variations in subsidence created by growth faults have on these fluvial systems.

The specific goals of this project are threefold. Within the late Miocene to Pliocene interval of the 3D seismic volume, I seek to:

1) Gain a detailed understanding of the external geometry and lithology of fluvial stratigraphy in this interval. External geometry refers to a quantitative description of planform shape including sinuosity, width, and depth over a significant portion of each channelized system. Well log control, seismic inversions, and seismic lithology inferences are used to provide information about the lithology of fluvial fill.

2) Examine the evolution of fluvial styles in order to investigate the repetitive nature of fluvial patterns as well as the extent to which a sea-level signal is recorded by changes in these patterns. Repetitive changes in planform style with time imply an allogenic forcing mechanism. Given the basinward survey location and passive margin setting, sea-level change is likely a primary variable influencing fluvial style. Changes in the style of fluvial systems observed through seismic mapping can be related to sea-level and is combined with biostratigraphic control to construct a 4th order sea-level curve for the late Miocene to Pliocene interval.

3) Determine if local growth faults are able to exert any influence over channelized features. The seismic survey contains about twenty-eight growth faults which create local variations in subsidence rate. Channelized features that cross or come into close proximity with these faults may be affected by the increased subsidence rates near faults. Using seismic data, quantitative relationships between spatial variations in subsidence and changes in the planform or geometry of fluvial systems can be established.

1.2 Geological setting of study area

The 1375 km^2 3D seismic survey is located under Breton Sound, Louisiana, approximately 50 km southeast of the city of New Orleans and 50 km northwest of the edge of the modern Mississippi River Delta (Fig. 1.1).

Figure 1.1: Aerial extent of the Breton Sound 3D seismic survey outlined on the modern Mississippi River Delta surface. Access to this seismic volume was provided by WesternGeco®.

The survey clearly images channelized features within sandstone, siltstone, and mudstone sedimentary fill over a depth range of about 500 m to 2000 m. Biostratigraphic data places the base of this 1500 m interval in the late Miocene and the top in the late Pliocene. Figure 1.2 shows proposed shifts in the depocenter location for this time period.

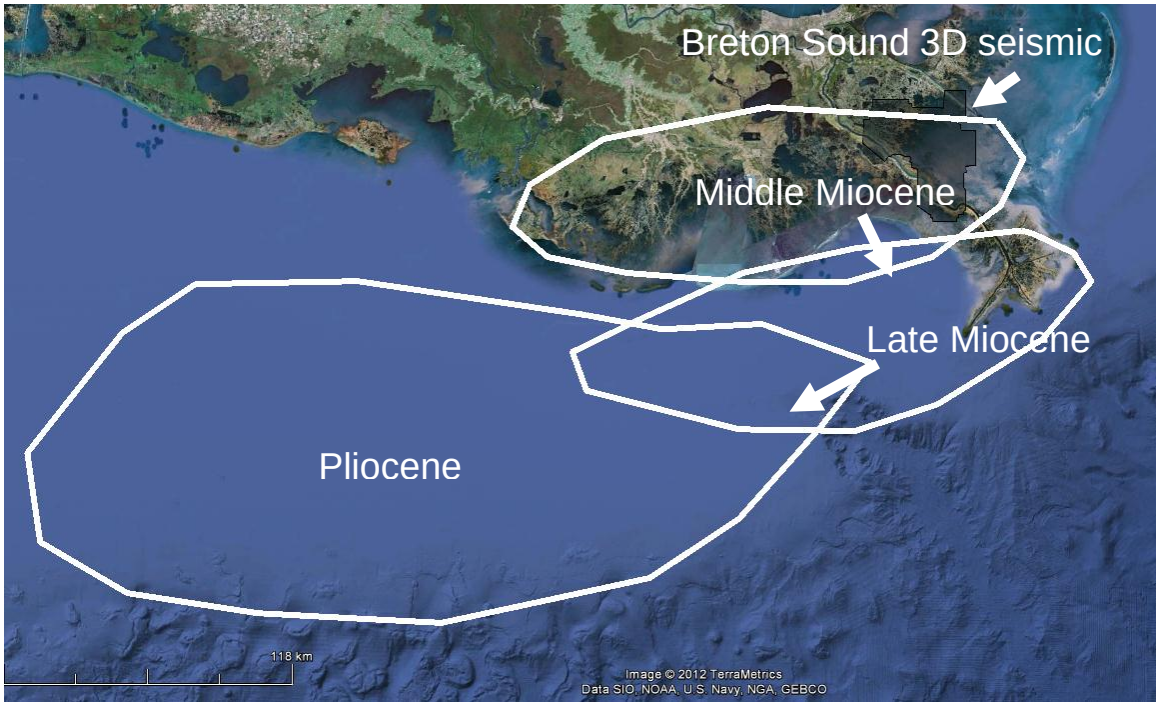

Figure 1.2: Locations of Miocene and Pliocene depocenters (after Salvador, 1991).

From Paleocene to Miocene, several major eastward shifts in fluvial-deltaic systems accompanied by ~ 80 km of progradation occurred. The late Miocene depocenter location near the modern Mississippi River Delta and the persistence of Mississippi River Delta deposition is related to the presence of the Mississippi embayment (Galloway et al., 1991). From the depositional pattern seen in the figure above it is clear that the studied seismic section should record an overall seaward progradation of the Mississippi River Delta system.

The large volumes of terrigenous clastic sedimentation delivered during Miocene through Pliocene times maintained significant growth faulting within the survey. Growth faults are contemporaneous with deposition and have listric concave upwards profiles that flatten with depth and sole out in underlying strata. These faults are a result of gravity driven local instability due to rapid sediment loading and related Louann salt withdrawal (Nelson, 1991). A defining characteristic of growth faults is thickening and down-warping of hanging wall sedimentary successions towards the fault due to increased availability of accommodation and rollover (Nelson, 1991). Figure 1.3 shows growth faults mapped within the upper 1.5 km of the survey.

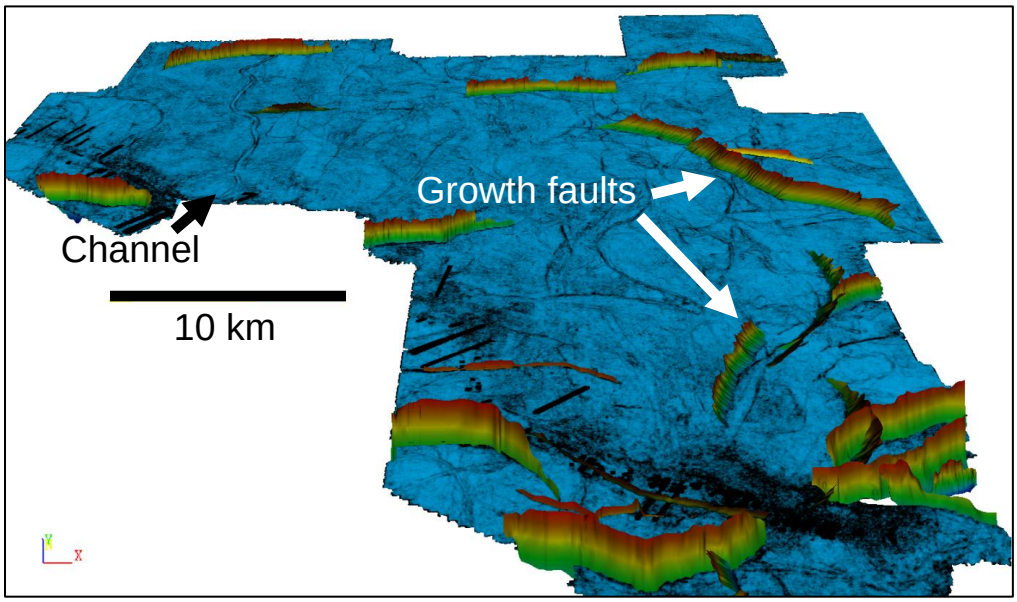

Figure 1.3: A perspective view (looking to the north) of growth faults within the Miocene to Pliocene survey interval (hotter colors are shallower). The blue surface shows outlines of several north-south oriented late Miocene fluvial systems.

The seismic volume images approximately 28 growth faults. Most fault planes are from 8 to 12 kilometers wide, dip either basinward or landward, and have a roughly east-west oriented strike. While the amount of surface displacement that existed on a fault at a specific point in time is unknown, modern fault displacements in the study area can be over 1 m at the surface (Gagliano, 2003). Fault offsets increase with depth to an average maximum value of about 60 m (George, 2008) near the base of the studied stratigraphic interval. A number of the faults imaged in the seismic data appear to extend up to the modern surface and affect delta

morphology. Figure 1.4 shows fault planes mapped from the Breton Sound seismic data projected onto a satellite photo of the modern surface. As demonstrated by Gagliano (2003) and George (2008), several of these faults correspond to abrupt shifts from wetlands to fully submerged areas on the delta surface. In addition, the area of the survey with the highest density of growth faults corresponds to the last major bend of the Mississippi River (bottom right of Figure 1.4) before reaching its Bird's Foot Delta.

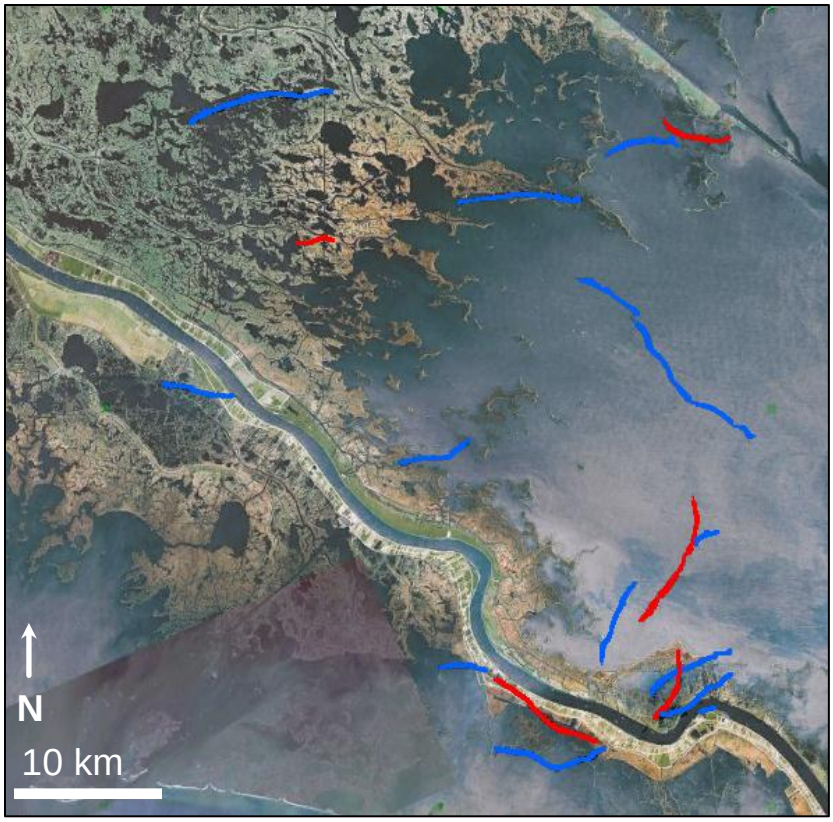

Figure 1.4: Projections of fault planes overlain on a satellite photo; blue indicates a basinward fault dip and red indicates a landward dip.

The high concentration of mappable channels and growth faults within the seismic survey make it well suited for examining fluvial systems as well as the relationship between faults and paleo-rivers. In addition, the range of fluvial styles allows for the effect of faults on both small channels and larger fluvial elements to be examined.

Chapter 2: Data and Methodology

A thorough attempt at understanding stratigraphy in subsurface data requires the integration and synthesis of a wide array of information obtained from seismic amplitude data and associated attribute and inverted volumes (with both map and cross sectional views), well log data, and biostratigraphic data. This section details the approaches used towards the goal of understanding the external geometry and lithology of late Miocene to Pliocene Mississippi River Delta fluvial systems and their interactions with growth faults.

2.1 Seismic data

The 1375 km^2 3D seismic volume, consisting of merged surveys from Breton Sound's Grand Lake, Black Bay, and Quarantine Bay, was shot in 1998 and 1999 and was provided by WesternGeco® for research use. Due to the variety of survey environments (from wetlands to shallow marine), a mix of energy sources were used during survey acquisition including airgun, pentolite, and dynoseis. Seismic processing was completed by Westerngeco® in 2006. Figure 2.1 shows checkshot results and survey acquisition and processing parameters. All seismic analysis for this project was based off of post-stack data. In the ~ 500 m to 2000 m interval of interest, frequency rollover is at around 40 Hz (Fig. 2.2) and P-wave velocities range from 1900 m/s to 2700 m/s which leads to a best case vertical resolution of about 12 to 16 meters. The seismic volume has a sampling rate of 4 ms.

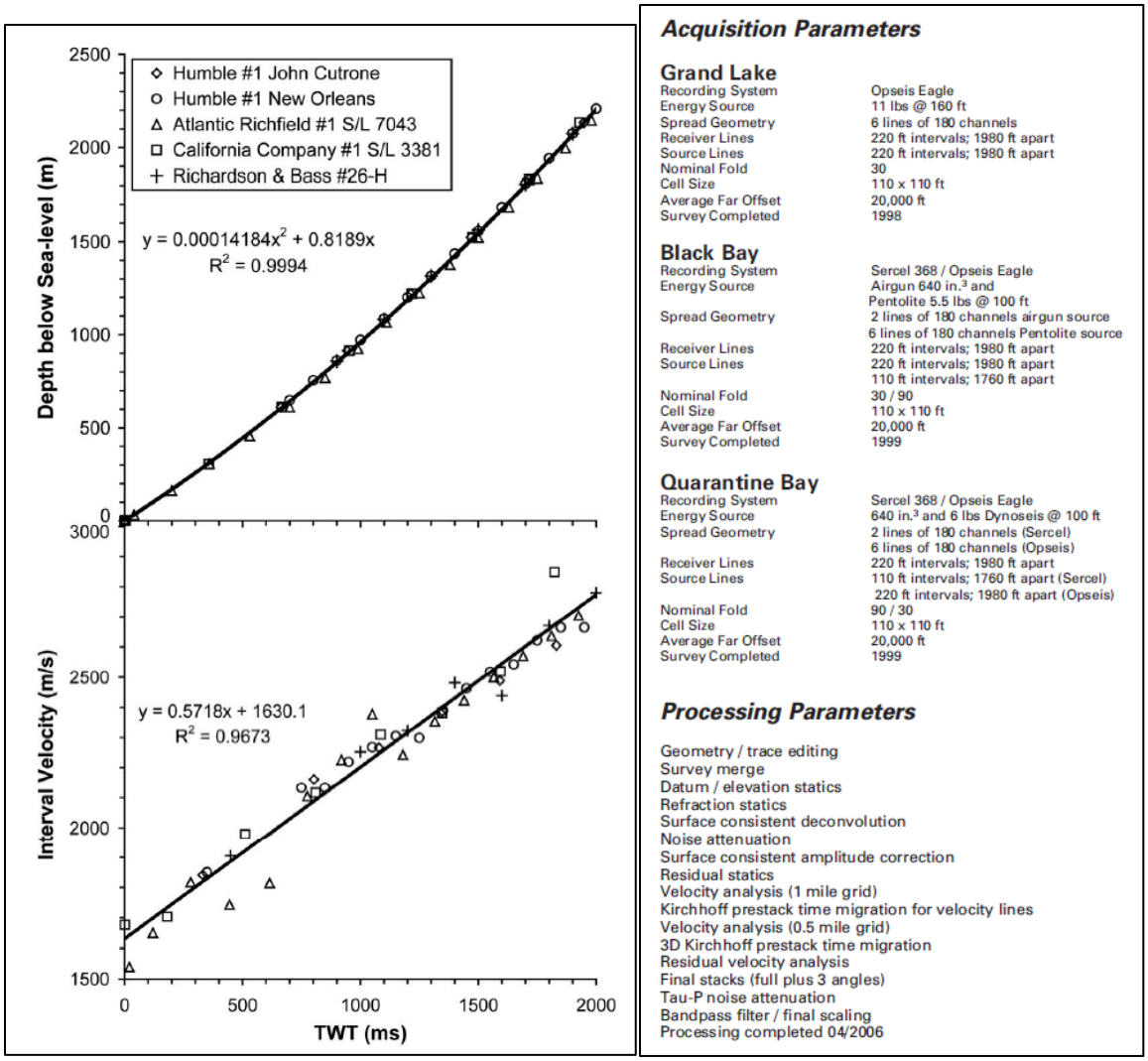

Figure 2.1: The relationships between two-way travel time (TWT) and interval velocity and TWT and depth below the present-day surface derived from 5 checkshot wells in the study area (George, 2008). Seismic acquisition and processing parameters are also shown here.

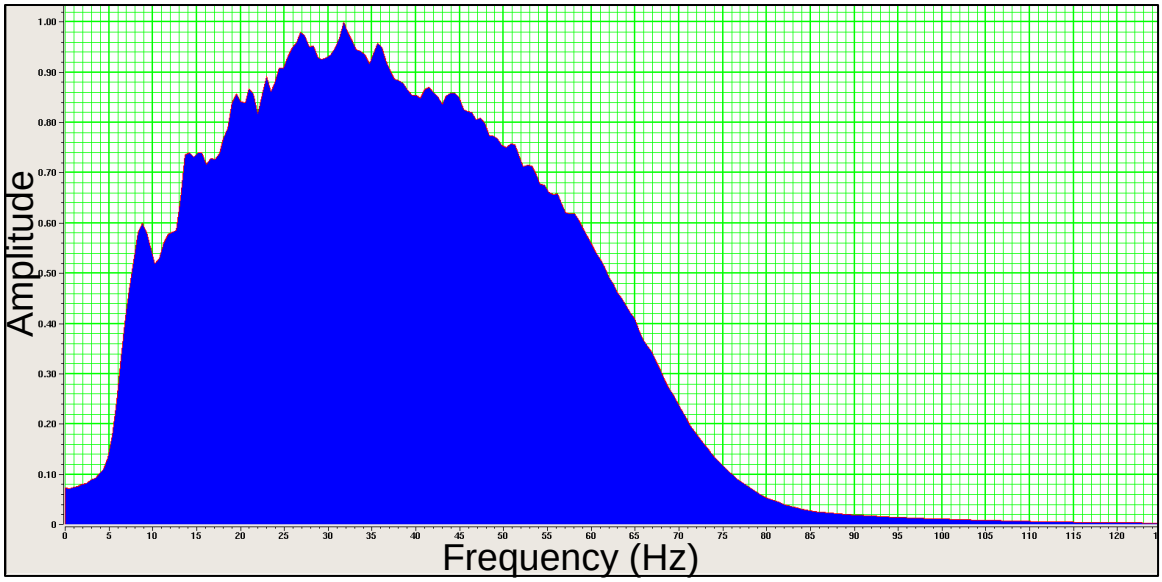

Figure 2.2: Amplitude spectrum for the seismic volume from approximately 500 m to 2000 m below the present-day surface.

The original seismic amplitude volume was provided as 0° phase data. Under this configuration, isolated sandy channel fill in the seismic volume is usually defined at the base by a positive reflection and at the top by a negative reflection (Fig. 2.3, upper). To aid in interpretation, the seismic volume was rotated a positive 90 degrees from its original 0° phase position. With this 90 degree phase orientation, an isolated sandy channel fill in this dataset usually appears as a single positive reflection (Fig. 2.3, lower), simplifying the identification of channels and mapping of their geometries (Zeng and Hentz, 2004).

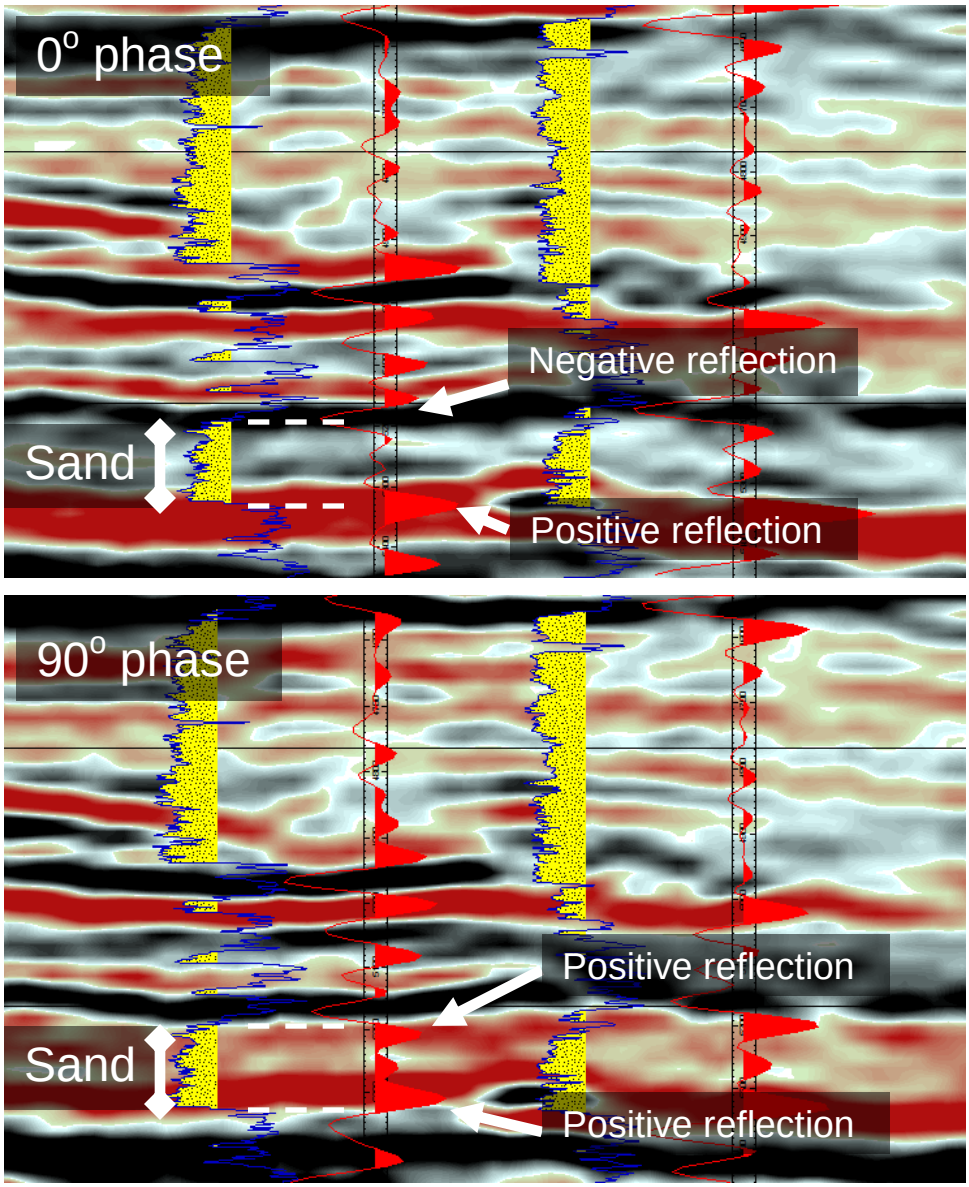

Figure 2.3: 0° and 90° phase seismic data with synthetic seismograms and gamma ray logs shown. The seismic section is the same in both images. The upper image is 0° phase seismic and synthetic; the lower image is 90° phase seismic and synthetic. Sand units in the upper image are defined by a negative reflection at the top of sand and a positive reflection at the base of sand. Sand units in the lower image are defined by positive reflections at both the top and the base of sand.

2.2 Software and workstations

Processing and interpretation of seismic and well log data was completed using an array of software and workstations. Digitization of well log data and limited seismic processing and interpretation were done using Seismic Micro-Technology (SMT) Kingdom Suite™ software on a Dell™ Optiplex 960 workstation with Windows 7® Professional 32 bit. Within the SMT® Kingdom Suite™ software, I relied on their 3dPAK, VuPAK, SynPAK, and TracePAK tools which provide an integrated environment for geological and geophysical interpretation. The majority of seismic processing and interpretation used Halliburton GeoProbe™ Volume Interpretation Software on a Dell Precision T7400 Workstation with RedHat™ Enterprise Linux 64 bit. Well log processing and all inversion implementations were completed on the same Linux workstation using CGG Veritas Hampson-Russel™ inversion software.

2.3 Well log data

No well log data was available from WesternGeco®; instead, log data was obtained from the Louisiana Department of Natural Resources via their Sonris.org GIS interface. The workflow for importing a log in LAS format consisted of: a) finding the serial number of a well located within the survey by using the Sonris GIS application which allowed for sorting by map view location, b) searching the Sonris database to see if the .TIFF files for that well contain any target curves (P-wave velocity, gamma ray, density, porosity, and resistivity) within the interval of interest, and c) using KingdomSuite™ software to digitize that curve and export it into LAS format (few of the wells were deviated, making the transfer to seismic relatively simple) and Hampson-Russel™ Strata software to tune the fit between the well log and seismic data. Unfortunately, even though logs are available for hundreds of wells within the survey, velocity and density data are remarkably rare (especially within the relatively shallow late Miocene to Pliocene zone) and there is no way to specifically sort the available logs by curve type, making acquisition of velocity and density data very difficult. As inversion is a project objective and typically requires velocity and density data, these two curves can be estimated by deriving them from other curves with greater availability. Nearly all the available logs contain resistivity curves. These resistivity curves can be related to Vp using the Faust transform (Equation 1), which is an empirical relation linking velocity to depth and the formation factor (the ratio of formation

resistivity to the resistivity of water). The physical basis for this relationship is probably the dependence of both terms on total porosity (Hacikoylu et al., 2006). The Faust transform is as follows:

$$Vp = 2.2888(ZF)^{1/6},\ F = RF/RW \qquad (1)$$

where Vp is P-wave velocity (in km/s), Z is depth (in meters), F is the formation factor, RF is resistivity of the formation, and RW is the resistivity of water. As this is an empirical relationship most applicable for the data from which it was derived, using this transform to create velocity logs as an input to inversion is not ideal; however, given the near complete lack of measured velocity data in this area and the widespread availability of resistivity logs, its use seems a necessary approach. Additionally, density curves are as rare as velocity curves, so in order to obtain some constraint on density the Gardner relation (Equation 2) is applied to the velocity curves which were derived from the resistivity curves. The Gardner relation is as follows:

$$p = 0.23Vp^{0.25} \qquad (2)$$

where p is density. Fortunately, seven porosity curves consisting of a mix of density-porosity and neutron-porosity were available so no transforms were necessary for porosity analysis.

After digitizing log curves, getting a moderate to high quality tie between the seismic and the well data is one of the most crucial aspects of integrating well logs into the study. Figure 2.4a shows a synthetic (blue) next to a real trace (red) with a relatively good tie between the two. The process for getting a tie like this is as follows. First, checkshot data is used to place the log data into roughly the correct time-depth range. Next, a statistical wavelet is extracted from traces around the wellbore. At this point, Strata software will suggest a bulk time shift (Fig. 2.4b) to minimize the miss-tie between the synthetic trace (calculated with velocity and density logs derived from the Faust transform and Gardner's relation). After this bulk time shift, events on the synthetic trace can be correlated with events on the real trace and a time-drift curve is applied to the time-depth curve (Fig. 2.4c) in order to improve the match of the picked events.

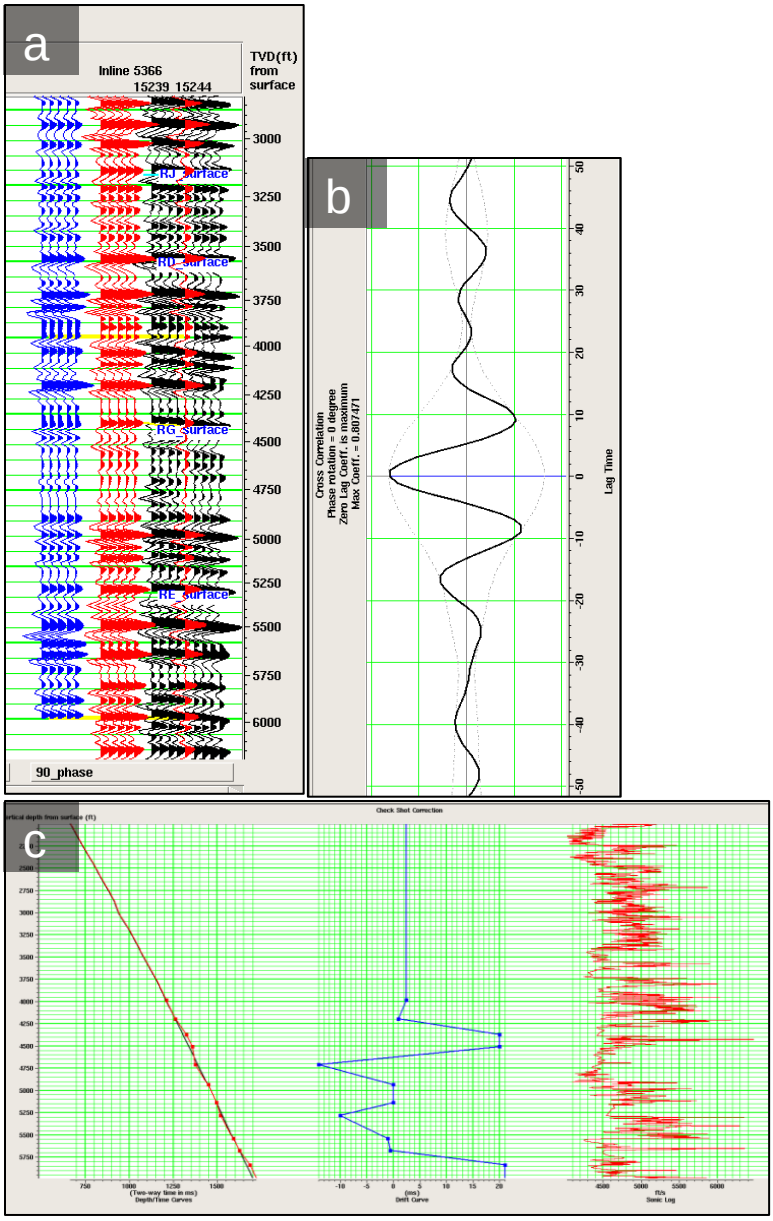

Figure 2.4 a) Synthetic (blue) trace against the real trace (red) showing good agreement between the two (correlation coefficient of 0.758). Each trace is shown repeated 5 times as a visual aid. The neighboring traces are shown in black on the rightmost set of traces.
b) Correlation coefficient on the horizontal axis against bulk shift (lag time) on the vertical axis.
c) Drift curve (blue) applied to the time-depth curve (leftmost red) to generate the best fit between the synthetic and real traces.

This process is then repeated for every well in the dataset. Once all the wells are tied as well as possible, a single wavelet for all the wells is extracted from the well log data (Fig. 2.5).

Though a wavelet extracted from well data may be more accurate than a wavelet extracted from seismic data, extraction is performed after tying wells to seismic using statistical wavelets because it is very sensitive to the match between the well and seismic data (Strata Software Documentation, 1999). Time-depth curves are then adjusted (by matching events on the synthetic and the seismic traces again) in order to refine the tie using this single wavelet. At this point, wells that still have low correlation coefficients (with 0.5 or below as the cutoff) between synthetic and real traces are dropped from the study. Figure 2.6 shows the correlation coefficients for wells used, with 15 falling between 0.5 and 0.9.

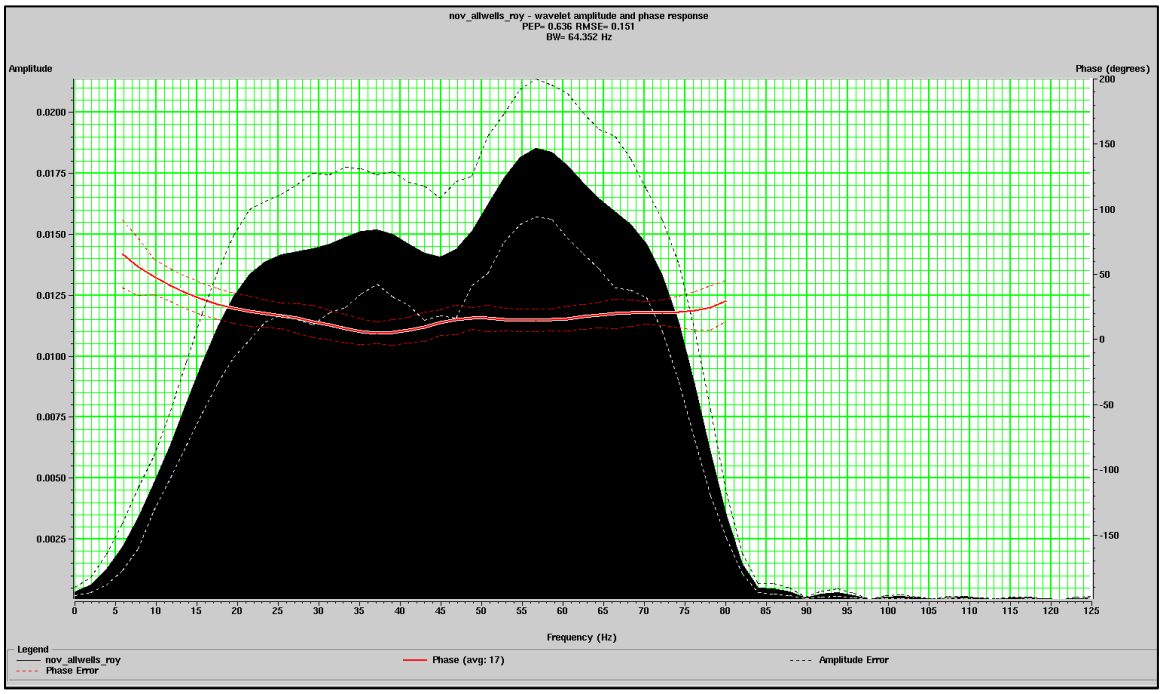

Figure 2.5: The wavelet derived using all wells (frequency on horizontal axis against amplitude on the vertical axis).

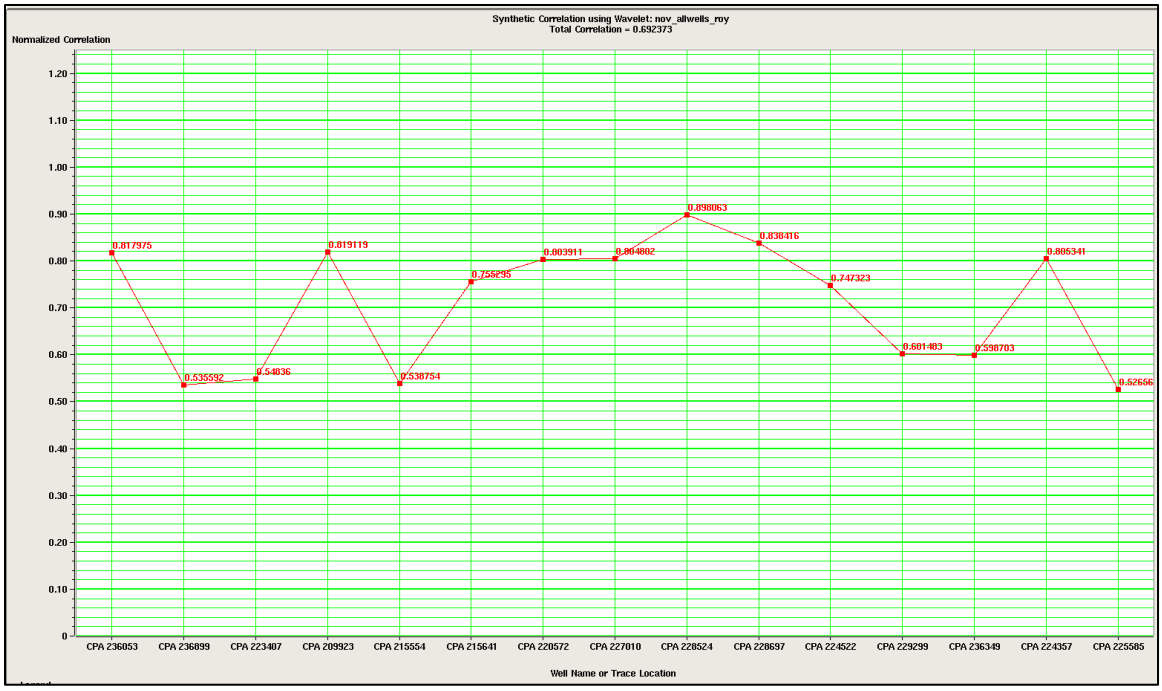

Figure 2.6: Correlation coefficients for synthetic and real seismic traces at all well locations. Values for the correlation coefficient range between 0.5 and 0.9.

2.4 Horizons and surfaces

Due to the large surface area covered by the seismic volume and the high lateral continuity of channelized features (with some channels running for over 20 km), the data set is well suited for a map view based approach to imaging channels and valleys. The simplest method for doing this is to move up and down the volume using a “probe” with a surface at a constant time. However, this method is problematic because the stratigraphy varies with time (due to a regional basinward dip as well as localized movement along faults) so a simple “time slice” will cut across stratigraphy and become younger moving basinward. To avoid this complication, a surface based approach can be used to create either horizon slices or stratigraphic slices. Horizon slices are ideal for mapping channels but reflect stratigraphy less accurately than do stratigraphic slices away from the surface used for flattening. Stratigraphic slices do not allow for channel mapping directly onto the slice but are useful for calculating surface based attributes.

To create horizon slices, a dense grid of lines is picked on a reflection that is persistent across the entire amplitude volume. This horizon is then filled in using GeoProbe's ™ ezTracker feature and the object that results is termed a surface. This surface is then used to flatten a portion of the original seismic volume or an attribute calculated from that volume. Here, a time shift is applied to every point of the surface so that the resulting surface is flat. This same time shift is then applied to the seismic volume over a specified time interval above and below the surface which results in a flattened volume that, near the surface used for flattening, does not cut across stratigraphy. However, because the amount of subsidence changes with time, map-view slices distant in time from the surface used for flattening reflect stratigraphy less accurately than do slices taken near the surface used for flattening. To alleviate this problem, seven different surfaces (each separated by a few hundred milliseconds) were mapped and flattened volumes created based on each of these surfaces.

Figure 2.7 shows the benefits of a surface based approach to imaging fluvial stratigraphy. The horizon slice images a nearly 20 km north-south trending channel on the western side of the survey. The time slice images the same channel for only its north most ~ 5 km and cuts through unrelated stratigraphy south of this.

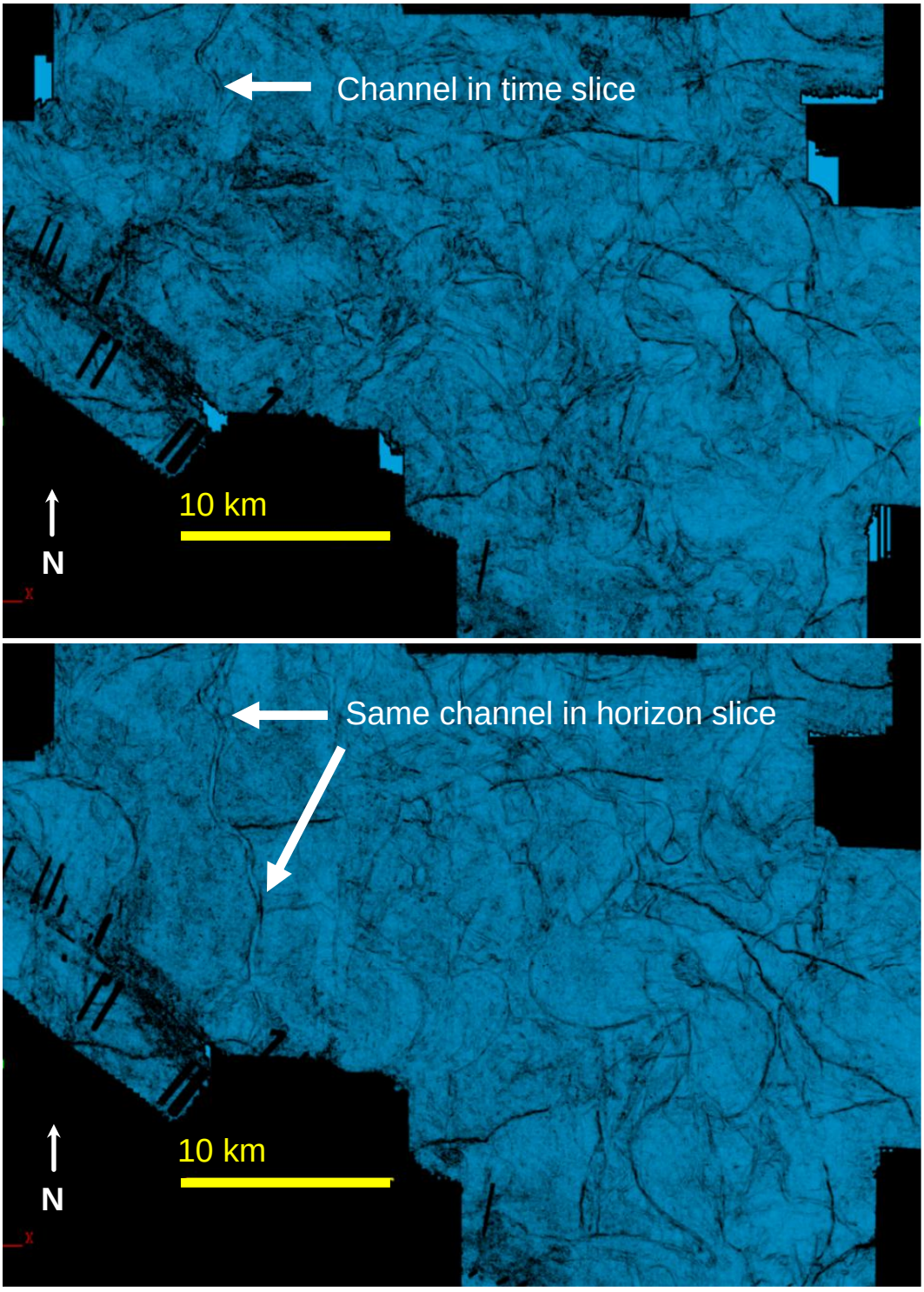

Figure 2.7: A time slice (upper image) and a horizon slice (lower image) of similarity attribute. Notice that the channel appears truncated on the time slice but can clearly be seen extending across the entire survey area on the horizon slice.

To create a stratigraphic or stratal slice, a specified number of proportionally spaced slices are calculated between two mapped surfaces. This method improves upon the accuracy of horizon slices by taking the stratigraphic profile of both the upper and the lower surface into account which limits the potential for errors due to cutting across unrelated stratigraphy (Zeng, 2010). The number of surfaces created between each pair of surfaces was chosen to roughly match the 4 ms sampling rate of the seismic data. In total, 227 stratigraphic slices were created that fall between the 7 mapped surfaces.

For average time, depth, or age calculations for a specific surface, an estimate of the average time (two-way travel time) of each surface is required. This was obtained by exporting each surface in .xyz format and finding the average of the time values (followed by depth conversion). To avoid complications from the complexly faulted southeastern area of the survey where little fluvial stratigraphy is imaged, the measurements were limited to the ~ 75% of the survey north of this area (where the y coordinate is > 300,000 survey feet), resulting in averages from nearly 925,000 separate point measurements for each surface.

2.5 Seismic attributes

Seismic attributes can be used to improve visualization of channelized features as well as to gain a heuristic understanding of lithology and variations in lithology. While several dozen attributes are easily available to the interpreter, a few stand out in their ability to clearly define channels and valleys. For this dataset, the similarity attribute and the sweetness attribute were most successful in defining channelized features and so were used extensively for mapping. Spectral decomposition was also used to provide information about the frequency dependence of depositional elements.

Similarity is an edge detection attribute defined as the distance in hyperspace between the vectors of two trace segments normalized by the sum of the lengths of the vectors. Similarity is similar to the commonly used coherence; however, similarity has the advantage of taking the amplitude difference between the two trace segments into consideration (Tingdahl and Rooij, 2005). In general, channel and valley edges as well as faults are imaged as low similarity areas, while un-channelized interfluve and un-faulted sections are imaged as high similarity areas. With GeoProbe's™ "Combo Mambo" feature, the similarity volume can be co-

rendered with the amplitude volume. As shown in Figure 2.8, the similarity attribute appears as surface shading on the amplitude volume which allows for direct integration of edge detection information with amplitude data.

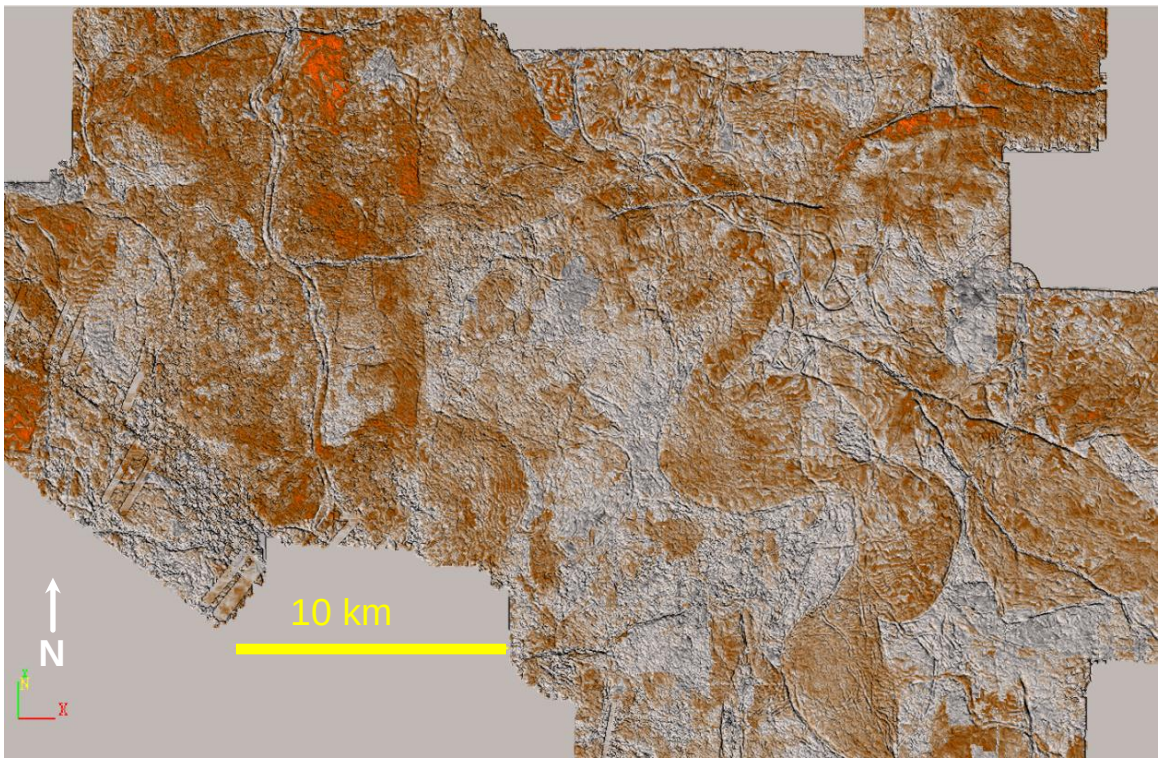

Figure 2.8: Co-rendering of amplitude (hotter colors indicate high positive amplitude) and similarity volumes on a horizon slice. View is from directly overhead.

Sweetness is defined as reflection strength divided by the square root of frequency. The basic idea of this attribute is that sandstones near tuning thickness will tend to have high reflection strength and low frequency resulting in a high sweetness value, while thinly bedded mudstones will have a low sweetness value (Hart, 2008). Unfortunately, since many factors besides lithology (e.g., fluid content or pore pressure) can influence the reflection strength and frequency, its usefulness as a lithology indicator is limited. However, because fluvial fill tends to have a different sweetness value than the surrounding sediments, the attribute can be useful in imaging channelized features as demonstrated in Figure 2.9.

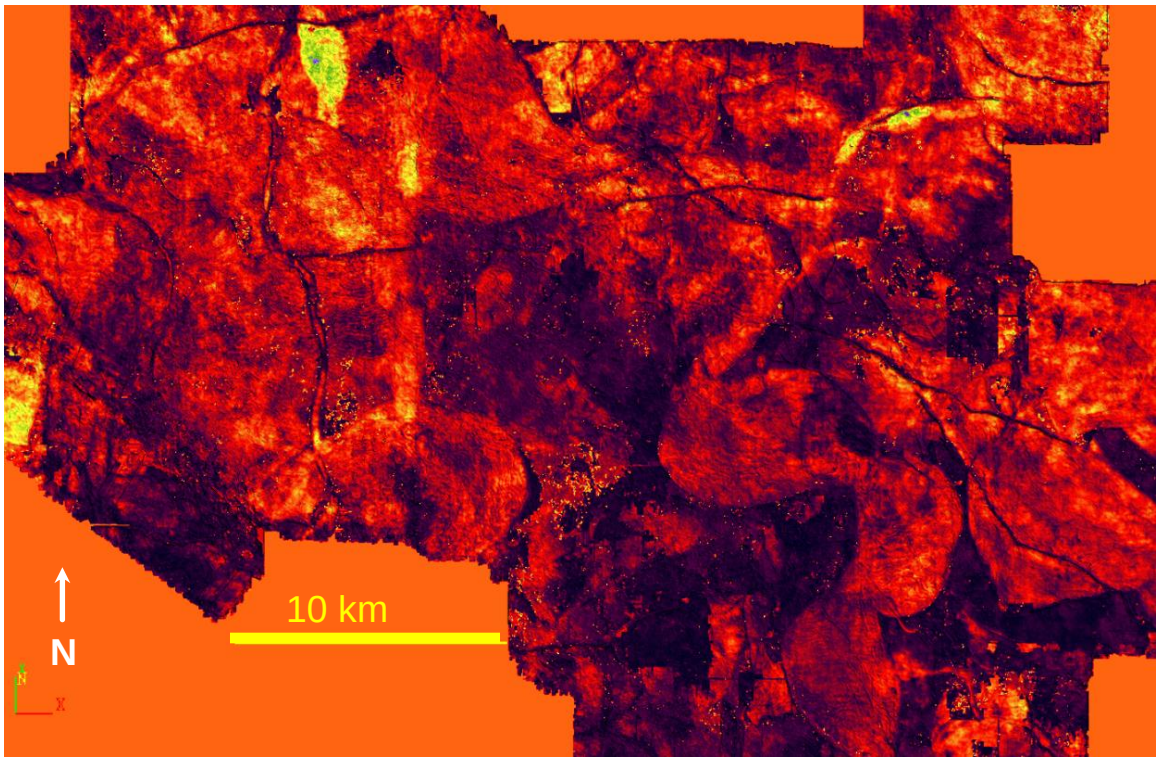

Figure 2.9: Sweetness attribute (hotter colors indicate higher sweetness). View is from directly overhead.

Figure 2.10 shows the spectral decomposition technique applied to a small vertical interval centered on a surface. Spectral decomposition is a frequency based seismic interpretation method where the amplitude or phase spectra for specific frequencies are calculated, isolated, and viewed (Partyka, 1999). An advantage of this technique over traditional attributes (e.g., edge detection attributes like coherence or similarity) for imaging channelized features is that spectral decomposition is sensitive to variations in bed thickness. Spectral decomposition is accomplished by applying a Fourier transform to a time window around a surface to convert that window from the time domain to the frequency domain.

Spectral decomposition results in a "tuning cube" where the vertical axis is frequency. This frequency cube can be sliced horizontally or vertically to examine the frequency response of depositional elements. In general, at low frequencies, thick beds have a stronger amplitude response than thin beds; at high frequencies, thin beds have a stronger amplitude response than thick beds. Key to the effective imaging of depositional elements with spectral decomposition is selection of an appropriate surface and time window. The surface should

contain, as identified using other attributes, the channelized features for which more detail is desired. The time window will then follow the same topography as the surface for a specified time above and below the surface. If the time window is set too large, the geology contained within can be considered mathematically random and the spectra will approximate the seismic wavelet and not the geology (Partyka et al., 1999). With a narrower time window, the geology becomes less random and acts to increase resolving power by attenuating the spectra of the source wavelet. To avoid edge affects, a taper must be applied to the time window. I used a Gaussian taper in this project in order to focus spectral decomposition on the surface being used.

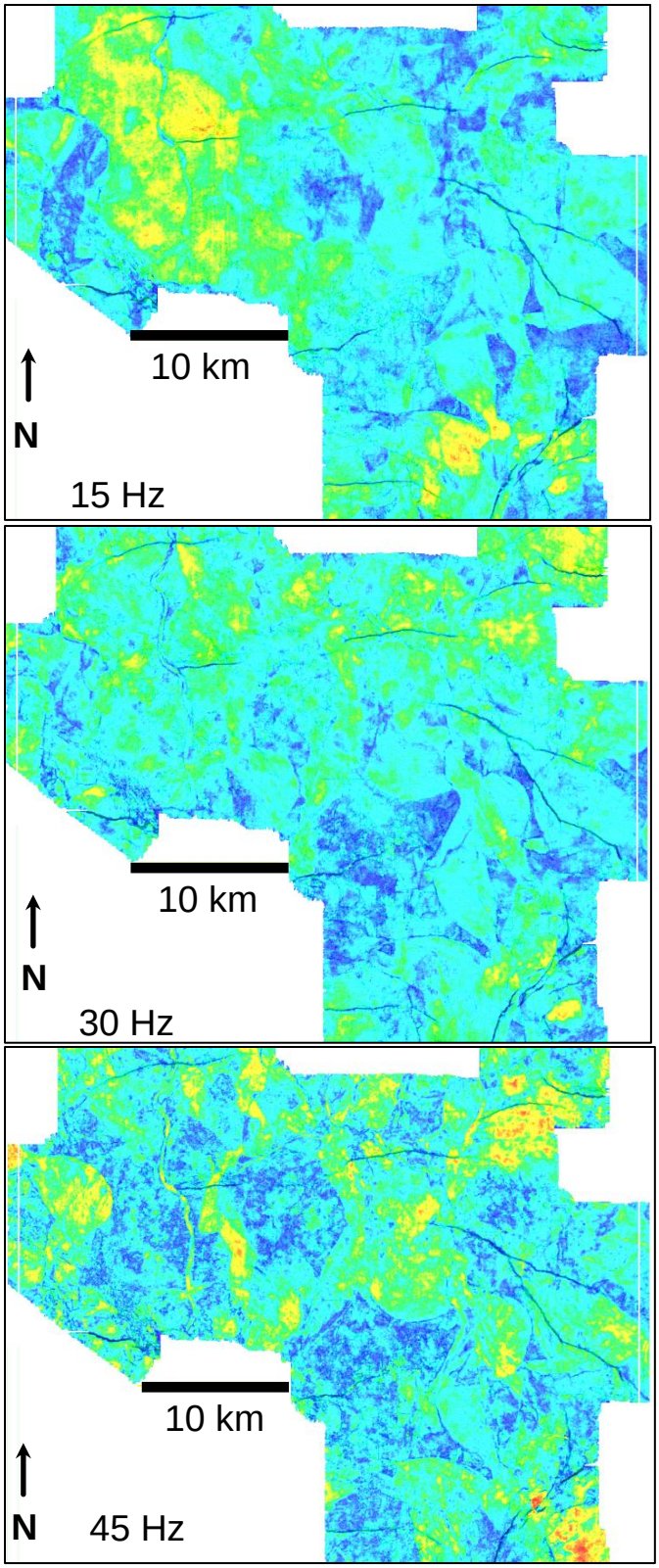

Figure 2.10: Spectral decomposition applied to a 120 millisecond sampling window around a surface at 15 Hz, 30 Hz, and 45 Hz. Thinner channelized features resonate as frequency increases. Hotter colors indicate higher amplitude.

2.6 Inversions for impedance and porosity

In addition to standard attributes, inverted volumes can be useful in understanding lithology and variations in lithology within channel and valley fill. These inversions can provide a valuable link between high resolution, laterally limited well log data and low resolution, laterally extensive seismic data. The process for creating impedance and porosity inversions is detailed here.

The seismic trace can be represented as the convolution of the reflection coefficient series with the wavelet plus noise (Equation 3).

$$S = W*R + noise \qquad (3)$$

where S is the seismic trace, W is the wavelet, and R is the reflection coefficient series.

Inversion can be thought of as applying the inverse of the wavelet to the seismic trace. This leads back to the reflectivity which can then be related to the rock properties of density and velocity (Strata Software Documentation, 1999).

A number of different inversion methods are available in Strata inversion software. For this project, I chose to use both bandlimited and model based inversions. Bandlimited (recursive) inversion takes an impedance log, filters it to obtain the low frequency background trend not available from seismic data, and adds it to a seismic trace on which the recursive equation (Equation 4) has been applied. Application of this equation assumes that the input data is 0° phase. The recursive equation is as follows:

$$Z_i + 1 = Z_i * \frac{1+r_i}{1-r_i} \qquad (4)$$

where Z_i is the impedance of the ith layer and r_i is the reflection coefficient for that layer. Interpolation between impedance curves is guided by picked surfaces. As this inversion method does not require knowledge of the wavelet, it may be an effective choice where ties between well and seismic data are uncertain (Strata Software Documentation, 1999).

The second inversion method used was model based inversion. Here, an impedance log is blocked (averaged) over some layer size and a synthetic trace is created using a derived

wavelet. Through a number of iterations, the wavelet and layer size are adjusted in order to minimize the error between the synthetic trace and the measured trace (Strata Software Documentation, 1999). Interpolation between well control points is also guided using picked surfaces.

The workflow for performing either type of inversion involves first tying seismic and well data, importing horizons (picked in Geoprobe^{TM}) to guide the inversion, selecting parameters for inversion, calculating the inversion, and performing error analysis on the inversion result and possibly refining parameters or removing obviously bad wells and repeating the inversion.

For bandlimited inversion, the only inversion parameter modifiable is the hi-cut frequency which I kept at the default frequency of 10 Hz. For model based inversion, there are several important parameters that may be adjusted including block size, number of iterations, and the global or local scaler. The block size was chosen to match the sampling rate of the seismic data (4 ms). The number of iterations (for the inverted synthetic and real traces to match) used was 12. A single global wavelet scaler was used which matches the amplitudes of the synthetic to that of the real trace. An optional configuration is to use a local scaler calculated for each trace. This local scaler may be more accurate than the global scaler; however, it is computationally expensive so for this project I chose to use a global scaler.

Once the inversion is applied to the entire volume, error analysis can be performed in various ways. One quality check, as shown in Figure 2.11, is to look at the residual traces when synthetic traces (derived from the inversion) are subtracted from the real traces. Ideally there should be low energy with no localized events (Strata Software Documentation, 1999). In the results for the model based inversion there is generally low energy with some localized events (mostly occurring below the lowest horizon used to guide the inversion). Another quality check is to look at the root mean square error between the original log and the inverted result (Fig. 2.12). The RMS errors in P-impedance were all below 1000 at the well locations (in line with examples shown in the user manual for Strata).

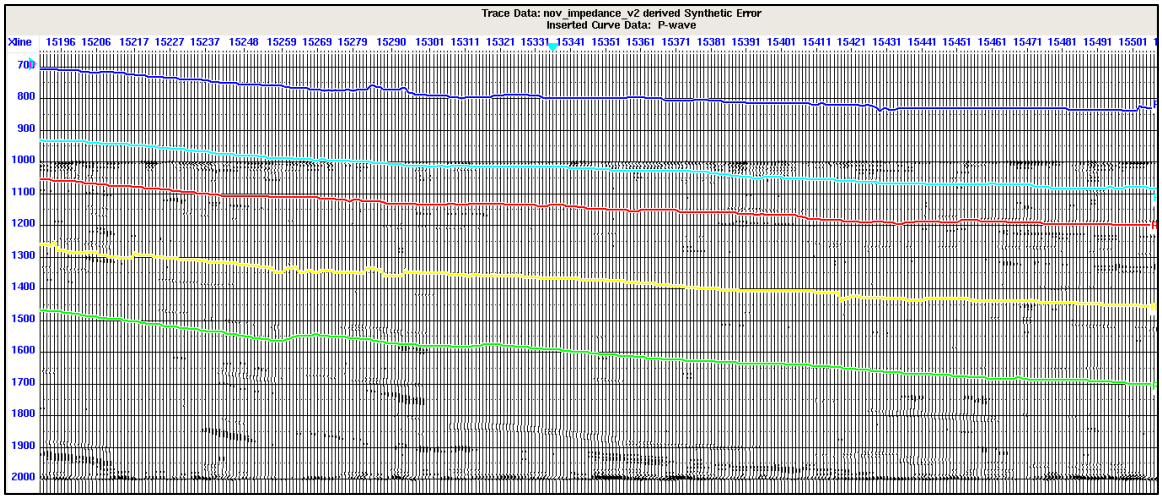

Figure 2.11: A cross section of the residual between real and synthetic traces derived from inversion. Notice that the residuals are small and largely unsystematic.

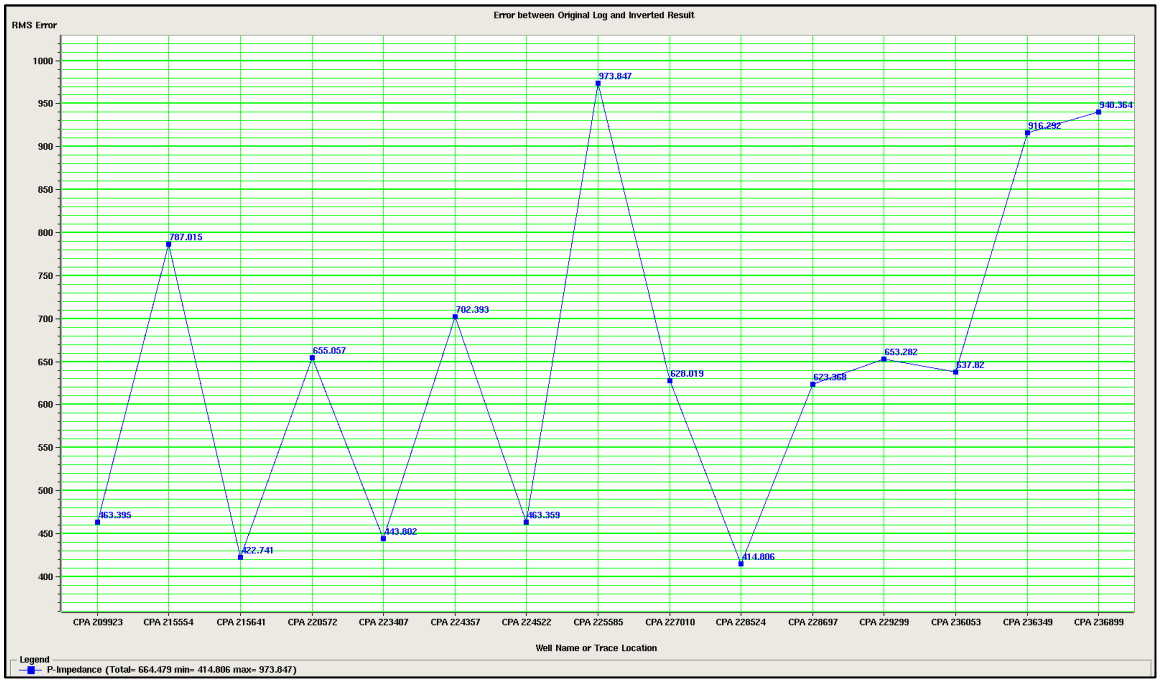

Figure 2.12: RMS errors in P-impedance between the original logs and the inverted results.

Figure 2.13 shows a comparison of bandlimited inversion and model based inversion. In the examples below notice the concave up channel like feature just below 1400 ms on the left-hand side of the cross sections. This imaged feature is defined as a low impedance zone within a higher impedance field using both inversion methods. Many small, localized events are present in both inversions. However, the model based inversion shows slightly more detail than the bandlimited inversion and also shows more variability in impedance.

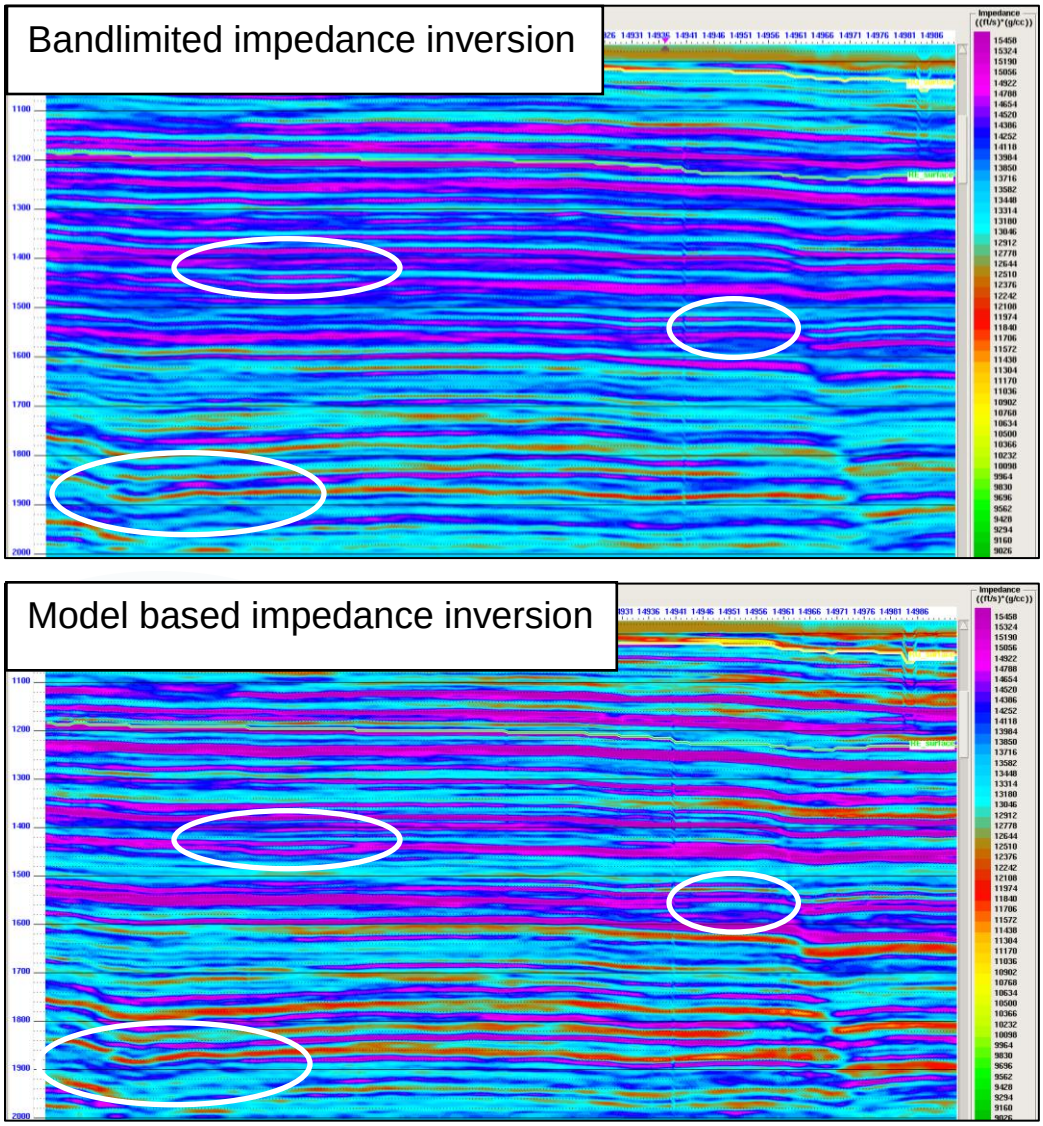

Figure 2.13: (Top) Result of a bandlimited inversion. (Bottom) Result of a model based inversion. Similar events are circled in each cross section.

As demonstrated in the crossplot shown in Figure 2.14, there is a physical connection between impedance and porosity where higher porosities correlate with lower impedances (lower velocities are due to decreased stiffness, reducing the elastic moduli). Porosities in this dataset generally range from 20% to 40%. The highest porosities are associated with the lowest gamma ray measurements. The impedance inversion result makes for an ideal input for porosity inversion because of the clear physical relationship between porosity and impedance.

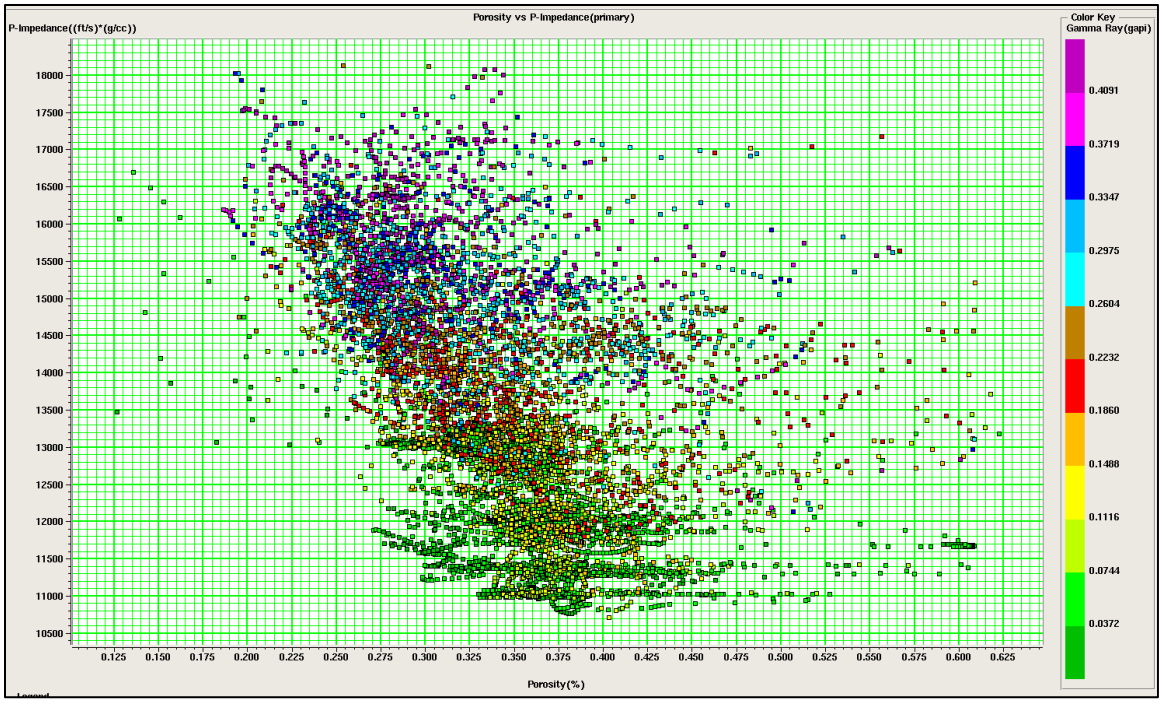

Figure 2.14: Porosity (horizontal axis) against P-impedance (vertical axis) color coded by gamma ray value. The data define occurrence of lower impedance sands and higher impedance muds.

Inversion for porosity using Hampson-Russel^{TM} Emerge software attempts to directly predict porosity from seismic data. This is accomplished by finding a statistical relationship between attributes and target porosity logs and extrapolating this relationship to the rest of the volume (Emerge Software Documentation, 2006). An important point is that there may be no clear physical relationship between attributes used and porosity. Use of any individual attribute depends on its success in decreasing the training error and increasing predictive power.

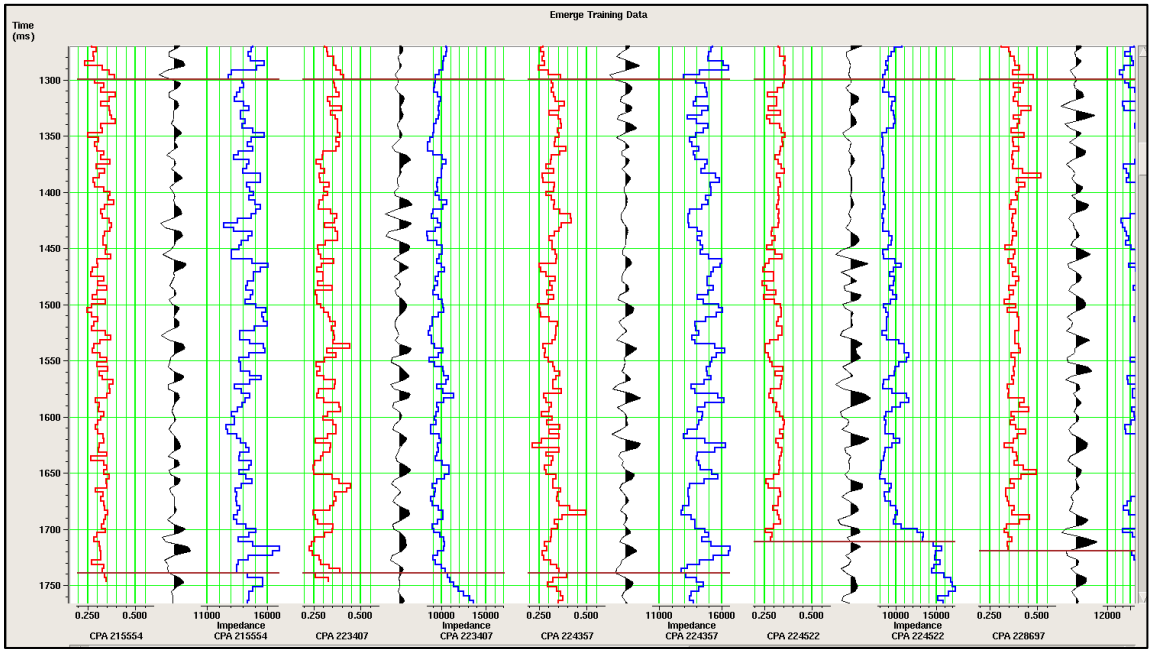

Figure 2.15: Input data for the Emerge software: porosity (red), seismic trace (black), and impedance log (blue).

Figure 2.15 shows the input data necessary to run the Emerge software. These data consist of a target porosity log, a trace at the well location, and the impedance inversion result. Emerge takes a trace at the well location (using wells that were already tied in Strata for the impedance inversion) and calculates several dozen attributes using that trace. It then performs a multivariable regression on the attributes and the inversion result to see which combination of attributes is best able to predict the porosity log. Specifically, the program, by minimizing the mean-squared prediction error, returns the best single attribute for predicting the target log, the best pair of attributes, the best triplet of attributes, and so on until the maximum number of specified attributes is reached (Hampson et al., 2001). The transforms between porosity and attributes may be linear or nonlinear in form. Because the seismic data is lower resolution (lower frequency) than the well log data, a sample on the well log may be related to multiple neighboring samples on the seismic data. To help alleviate this difference in vertical resolution, a convolutional operator is used to relate multiple attribute samples to the single target log sample (Hampson et al., 2001). A range of convolutional operator lengths can be tested and a specific length (and number of attributes) chosen such that validation errors are minimized (Fig.

2.16). Using too many attributes or too long of an operator length will result in a better fit to the training data but a decrease in predictive power. This “overtraining” can be avoided by minimizing the validation error using cross validation. To do this, a single well is dropped out of the training set and the remaining wells are used to predict the porosity log for the hidden well (Hampson et al., 2001). Once an ideal operator length and number of attributes is determined an inversion may be performed using these settings.

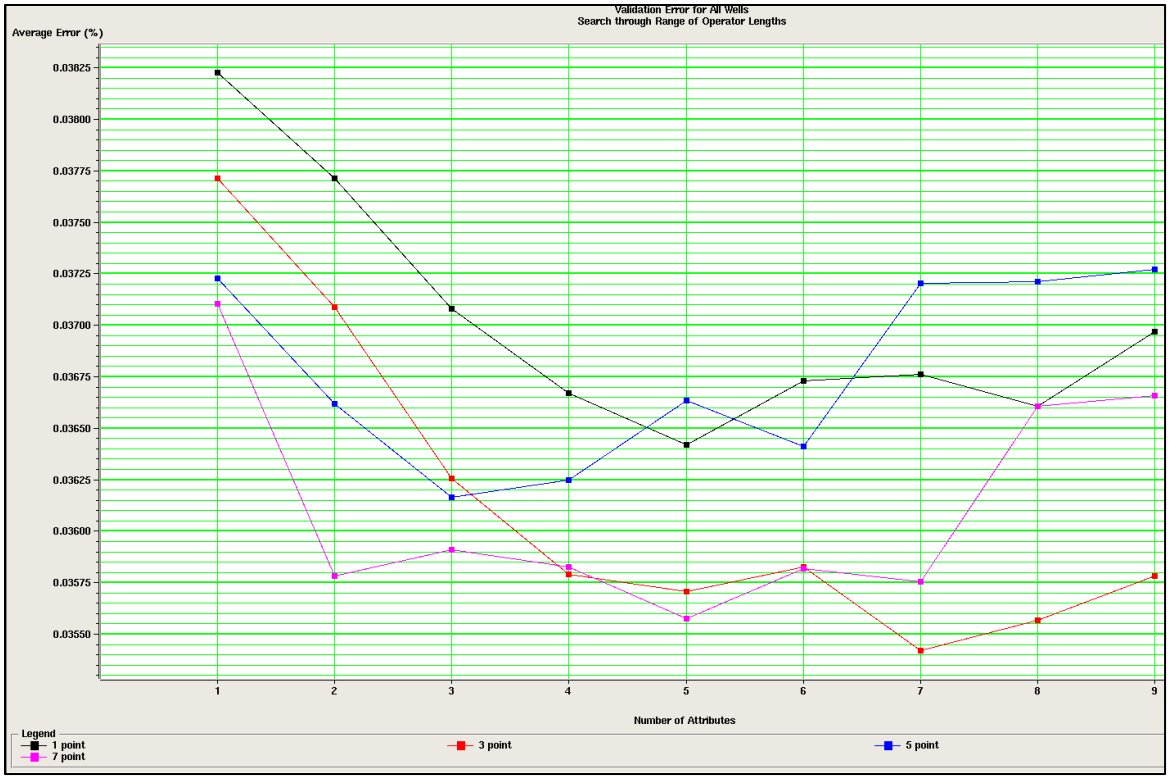

Figure 2.16: Number of attributes (horizontal axis) against validation error (vertical axis) for convolutional operator lengths of 1, 3, 5, and 7. The minimum in validation error is reached at 7 attributes and an operator length of 3.

The multi-attribute regression for this dataset had the lowest validation error at 7 attributes and an operator length of 3. However, the 7 attributes in this configuration did not include the inversion result. As there is a clear physical relationship between porosity and impedance, I chose to use the next lowest validation error for the porosity inversion parameters. This was found at 5 attributes and an operator length of 7. The final attributes that always led to a decrease in validation error were (beginning with the most predictive attribute):

integrate, integrated absolute amplitude, the expected 1 / impedance result, instantaneous frequency, and a lowpass filter (Table 2.1).

	Target	Final Attribute	Training Error	Validation Error
1	Porosity	Integrate	0.035930	0.037102
2	Porosity	Integrated Absolute Amplitude	0.034585	0.035783
3	Porosity	1 / (Impedance)	0.033900	0.035909
4	Porosity	Instantaneous Frequency	0.033196	0.035827
5	Porosity	Filter 5/10-15/20	0.032674	0.035577
6	Porosity	Instantaneous Phase	0.032222	0.035818
7	Porosity	Filter 25/30-35/40	0.031793	0.035757
8	Porosity	Amplitude Weighted Frequency	0.031363	0.036608
9	Porosity	Amplitude Weighted Phase	0.030960	0.036659

Table 2.1: The set of attributes yielding the best prediction for porosity using an operator length of 7. The attributes are ranked from most to least predictive.

This specific combination of attributes and operator length led to an application correlation coefficient of 0.586 using all of the wells and a validation correlation coefficient of 0.485 between the training set and hidden wells. Figure 2.18 shows the application result and the training result corresponding to these correlation coefficients.

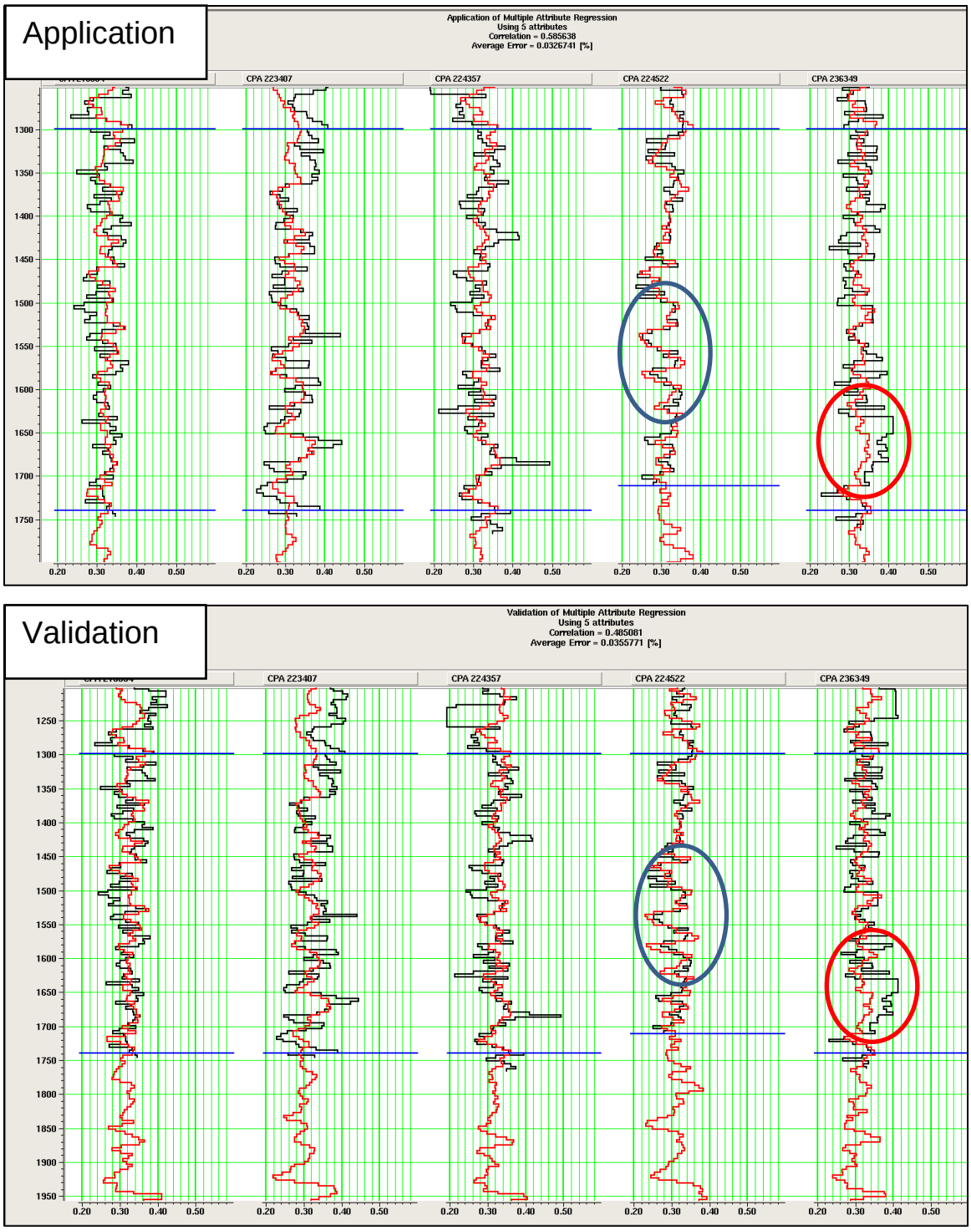

Figure 2.18: The application result (top) and the validation result (below). The original log is shown in black and modeled log in red. Matches are strong in some areas (blue circles) and poor in others (red circles).

The multi-attribute regression porosity inversion (Fig. 2.19) images channels as distinct units with overall higher porosity than neighboring un-channelized areas. Variability within channels is correlated with changes in gamma ray (high gamma ray indicating higher clay content and lower porosity than clean sand).

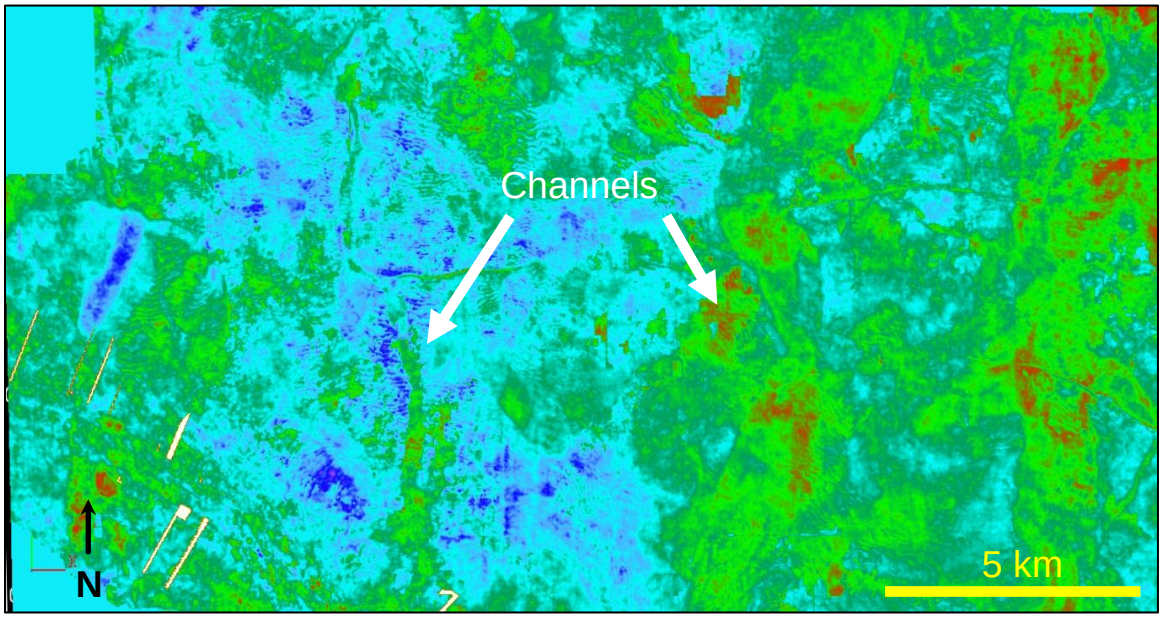

Figure 2.19: Horizon slice through the multi-attribute regression porosity inversion. View is from directly overhead. Hotter colors indicate higher porosities.

2.7 Biostratigraphy

Biostratigraphy reports were provided by Paleo-Data Inc. and come from four wells located within the survey. These reports use last occurrences of benthic foraminifera recorded from well cuttings to provide age control. The four wells show a long term sedimentation rate that varies by location and ranges from 0.19 m/kyr to 0.26 m/kyr over a roughly 10 million year interval. A rate of 0.23 m/kyr was used for all age calculations. This is likely the most robust rate as it comes from the well (Fig. 2.20) with the most data points (12) and falls near the middle of the range of rates.

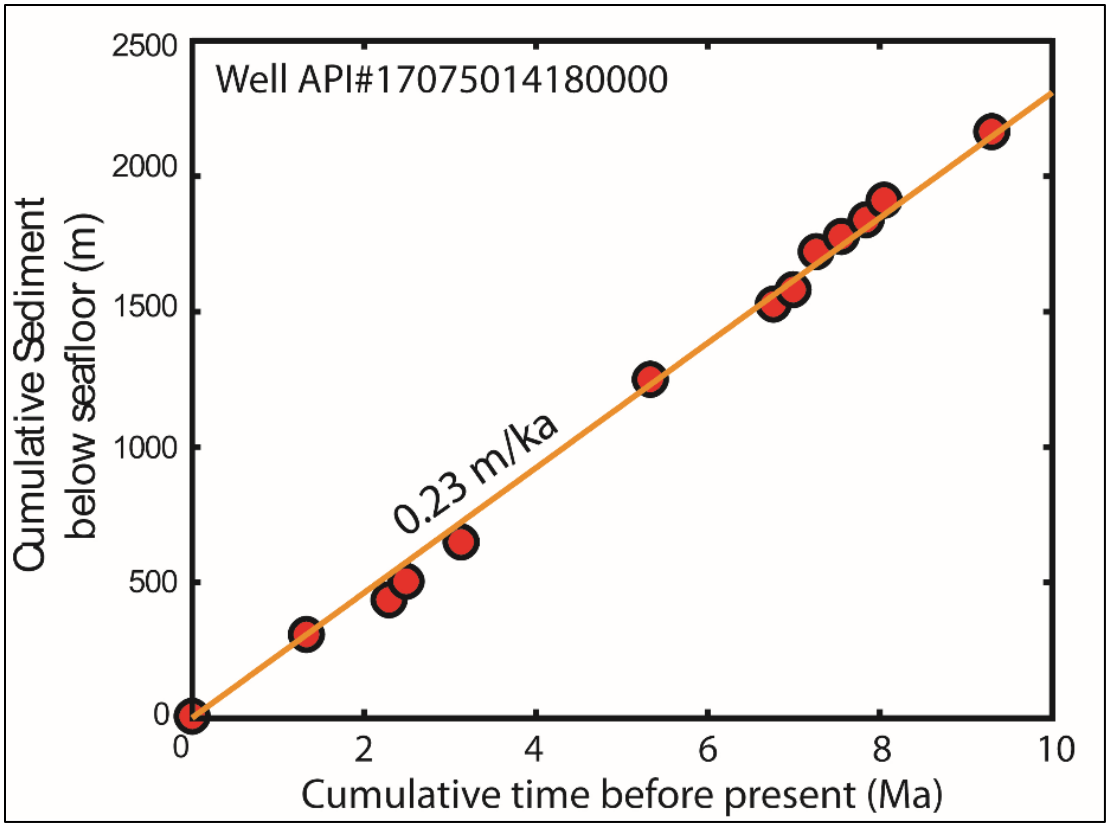

Figure 2.20: Age vs. depth curve from a well within the seismic survey. Figure and data are courtesy of Kyle Straub (Tulane University) and Richard Fillon (Earth Studies Group, LA).

2.8 Mapping channels and valleys

With the channels and valleys clearly imaged using flattened volumes of various attributes, they can then be mapped directly onto the probe top. To define the planform geometry of a channel or valley, a pointset is first created using the digibrush tool in Geoprobe™ that defines the edges of the channelized feature along the entire length of the channel. With the feature's edges defined, the pointset can then be converted to a surface and unflattened to bring it to a configuration that agrees with the original seismic volume. This process gives the planform geometry of the channel or valley and allows width, distance along channel, curvature, slope, and sinuosity to be calculated by recording the coordinates of channel boundaries at consistent intervals along the channel centerline. This interval was never greater than 1 to 2 times the width of the channelized feature being measured. Estimates of channel or valley thicknesses were obtained by defining the difference in time between the roof of the

channel or valley and the thalweg at the same cross section locations where width was recorded. Then, using time vs. depth relationships, time was converted to actual thickness and the width to depth ratio was calculated. Overall, a total length of over 600 km from 43 channels, channel-belts, and valleys was mapped in detail.

For thickness measurements, no attempt to correct for compaction was made. Similar to channels in Mohrig et al. (2000), fluvial deposits in this dataset are primarily sandy and differential compaction effects are not expected to significantly modify channel geometry.

These techniques provide measurements for fluvial geometry as preserved in subsurface data. The preserved stratigraphy, however, does not necessarily represent a fluvial system that existed at any specific point in time. Fluvial stratigraphy is the composite, time transgressive result of erosion and sedimentation. Large fluvial systems imaged in seismic data may be the result of a large channel, the lateral migration of a small channel over a long period of time, or the result of a number of small, concurrently active channels. Additionally, seismic imaging of channels is based on variations in amplitude which may be caused by a number of factors unrelated to fluvial cut and fill processes (e.g., changes in pore pressure, changes in fluid content, the presence of fractures, etc.). If a fluvial system's fill is similar to the surrounding lithology, then there may be no change in amplitude across its boundary and it will not be clearly imaged. These caveats aside, the continuous (i.e. contiguous and mappable over several tens of kilometers) nature of fluvial systems in this dataset provides strong evidence for the robustness of 3D seismic based fluvial analysis.

2.9 Mapping faults

All faults were mapped using GeoProbe's™ ezFault tool (Fig. 2.21) and interpreted using both the amplitude and similarity attribute volume. The similarity volume is ideal for identifying faults because fault planes appear as prominent low similarity zones. Faults were mapped on cross-sections every 4 inlines or crosslines (or with finer detail in areas of high fault complexity). Approximately 28 faults were mapped between 1500 ms and 500 ms beneath the present-day surface. Incomplete seismic coverage in the shallow subsurface precluded fault mapping at less than 500 milliseconds.

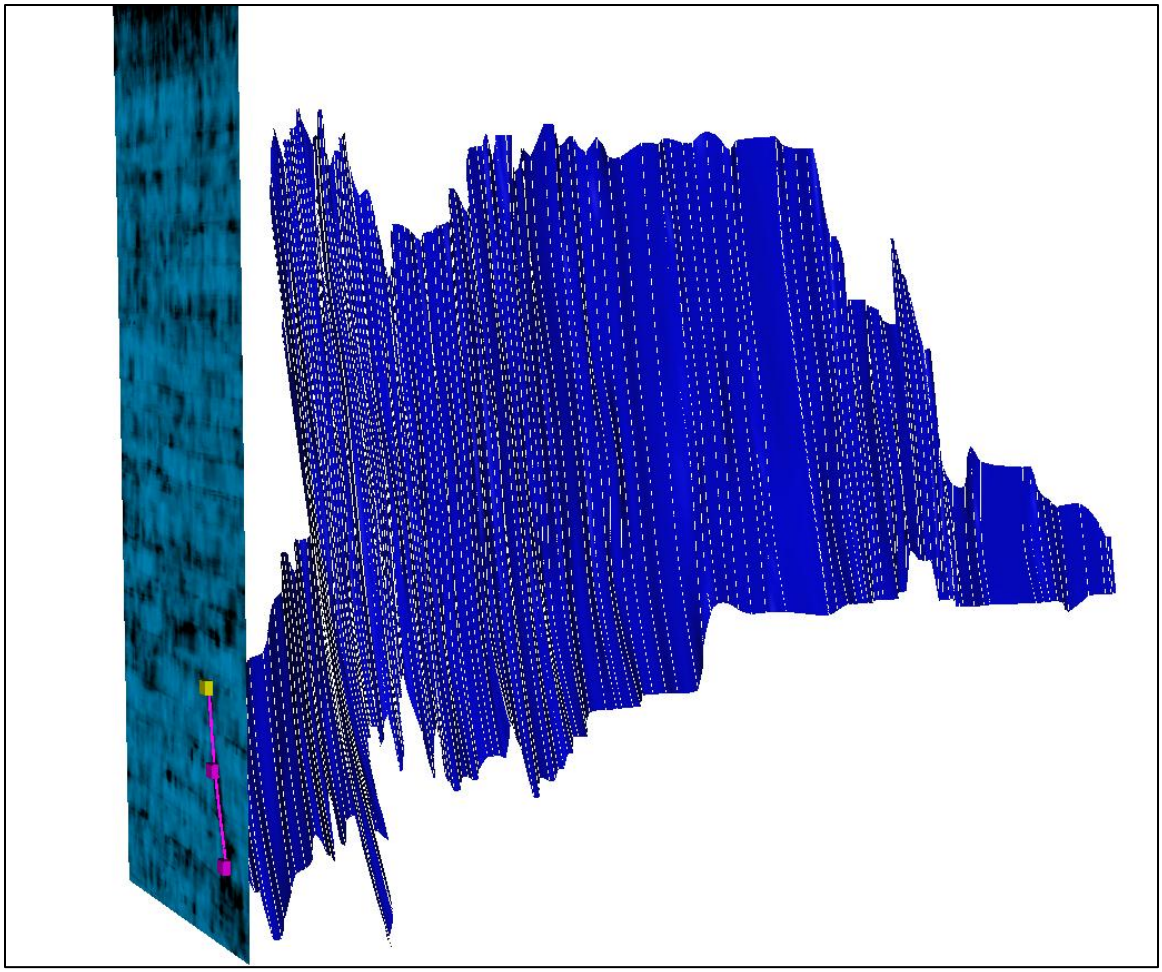

Figure 2.21: Perspective view of a fault being mapped from the similarity volume. Vertical interval shown is ~ 1 km and horizontal length of fault is ~ 10 km.

2.10 Measuring fault and channel-belt relationships

Relationships between faults and channel-belts were examined by measuring any changes in paleo-flow direction where a channel-belt crossed a fault (Fig. 2.22). This was done by approximating the strike of the fault near the valley as a straight line and measuring the coordinates of the line edges. Next, coordinates of a line drawn normal to the fault strike at the channel-belt midpoint along the fault (with the endpoints approximately one channel-belt width upstream and downstream of the fault) were recorded. Additionally, coordinates of a line drawn from the same midpoint (at the channel-belt along the fault strike) to the channel-belt midpoint one channel-belt width upstream and downstream of the fault were recorded. The difference in

angle between the two upstream lines and the two downstream lines was then calculated. This produced a measure of the change in channel-belt orientation across the fault (Fig. 2.22).

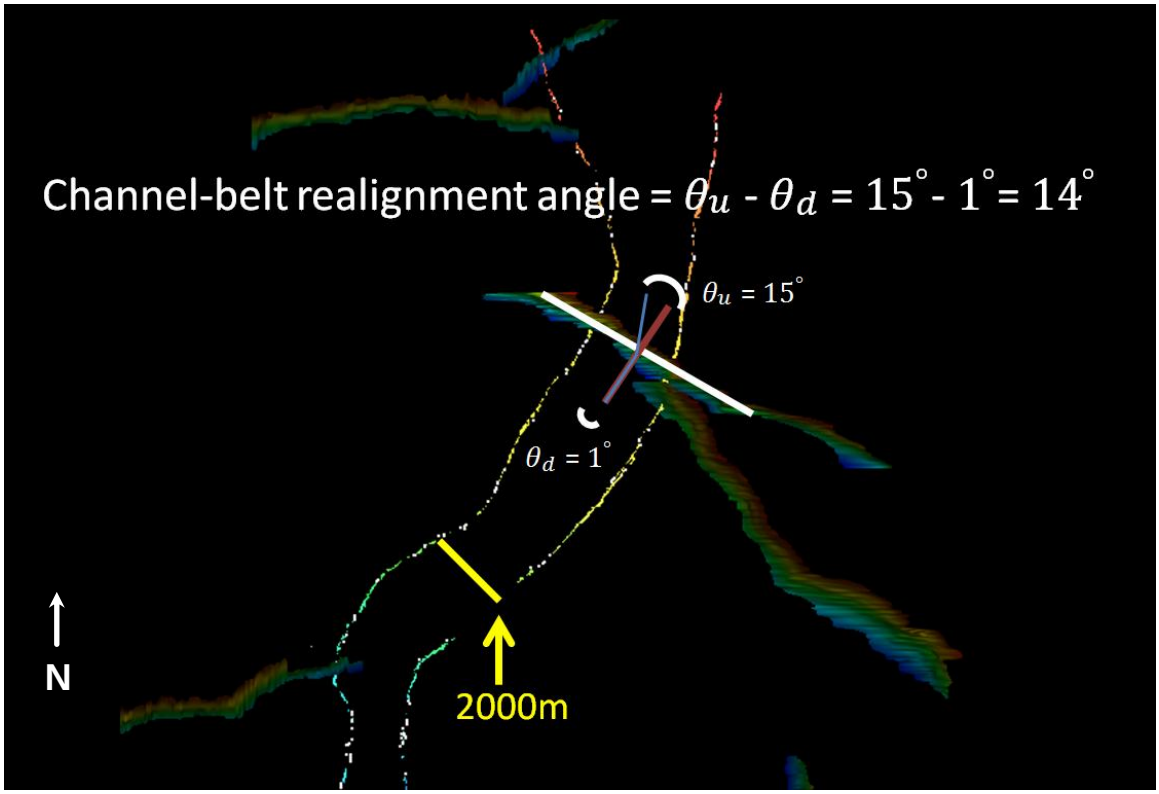

Figure 2.22: Definition of channel-belt realignment angle measured at a fault crossing. The orientation of the channel-belt relative to the strike of the fault is measured both upstream, Θ_u, and downstream, Θ_d, of the structure. View is from directly overhead.

A measure of the magnitude of faulting at each channel-belt location is needed in order to compare the effect of faults on channel-belt systems over differing spatial and temporal intervals. Here this is done using the offset ratio: the local vertical displacement on the fault divided by the depth beneath the present-day surface where this displacement and channel-belt was measured. As fault displacement increases roughly linearly with depth (George, 2008), the offset ratio provides a way to compare displacements throughout the ~ 1500 m studied interval.

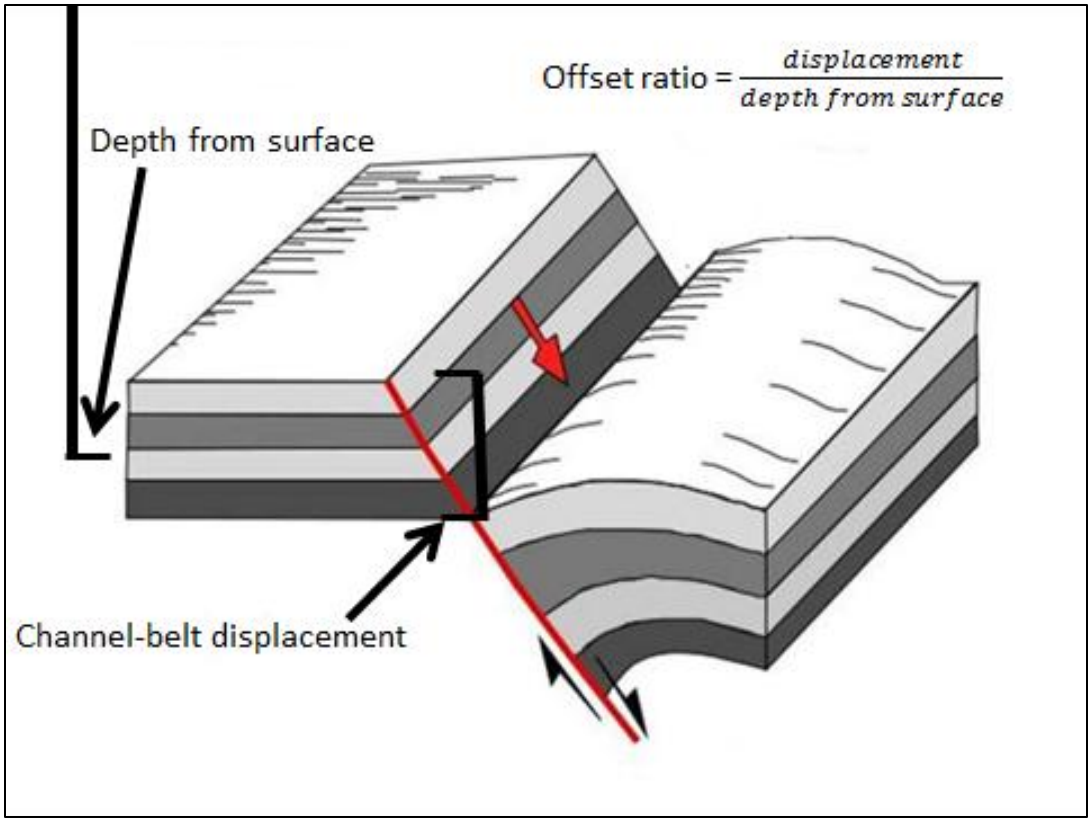

Figure 2.23: Definition of offset ratio (after Gagliano, 2005).

Chapter 3: Fluvial Stratigraphy

3.1 Background

The external morphology of a fluvial channel can be defined by its extent (length, width, and thickness), its shape, and the character of its boundaries (Krynine, 1948). The majority of the literature on the stratigraphic record of fluvial deposits has focused on the internal architecture of channelized deposits, while the study of their external geometry and spatial arrangement has been limited (Gibling, 2006). This lack of work on the planform geometry of stratigraphic channels does not reflect a lack of importance of this data. Information on 3D fluvial form is relevant at least to the disciplines of sequence stratigraphy, basin analysis, and civil and environmental engineering (Bridge and Tye, 2000). Additionally, because a significant number of hydrocarbon reservoirs are contained within fluvial deposits, geometrical constraints and analogues for fluvial systems are of prime economic importance in petroleum exploration and production within fluvial reservoirs (Reynolds, 1999). The study of the channel-form geometries in ancient fluvial systems has been limited by the lack of 3D exposures necessary to collect this information.

Outcrop studies can provide information on numerous features within fluvial systems over a wide range of scales: from millimeter size depositional structures, small to large scale bedforms, larger scale channels and channel-belts, all the way up to the size of the depositional system itself (Miall, 1988). However, the 3D extent of outcrops, even in superbly exposed systems, is limited to a few kilometers at best (e.g., the Guadalope-Matarranya alluvial system at less than 5 km for any channel segment [Mohrig et al., 2000]) and is typically far lower, severely restricting the suitability of outcrops for the study of the planform geometry of ancient fluvial deposits. While the degree of braiding and sinuosity can be inferred from architectural-element analysis (Miall, 1994), the actual planform geometry is still poorly constrained. Well log data is even more laterally restricted than outcrop data and interpretations of planform fluvial geometry are limited by well spacing and rely upon the accurate interpretation and correlation of fluvial deposits between wells (Bridge and Tye, 2000).

With its excellent lateral coverage, 3D seismic data provides the best opportunity for constraining paleo-channel geometry. The discipline of 3D seismic geomorphology has evolved

in recent years to take advantage of the potential for 3D seismic data to image ancient depositional systems as satellites image the modern surface (Wood, 2007). Figure 3.1 shows an example of a late Miocene fluvial system imaged using the WesternGeco® seismic volume.

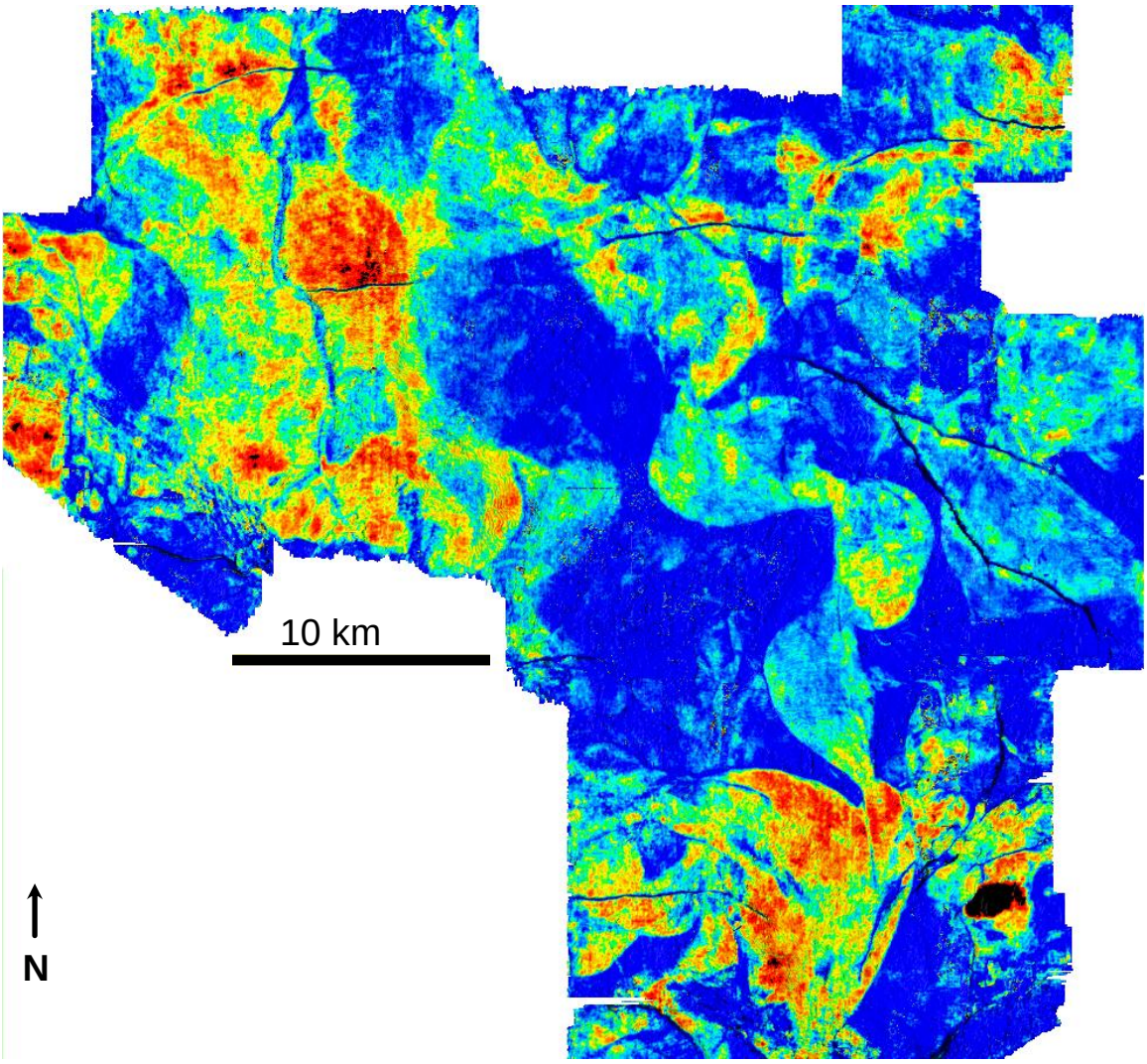

Figure 3.1: Overhead perspective of late Miocene fluvial stratigraphy from the Breton Sound dataset. Hotter colors indicate higher values of the sweetness attribute.

With seismic data, fluvial features have been continuously imaged for distances of several tens of kilometers (e.g., Posamentier, 2001, and this study). However, unlike satellite images, which capture a single surface tied to a specific point in time, seismic images resolve the composite, time-transgressive sedimentary record of depositional events. Importantly, 3D

seismic data can provide a view of an evolving fluvial system over geologically significant time periods.

A number of studies have used the techniques of 3D seismic geomorphology in order to document fluvial geometry as well as changes in fluvial style over time. Among these studies, Wood (2007) provided dimensional data on several dozen Miocene and Pliocene fluvial systems from the Gulf of Mexico. Wood divided these systems into three classes based on their morphometric characteristics and related each class to a specific systems tract (i.e. lowstand, transgressive, or highstand systems tracts), but did not explicitly detail how these systems varied with time. Posamentier (2001) differentiated incised versus unincised lowstand bypass systems of the Miocene through Pleistocene Java Sea Shelf based on the presence or absence of incised tributary valleys feeding the main incised valley. The incised valleys were interpreted to form only when the magnitude of sea-level fall was great enough to expose the entire shelf, an event interpreted as rarely occurring during the Pleistocene due to the lack of evidence for incised tributary valleys during this time. Maynard et al. (2010) examined incised valleys in lower Cretaceous Canadian 3D seismic data and developed a less restrictive set of criteria for incised valley recognition than Posamentier. Maynard et al. (2010) simply defined an incised valley to be any channelized element that is bounded at its base by a sequence boundary. As incised valleys have a distinctive, though apparently variable planform shape and are normally interpreted to result from external forcing, their recognition in 3D seismic data can be used to infer a change in that external forcing. A general definition for incised valleys is given by Zaitlin et al. (1994) as a "fluvially-eroded, elongate topographic low that is typically larger than a single channel form, and is characterized by an abrupt seaward shift of depositional facies across a regionally mappable sequence boundary at its base. The fill typically begins to accumulate during the next base-level rise, and may contain deposits of the following highstand and subsequent sea-level cycles." Implicit in this definition is that incision begins because of a fall in base-level.

This study utilizes a Mississippi River Delta 3D seismic data set with particularly well resolved paleo-channels, channel-belts, and valleys that span an approximately five million year period of time so that the external geometries of fluvial deposits, as well as changes in fluvial style over time, can be measured and analyzed. This information is integrated with well log and

inversion data in order to infer the lithological composition of these fluvial systems. Based upon the established link between external environmental variables and channel geometry and depositional style (Wood, 2007), the data is also used to create a relative sea-level curve for the late Miocene to Pliocene Mississippi River Delta. Additionally, the occurrence of a characteristic vertical scale that separates major observed changes in fluvial stratigraphy through time is investigated.

3.2 Data analysis

Forty-three examples of channelized fluvial bodies were mapped in detail totaling over 600 km of river distance. Widths varied over more than two orders of magnitude, from 100 m to 31,000 m, and thicknesses ranged by about one order of magnitude, from 11 m to 90 m. This section presents two examples of small channels, one example of a channel-belt, one example of a valley, and then details the overall fluvial geometry observed within the dataset.

3.2.1 Channel A

Channel A, a south trending late Pliocene channel (Fig. 3.2), is located in the central portion of the survey and was mapped for over 18 km along the channel centerline. Width ranges from 224 m to 530 m with an average width of 300 m and thickness ranges from 16 m to 26 m with an average thickness of 22 m. The average width to depth ratio is 14. The channel has a sinuosity of 1.22 and has a pronounced bend near the center of its mapped extent where it turns sharply to the northeast. In stratal slice map view the channel appears as a poorly resolved, positive moderate to high amplitude continuous unit. However, using spectral decomposition (Fig. 3.2), the channel is very well resolved between 5 Hz and 40 Hz. Maxima in seismic amplitude tend to occur at channel bends and are particularly strong in these locations at 5 Hz and 40 Hz.

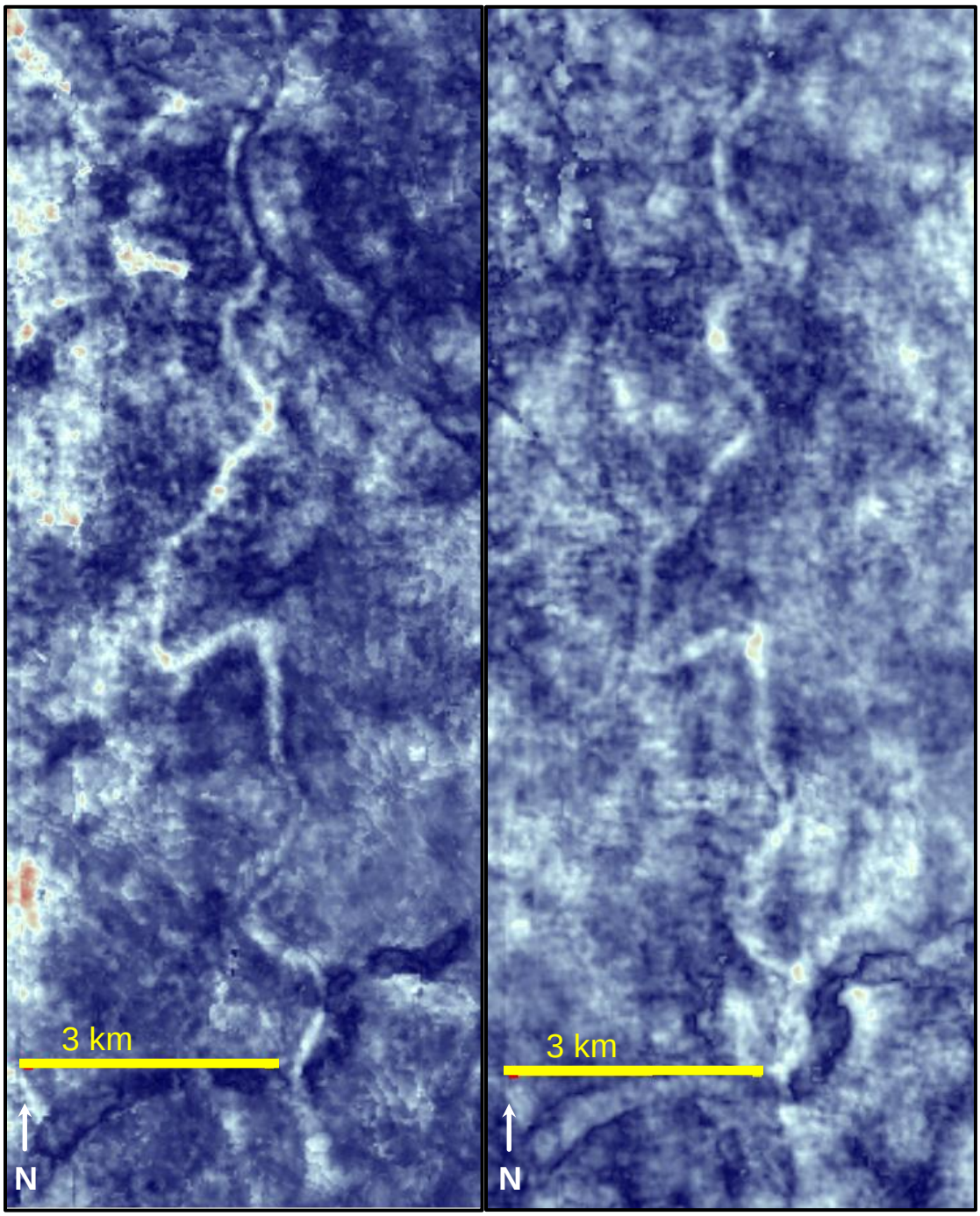

Figure 3.2: Spectral decomposition at 5 Hz (left) and 40 Hz (right). View is from directly overhead. Hotter colors indicate higher amplitudes.

In cross section, the channel can be characterized as a discrete high amplitude positive unit that falls within a positive and laterally extensive reflection (Fig. 3.3). Likely due to limitations in seismic resolution, no internal architecture is imaged within this fill.

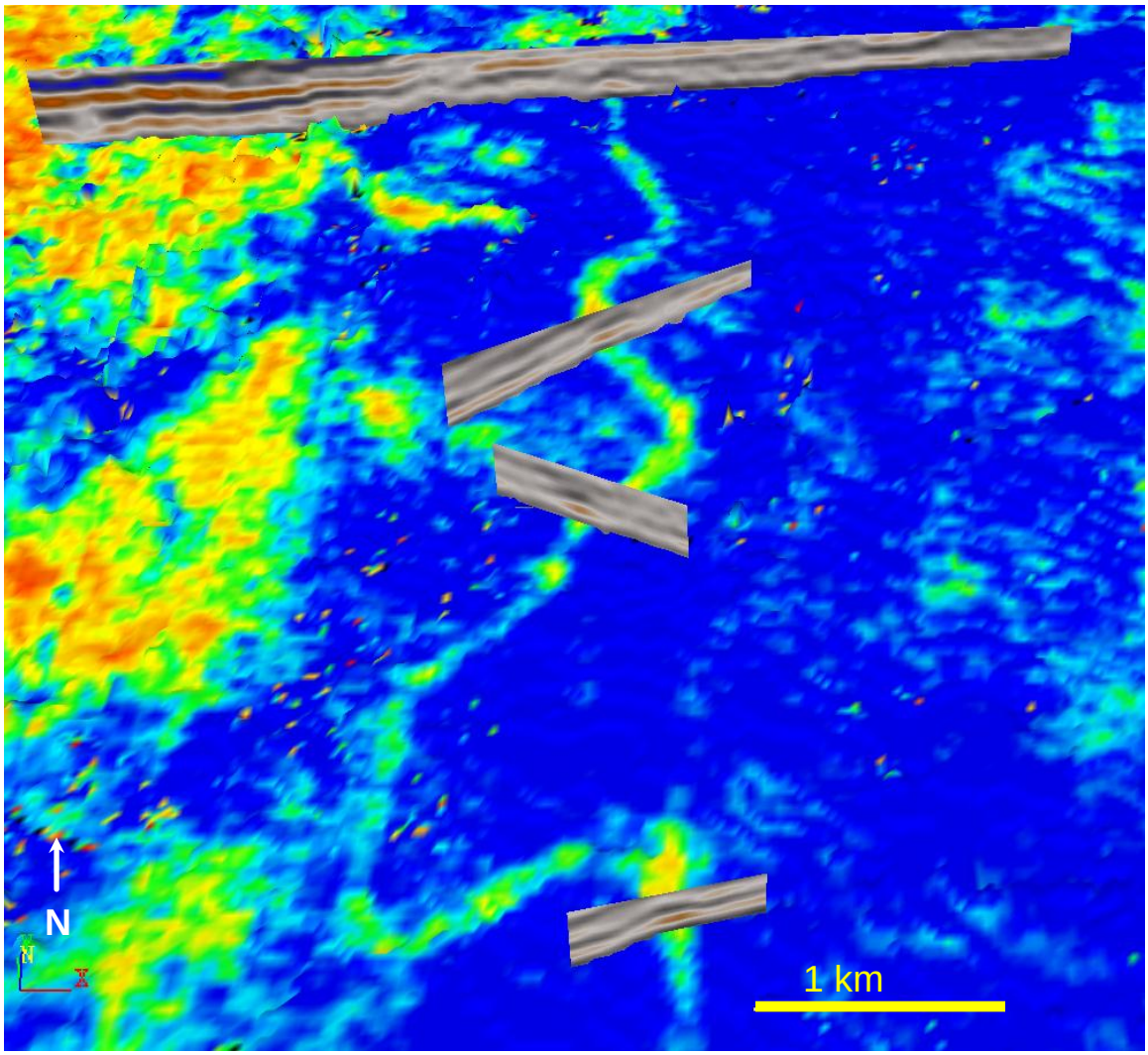

Figure 3.3: Perspective view of Channel A looking (upstream) towards the north. Cross sections show amplitude data and the surface shows sweetness data. In cross section, channel fill appears as high amplitude flat or oval shaped features. The sweetness surface has been moved below its actual location so as not to obscure the cross sections. Hotter colors indicate higher sweetness.

3.2.2 Channel B

Channel B, a southeast trending late Miocene channel, is located in the central portion of the survey and was mapped for over 17 km of channel distance. The average width to depth ratio is 8; width ranges from 100 m to 245 m with an average width of 165 m and thickness ranges from 14 m to 25 m with an average thickness of 20 m. The channel has a sinuosity of 1.5 and crosses an east-west trending, basinward dipping growth fault near the center of its mapped extent. Channel geometry appears to be unaffected across the fault. In spectral decomposition stratal slices, the channel is well imaged from 45 Hz to 60 Hz, with peak amplitude across the majority of the channel at 50 Hz (Fig. 3.4).

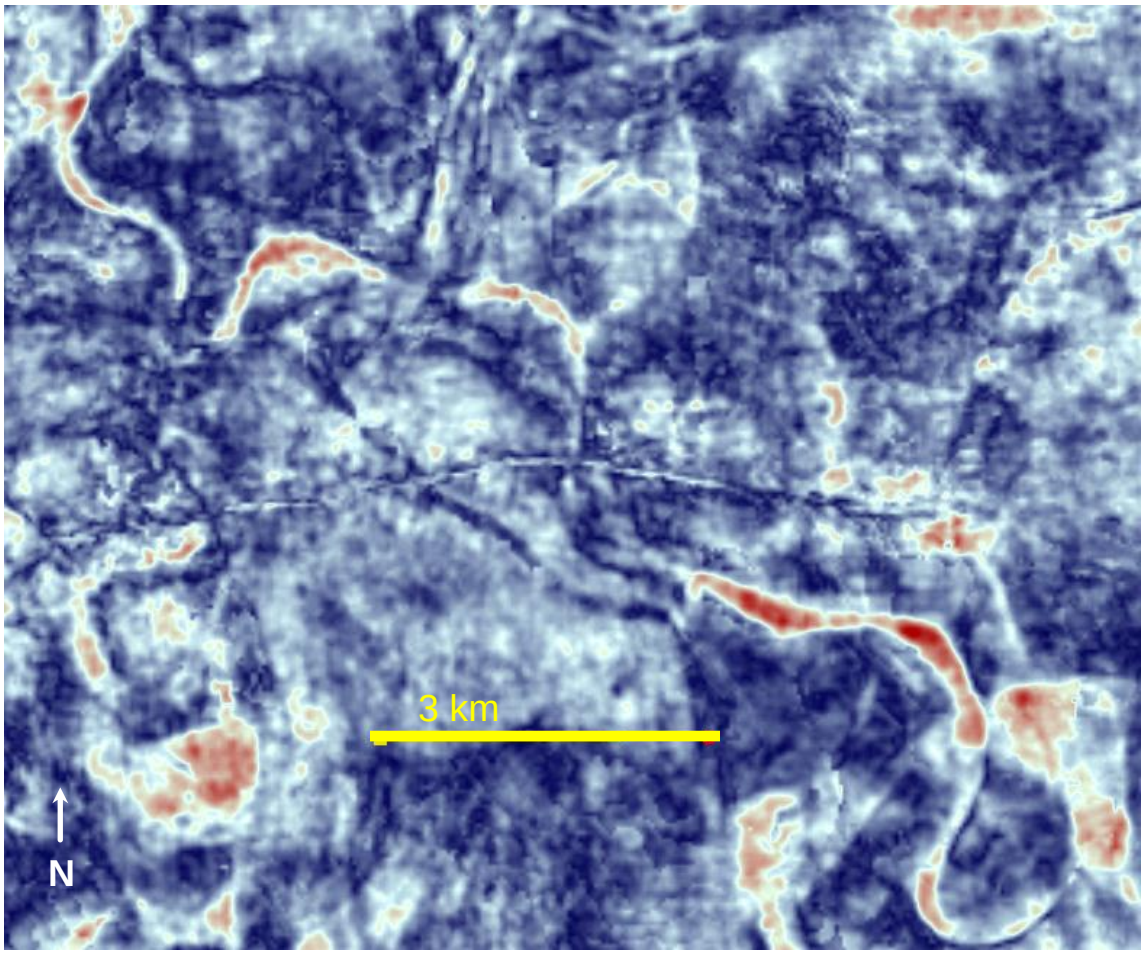

Figure 3.4: Spectral decomposition of Channel B deposits at 50 Hz. View is from directly overhead. Hotter colors indicate higher amplitude.

In contrast to Channel A, which is positioned within a laterally persistent positive reflection, Channel B is an isolated, positive moderate to high amplitude reflector in cross section that is positioned within a laterally extensive negative reflection (Fig. 3.5).

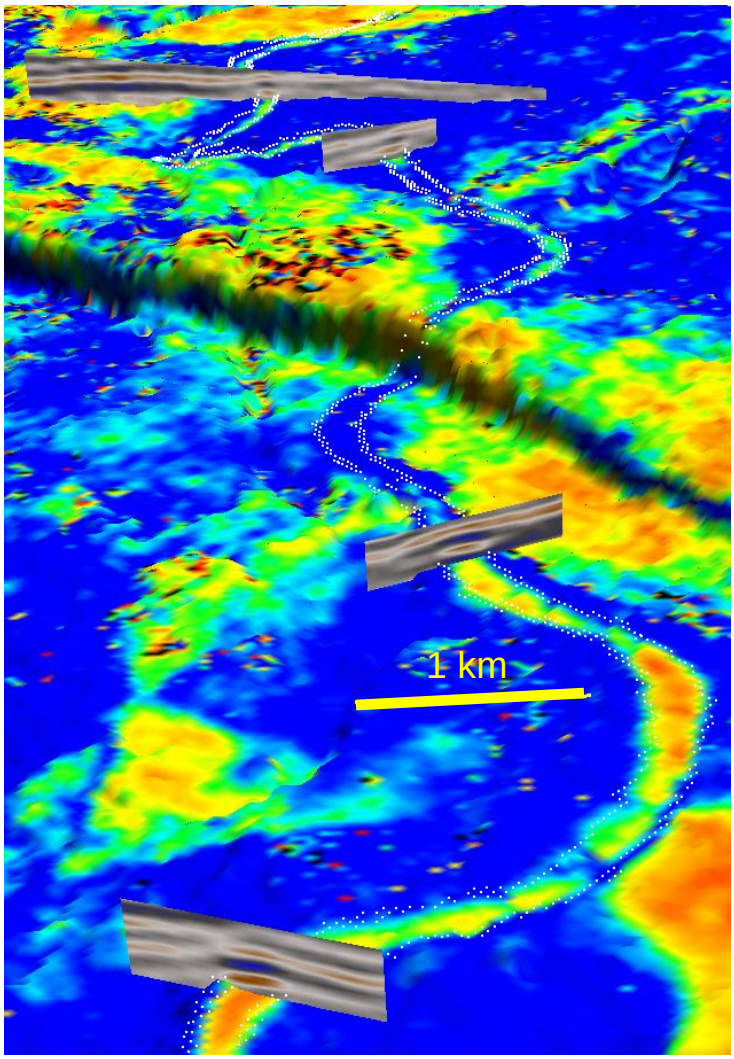

Figure 3.5: Perspective view of Channel B looking upstream toward the northwest. Cross sections show amplitude data and the surface shows sweetness data. The channel crosses an east-west oriented fault in the upper half of the image. The channel edges are outlined with white dots and channel fill appears as isolated, positive high amplitude flat or oval shaped features in cross section. The sweetness surface has been moved below its actual location so as not to obscure the cross sections (hotter colors indicate higher sweetness).

3.2.3 Channel-belt C

This south trending late Miocene channel-belt is located in the west portion of the survey and was mapped for over 27 km channel distance. The average width to depth ratio is 67; width ranges from about 1650 m to 5540 m with an average width of 3195 m and thickness ranges from about 25 m to 60 m with an average thickness of 48 m. The channel-belt has a sinuosity of 1.56 and crosses an east-west trending regional growth fault approximately 2 km downstream of its northern-most mapped position and partially crosses a counter regional growth fault near the center of the mapped portion of the channel-belt. No clear changes in geometry are observed around these faults. The channel-belt is well imaged in the amplitude volume, appearing as a positive, moderate to high amplitude continuous unit (Fig. 3.6) on stratal slices.

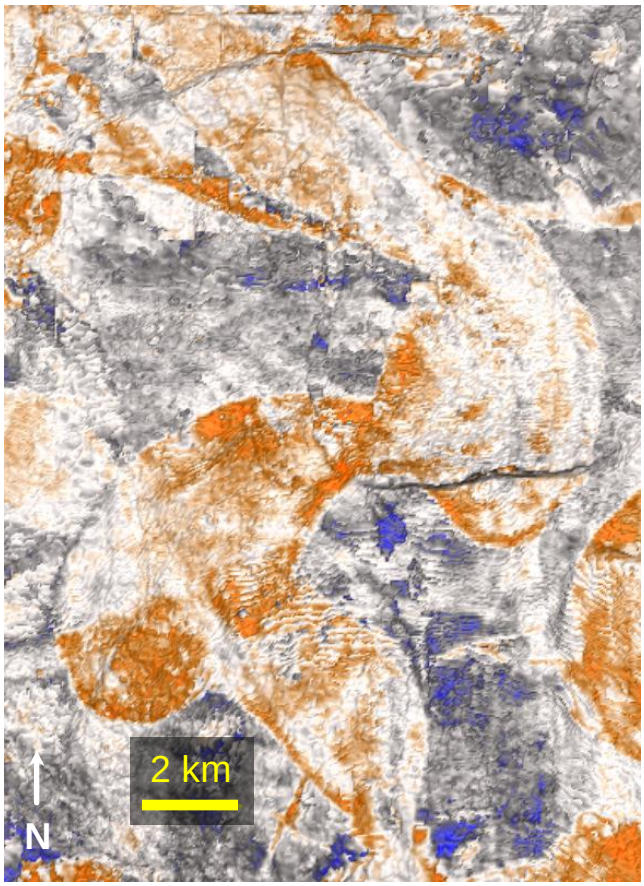

Figure 3.6: Channel-belt C observed on an amplitude stratal slice (hotter colors indicate positive high amplitudes). View is from directly overhead.

Using the spectrally decomposed seismic volume, the channel-belt edges are best defined at 35 Hz (Fig. 3.7). However, this example does not show a strong response throughout the channel-belt at any one frequency. Instead, the channel-belt has a low to moderate amplitude response over a broad range of frequencies.

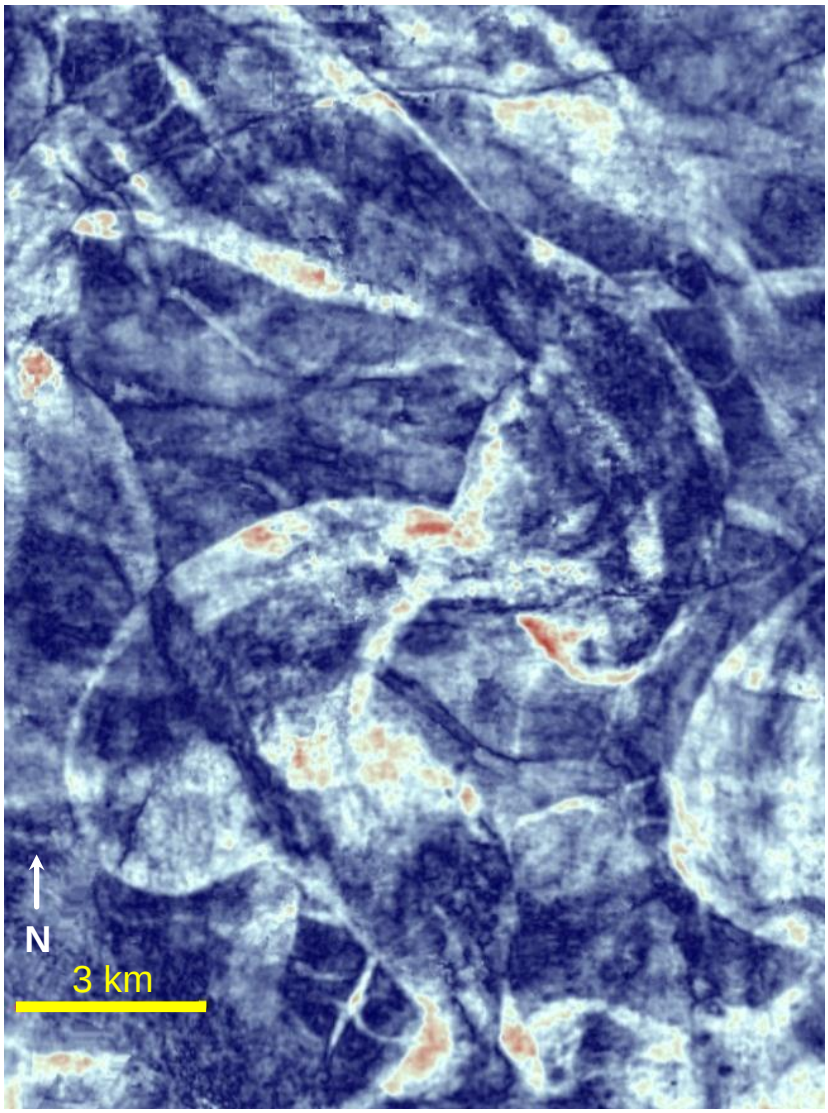

Figure 3.7: Spectral decomposition of Channel-belt C at 35 Hz. Hotter colors indicate higher amplitudes. View is from directly overhead.

A younger, narrow (290 m average width) southeast trending channel cuts across the southern half of Channel-belt C and is observed eroding into the upper surface of the channel-belt (Fig. 3.8).

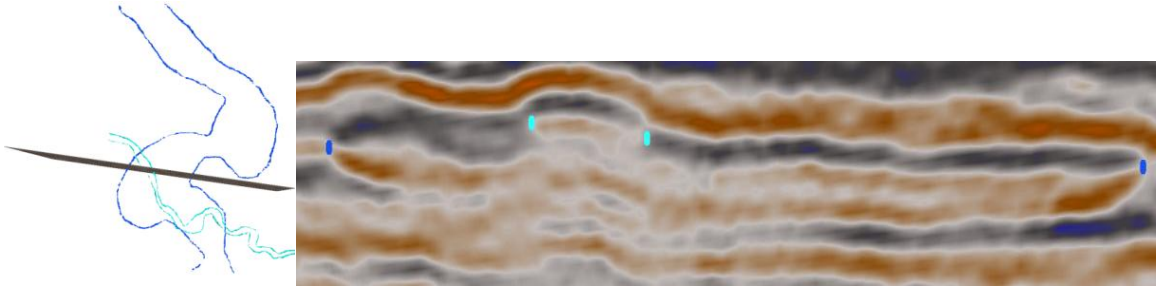

Figure 3.8: (Left) Cross section location through Channel-belt C and the smaller overlying channel. (Right) A ~ 3 km amplitude cross section (looking upstream to the north) with the upper channel edges marked in light blue and the channel-belt edges marked in dark blue.

Five wells intersect Channel-belt C and define its fill as single story and blocky. The northern most well (Fig. 3.9, cross section A) has a 34 m thick, blocky low gamma ray fill with a sharply defined high gamma ray base and cap. The ~ 50 m immediately below the fill is also sandy but is separated from the channel-belt by a thin (~ 1m) spike in gamma ray intensity and a relative decrease in porosity. This basal boundary correlates with a change in impedance at the base of the channel-belt. Fill porosity is generally around 45% and decreases to about 40% in the uppermost few meters of fill along with a corresponding increase in gamma ray, likely indicating an increase in mud content. The well shown in cross section B has a 34-m thick blocky, low gamma ray fill with a sharp base and a sharp cap. Three wells are shown in cross section C. The most updip well on cross section C shows a 27 m thick sandy fill with the upper 15 m displaying a coarsening up gamma ray log pattern and sharp base and cap. The approximately 38 m thick low gamma ray fill in the central well is blocky with a sharp base and cap. The south most well has 25 m of low gamma-ray value fill and fines upwards.

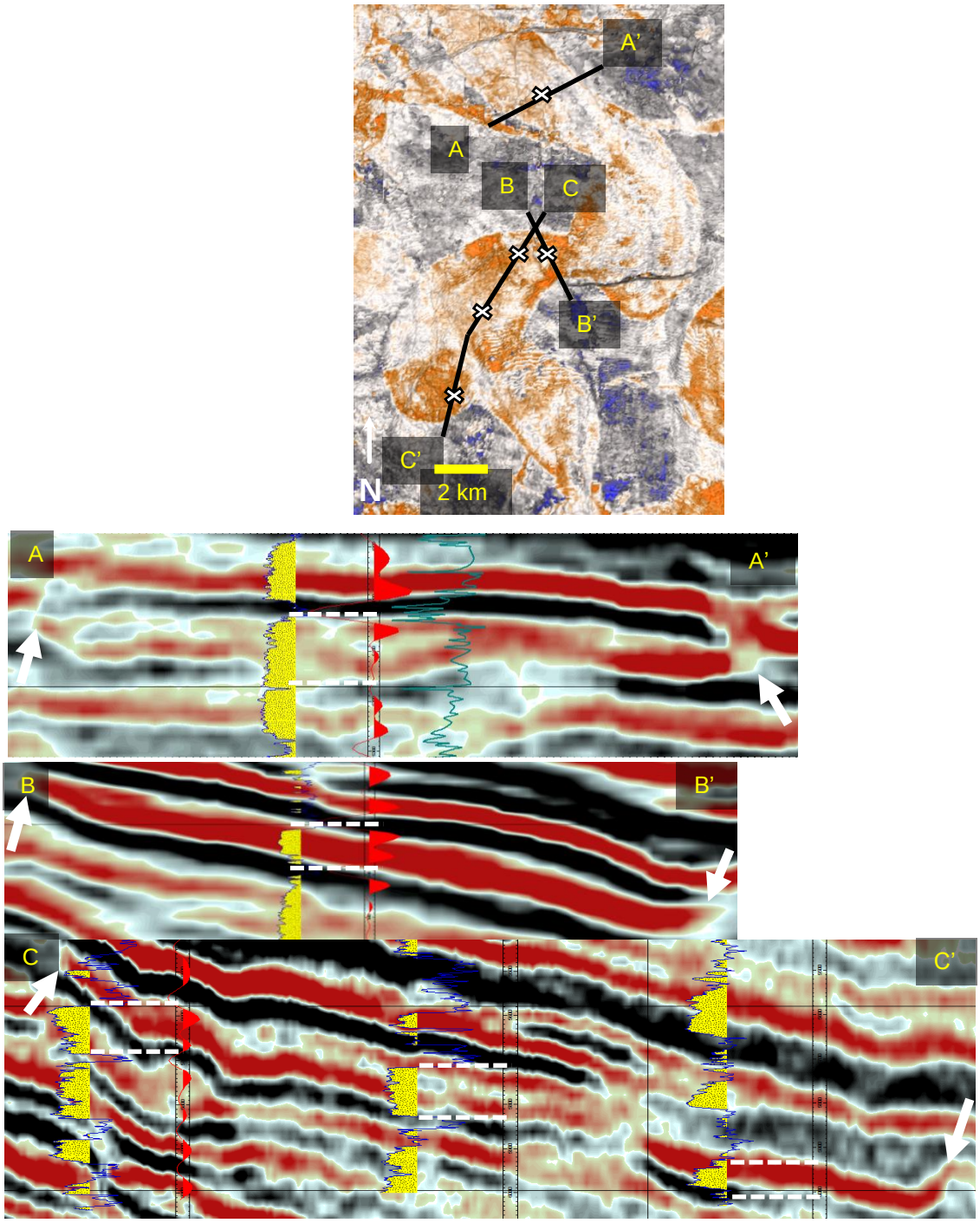

Figure 3.9: Channel-belt C cross sections with well logs. Gamma ray values < 60 are shaded in yellow; dotted white lines connect curve projections to actual well intersections. A teal colored porosity curve is also presented in cross section A. White arrows point to channel-belt edges.

3.2.4 Valley D

This large, late Miocene valley trends southwest and can be followed for several tens of kilometers to the southwestern edge of the survey. It is one of the largest mappable valleys in the dataset with a width up to 31 kilometers and thickness up to 78 meters. Average width is 19.5 km and average thickness is about 68 m; the average width to depth ratio is 287. The valley widens significantly downstream where there is a sharp southeast bend to the east side of the valley. This bend may be genetically unrelated to the main valley but this discrimination is ambiguous based on the seismic data. Upstream of this bend, the average width is 13 km; downstream of the bend, the average width is 30 km. On an amplitude stratal slice this valley appears as a well-defined moderate positive amplitude unit bordered by both negative and positive high amplitude reflections (Fig. 3.10, upper image). In similarity, the valley appears as a well-defined low similarity zone bounded by high similarity areas (Fig. 3.10, lower image).

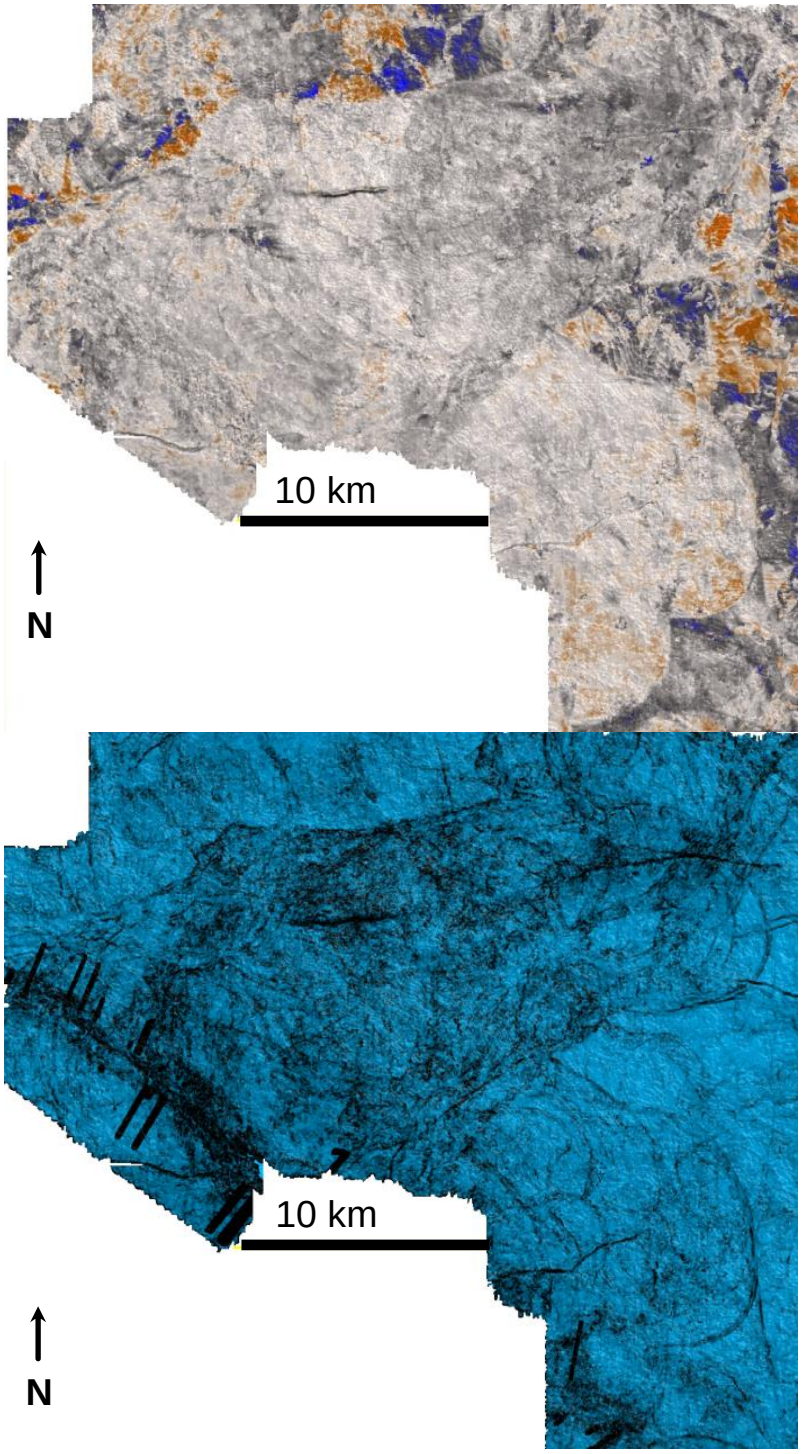

Figure 3.10: (Upper) Amplitude stratal slice highlighting Valley D (hotter colors indicate higher amplitude). (Lower) Similarity stratal slice showing Valley D (darker colors indicate lower similarity). View in both maps is from directly overhead.

In spectral decomposition, the valley body does not appear as a cohesive unit at any frequency. Instead, valley response is spread out over a broad range of frequencies and appears as a collection of moderate amplitudes from 15 Hz to 65 Hz. Figure 3.11 shows the valley at 20 Hz and again at 45 Hz. The highest amplitudes are found just outside the valley boundaries.

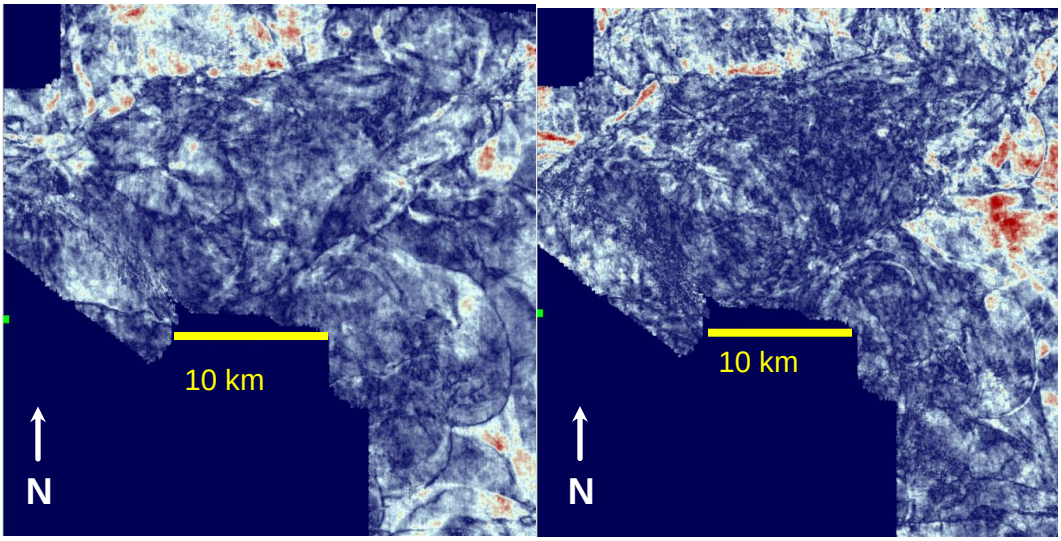

Figure 3.11: Valley D at 20 Hz (left) and at 45 Hz (right). View is from directly overhead. Hotter colors indicate higher amplitude.

In cross section, the valley appears as an isolated, moderate to high amplitude reflection with more "cut and fill" seismic character than observed in the three previously described elements. Five wells intersect the valley and show thick (46 m to 71 m), generally sandy fill. The valley fill tends to be blocky but can fine upwards, with each well showing 1 to 5 stacked units within the fill (and each of these units shows clear high gamma ray bases and caps). The well shown in cross section A, (Fig. 3.12, upper) has 48 m of blocky sand. The valley fill here appears as two stacked units: a lower coarsening up section, and an upper, thicker blocky section. Three wells are shown in cross section B (Fig. 3.12, middle). The most updip well shows 46 m of sand that consists of two blocky stacked units with porosity of around 35%. The central well shows 66 m of highly variable fill with at least 5 stacked units. The south most well in cross section B consists of two stacked units (71 m thick) with a lower blocky unit and an upper finer unit. The well shown in cross section C (Fig. 3.12, lower) is a single, 53 m unit of blocky sand.

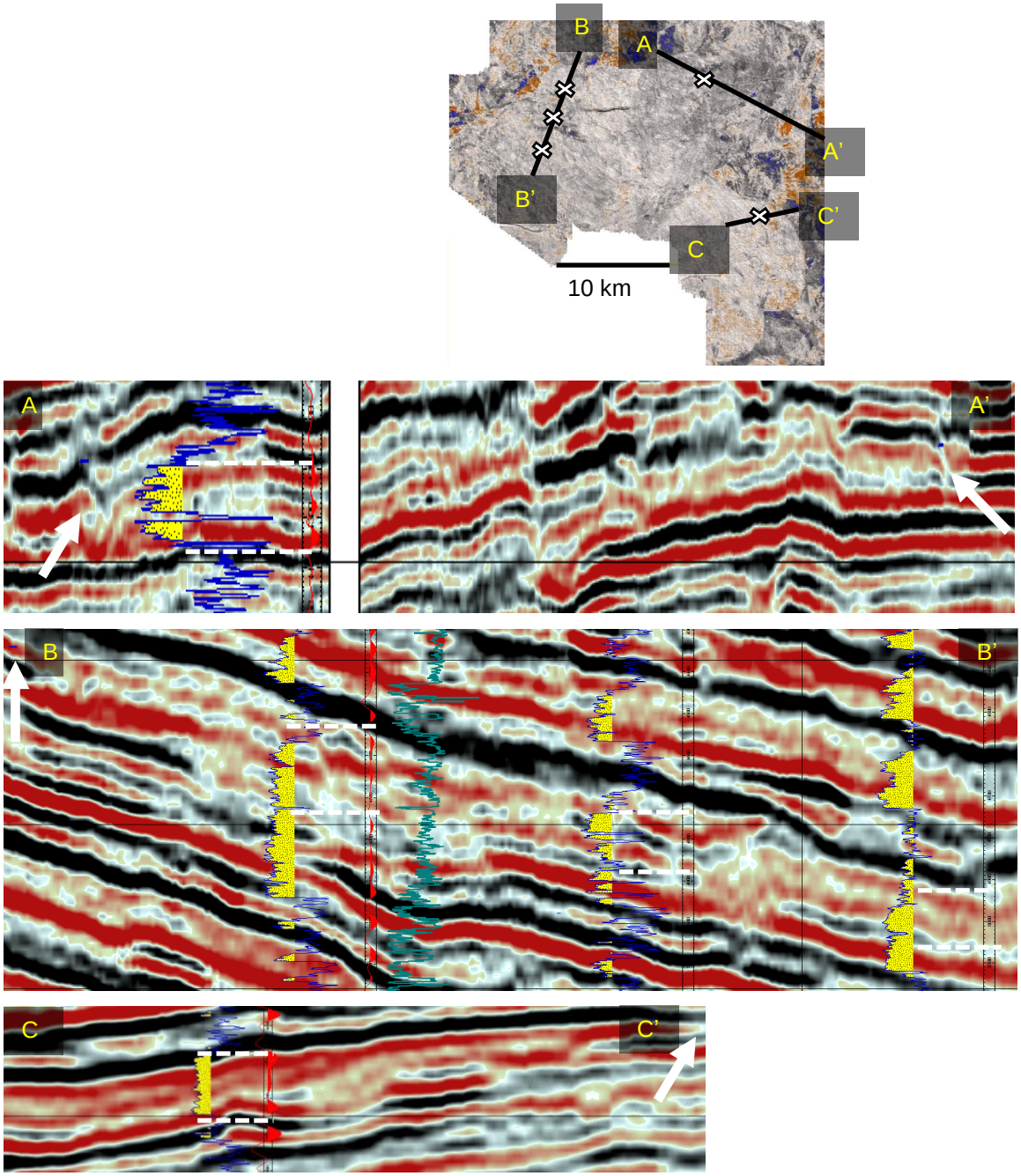

Figure 3.12: Valley D cross sections with well logs. Gamma ray values < 60 shaded in yellow; dotted white lines connect curve projections to actual well intersections. Porosity curve (in teal) shown in cross section B. Arrows point to valley edges.

3.2.5 Width to depth relationships

The average width and depth (i.e. thickness) was calculated from each of the 43 fully mapped channelized fluvial elements. Width ranges from around 67 m to 31,000 m and depth ranges from 11 m to 90 m. When plotted (Fig. 3.13), the channelized bodies from this dataset follow a power-law scaling relationship between width and depth. Trend-lines for the minimum and maximum width and depth are also derived from the data set. These show that upper and lower limits on fluvial geometry follow a similar power law scaling relationship. These curves provide a locally tuned relationship between width and depth for fluvial stratigraphy in this study area and interval of interest.

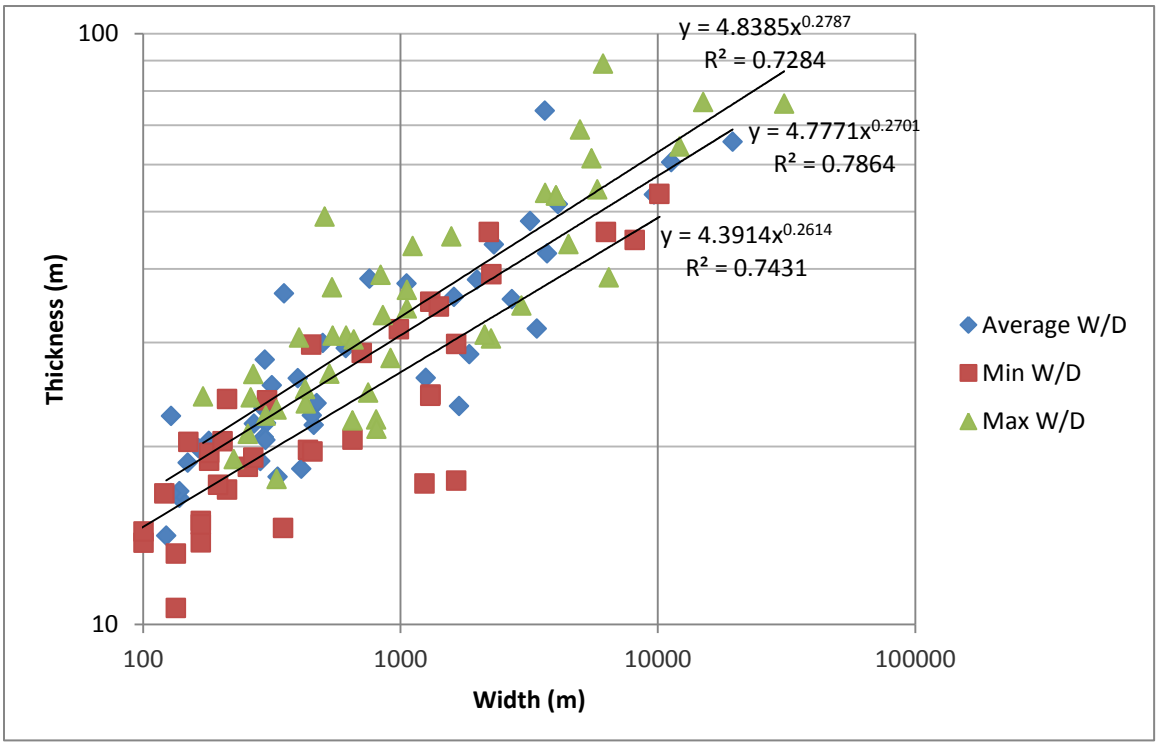

Figure 3.13: Average, minimum, and maximum values for width and depth from the 43 fully mapped channelized elements in the study volume.

Figure 3.14 shows the cumulative frequency distribution of width to depth values. Ninety percent of the fully mapped fluvial elements have a width to depth ratio less than 100. However, many of the largest valleys are not entirely contained within the seismic volume preventing the very high width to depth ratios of these systems from being included.

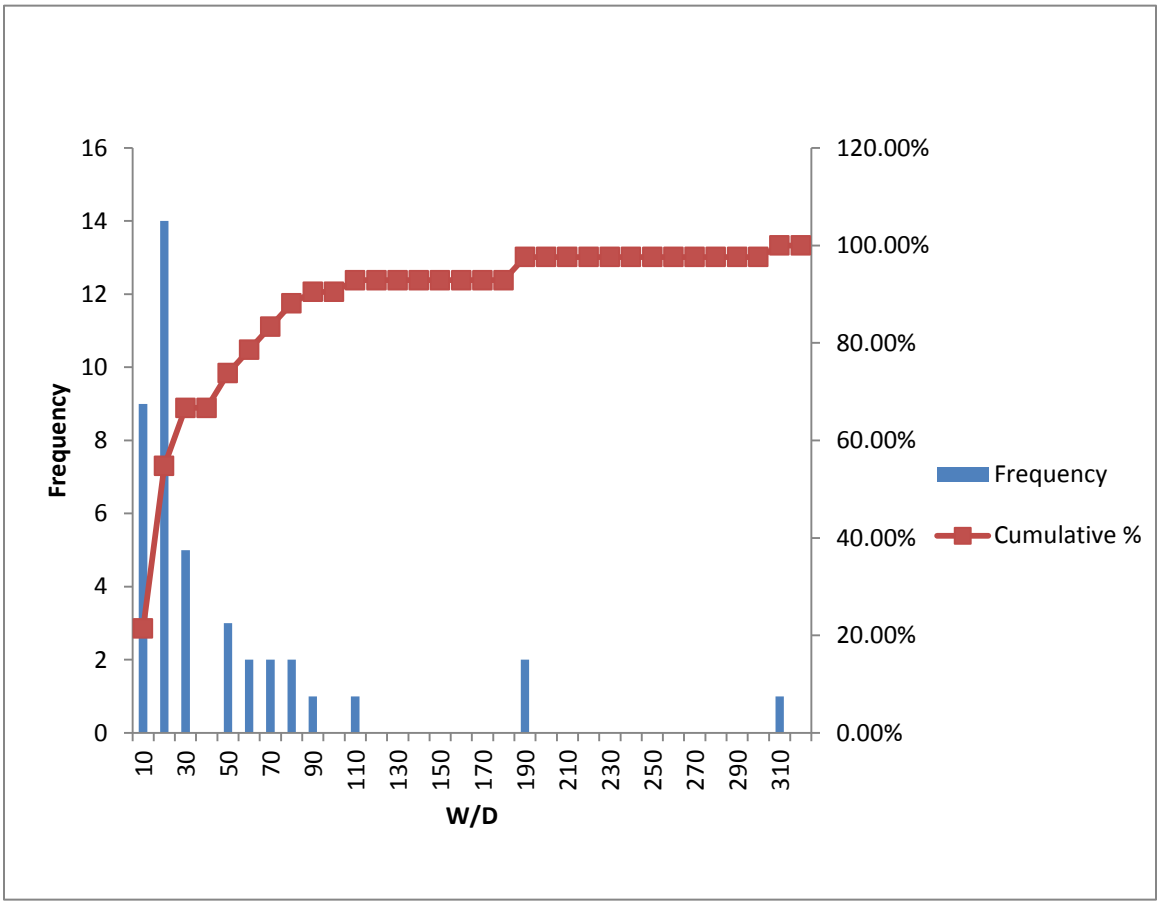

Figure 3.14: Width to depth histogram and cumulative frequency distribution for the 43 fully mapped channelized elements in the study volume.

3.2.6 Sand content in the Mississippi River Delta

From the 17 wells that contain gamma ray curves, sand percentages for each well can be estimated by defining all gamma ray values that fall below a certain level as sand beds. Sand percentages were calculated for the entire late Miocene to Pliocene interval for each well. The stratigraphic thickness analyzed from each well ranged from 600 m to 1900 m in depth, depending on the completeness of the GR log from each well. The overall sand percentage calculated using all 17 wells is 64.6% for a cutoff defining all strata with < 70 API gamma ray units as sand. With a more conservative cutoff value of 50 API gamma ray units, the overall sand percentage is lowered to a still significant 41.4%. The log-based estimates have not been corrected for any sediment-compaction effects. Figure 3.15 shows an approximately 700 m thick sand rich seismic cross section with gamma ray curve.

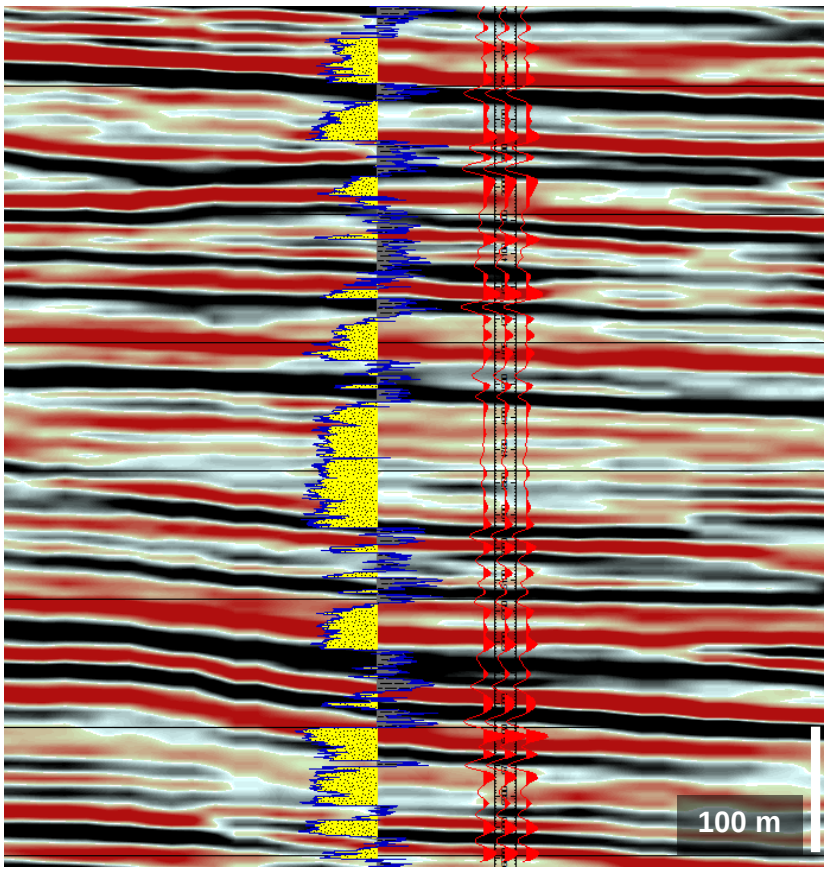

Figure 3.15: Approximately 700 m thick cross section showing high sand content in gamma ray curve. Cutoff for sand (shaded yellow) is 70 API gamma ray units.

3.2.7 Influence of antecedent topography

Alluvial ridges are topographic highs formed by abandoned channels that, if not covered by floodplain sediments, may act to guide younger channels (Mohrig et al., 2000). Figure 3.16 shows an example of a channel-belt influenced by topography inherited from an older abandoned channel-belt. For a distance of 4 km downstream of the bifurcation of the older channel-belt (shown in blue), the west edge of the younger system (shown in red) closely tracks the east edge of the older system. This is likely due to the presence of a levee on the older channel-belt which acted as a barrier to the younger channel-belt. As shown in cross section, the two channel-belts are separated by only a few meters of coastal plain muds. Interestingly, the younger channel-belt is deflected upwards as it approaches the older channel-belt. This deflection may be due to the presence of the alluvial-ridge, the general concave up character of channelized systems, or to differential compaction of muds under the younger channel-belt which decreases as it approaches the sandy fill of the older system.

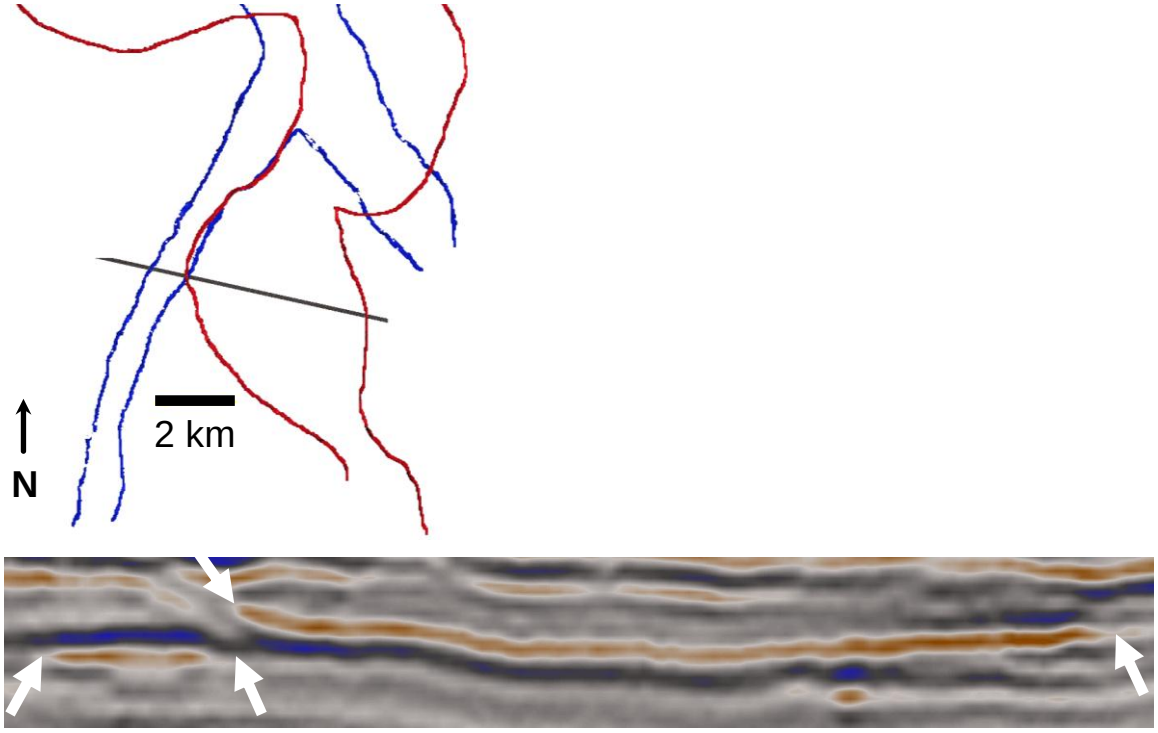

Figure 3.16: Influence of inherited topography. Upper image shows outlines of channel-belts; red demarcates the younger of the two belts. Lower image shows the marked amplitude cross-section looking to the north; arrows point to the identifiable channel-belt edges.

3.2.8 Fluvial styles by surface

Stratal slice analysis of an approximately 1300 m thick sedimentary succession reveals 21 distinct depositional events. Twenty of the twenty-one events display a dominant style of fluvial stratigraphy that falls into one of three categories: 1) incised valleys, 2) channel-belts, or 3) strongly distributive networks of channels. One slice shows an almost unchannelized surface with little lateral variation in amplitude. While there is additional channelized stratigraphy that falls between these 21 stratal slices, these surfaces appear to represent the most pronounced depositional events as well as the most unambiguous representations of each fluvial style. A representative example of each of the three fluvial styles is shown in the following:

3.2.8.1 Incised valley surface

This early Pliocene incised valley (Fig. 3.17) is clearly imaged for a length of over 40 km on a surface located at an average depth of 1070 m. The valley is oriented directly north-south with its widest portion (~ 32 km width) located at the center of the survey. The valley narrows to the north and south of this maximum width (to a minimum width of ~ 14 km to the north) and then appears to widen again to the north outside of the survey boundaries. The west side of the southern half of the valley is not imaged because it falls outside of the survey boundaries as well. Valley thickness averages about 62 m. On stratal slices, the valley appears as a well-defined, positive high amplitude continuous unit. Seismic amplitude-lithology relationships suggest that the valley is primarily filled with sand. While the dominant stratigraphic signal of this surface is the valley, another fluvial style is also present. The valley appears to be cut into a network of narrow distributive channels, some of which are preserved to the east of the widest portion of the valley.

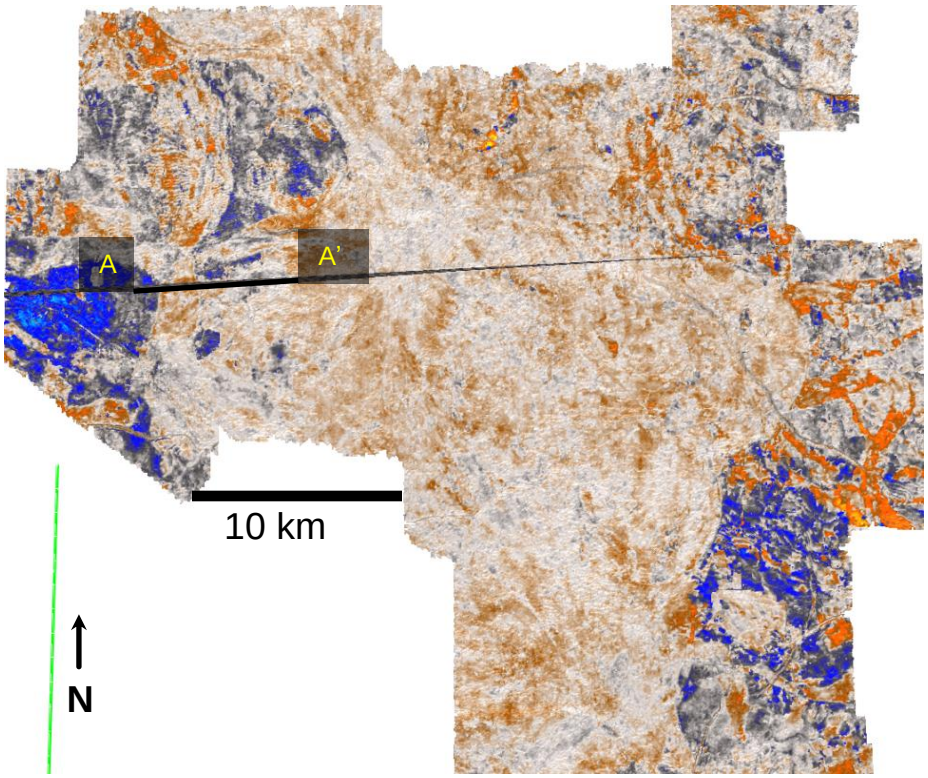

Figure 3.17: Map of the representative valley on an amplitude stratal slice.

Valley systems are of such significant size that their internal architecture can sometimes be directly imaged in the seismic data. Figure 3.18 shows a series of inclined reflections that dip towards the west edge of the valley.

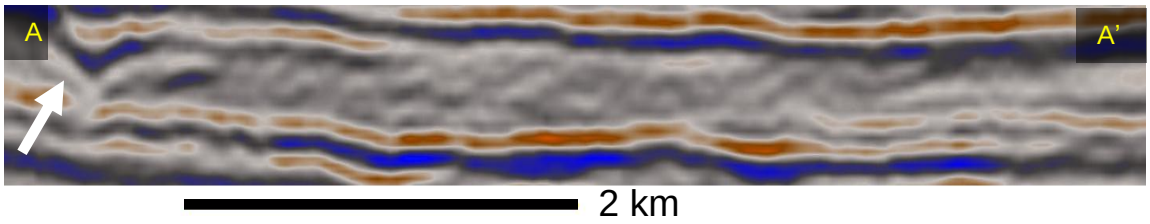

Figure 3.18: Amplitude cross section showing inclined reflectors in valley fill (dipping to left). Valley thickness is approximately 60 m. Cross section location is shown in Figure 3.17. Arrow shows west edge of the valley.

3.2.8.2 Channel-belt surface

Figure 3.19 shows four separate examples of upper Miocene channel-belts located on a single surface at approximately 1500 m depth. Each of these channel-belts extends basinward with little apparent variation in paleo-flow direction. Widths range from an average of 300 m for the westernmost channel-belt to between 1 and 3 km for the other three channel-belts. Thicknesses average about 25 m for the western most channel-belt and 25 to 35 meters for the other three channel-belts. The eastern most channel-belt bifurcates into two main trunks towards the southern part of the seismic survey area. No wells intersect these features; however, seismic lithology relationships suggest they are composed of primarily sandy (high amplitude) fill. In addition, although variability can be significant, impedance and porosity inversions (Fig. 3.20) indicate low-impedance, high-porosity fills, a signature of sand within this dataset.

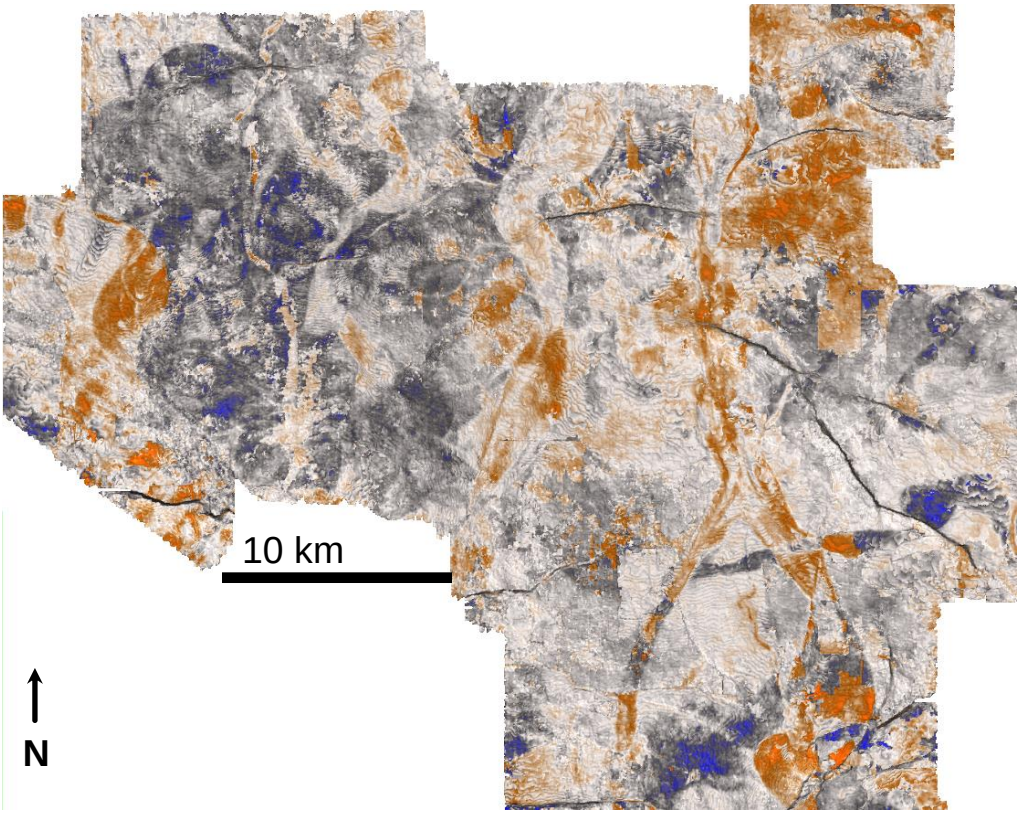

Figure 3.19: Four channel-belts on an amplitude stratal slice. View is from directly overhead.

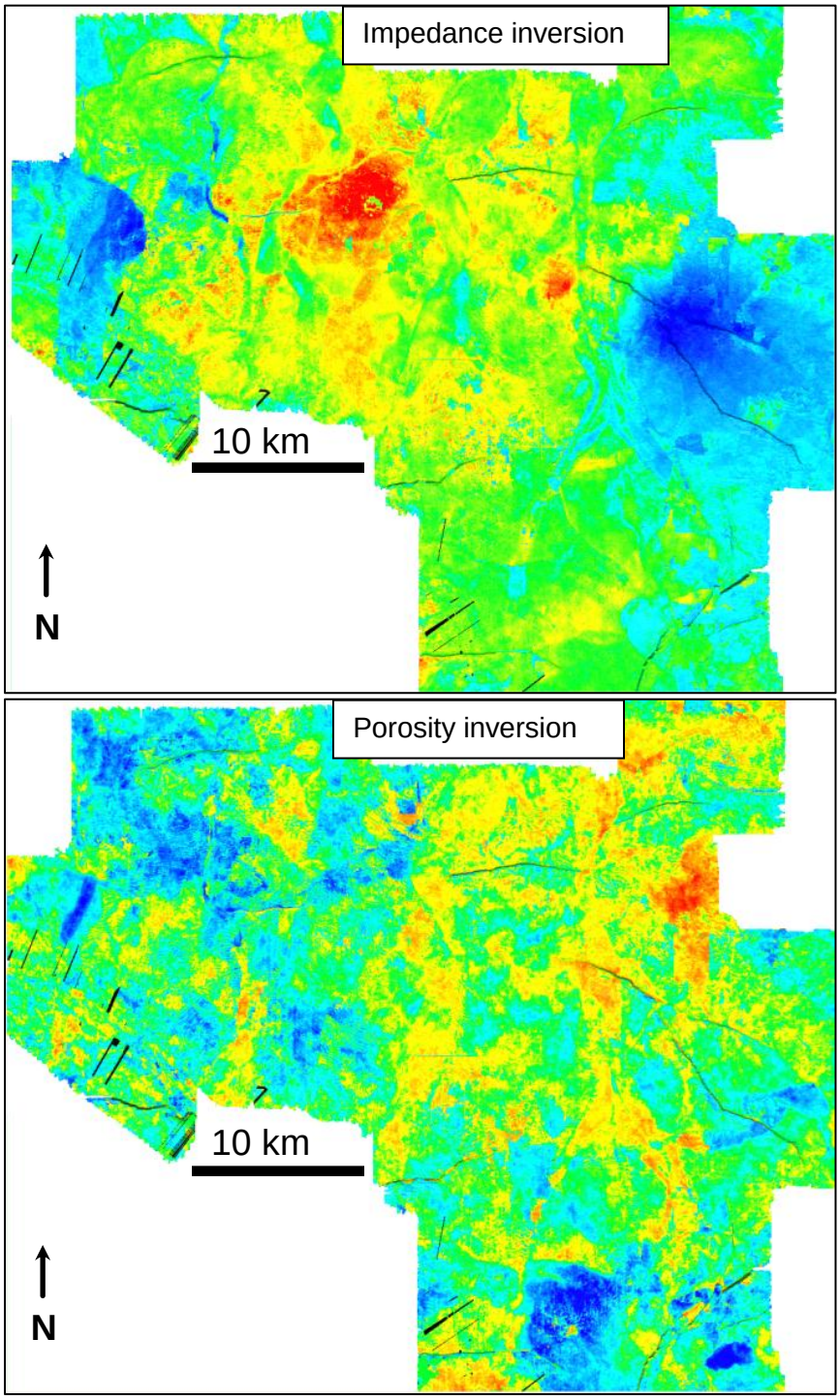

Figure 3.20: Impedance and porosity inversions of the stratal slice with the four channel-belts shown in Figure 3.19. Hotter colors indicate higher values for impedance and porosity. Porosity ranges from about 20% to 40%. View is from directly overhead.

3.2.8.3 Distributive channel network surface

Figure 3.21 shows an example of a complex network of narrow (one to several hundred meters wide) channels located on a surface at an average depth of 1016 m. Channel thicknesses, with most less than 15 m, are among the smallest imaged by this seismic survey. This fluvial style displays high variability in paleo-flow direction with many channels oriented east-west, a trend rarely seen in larger channel-belt and valley systems in the dataset. In the southwestern portion of this example, the eastern edge of a valley appears to cut into the network of distributive channels resulting in both valley and distributive network fluvial styles being present on the same surface.

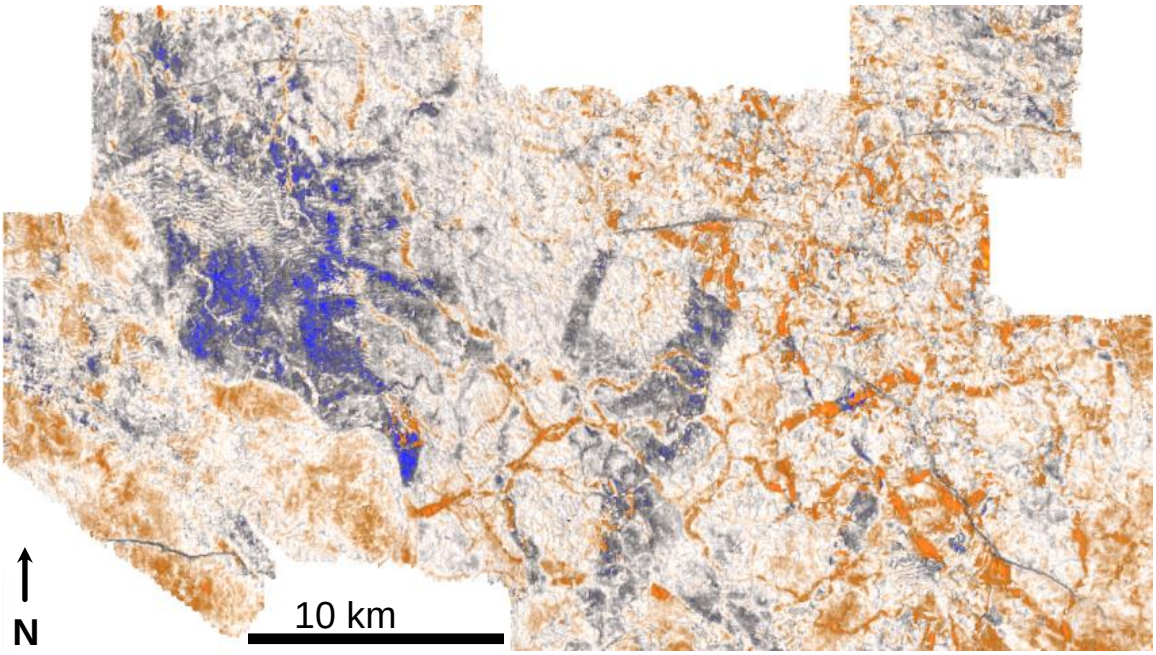

Figure 3.21: Strongly distributive “rat’s nest” network of narrow channels on an amplitude stratal slice. View is from directly overhead.

3.2.9 Spatial and temporal distribution of fluvial styles

Valleys are the most common fluvial style with 10 present throughout the ~ 1300 m thick stratigraphic interval studied. Valleys are seen in alternation with both channel-belts and distributive networks. Four surfaces showing channel-belts are present in the deepest ~ 450 m of the interval (about 1900 m to 1450 m depth) and alternate with valleys at an average vertical spacing of 58 m. Shallower than ~ 1450 m, no channel-belts are found; instead, fluvial styles shift to an alternation of valleys and distributive channel networks with an average vertical spacing of 54 m.

This 1300 m stratigraphic interval spans an approximately five million year period of time from the late Miocene to Pliocene. The youngest channel-belt surface is approximately 6.3 Myr in age and the oldest distributive channel network is approximately 4.9 Myr in age.

Figure 3.22 shows an approximately 20 km strike section through the seismic volume with stratal slices defining the positions of the 21 stratigraphic elements. This figure illustrates the repetitive nature of the stratigraphy as well as the change in fluvial style from an alternation between valleys and channel-belts during the late Miocene to an alternation between valleys and distributive networks during the Pliocene.

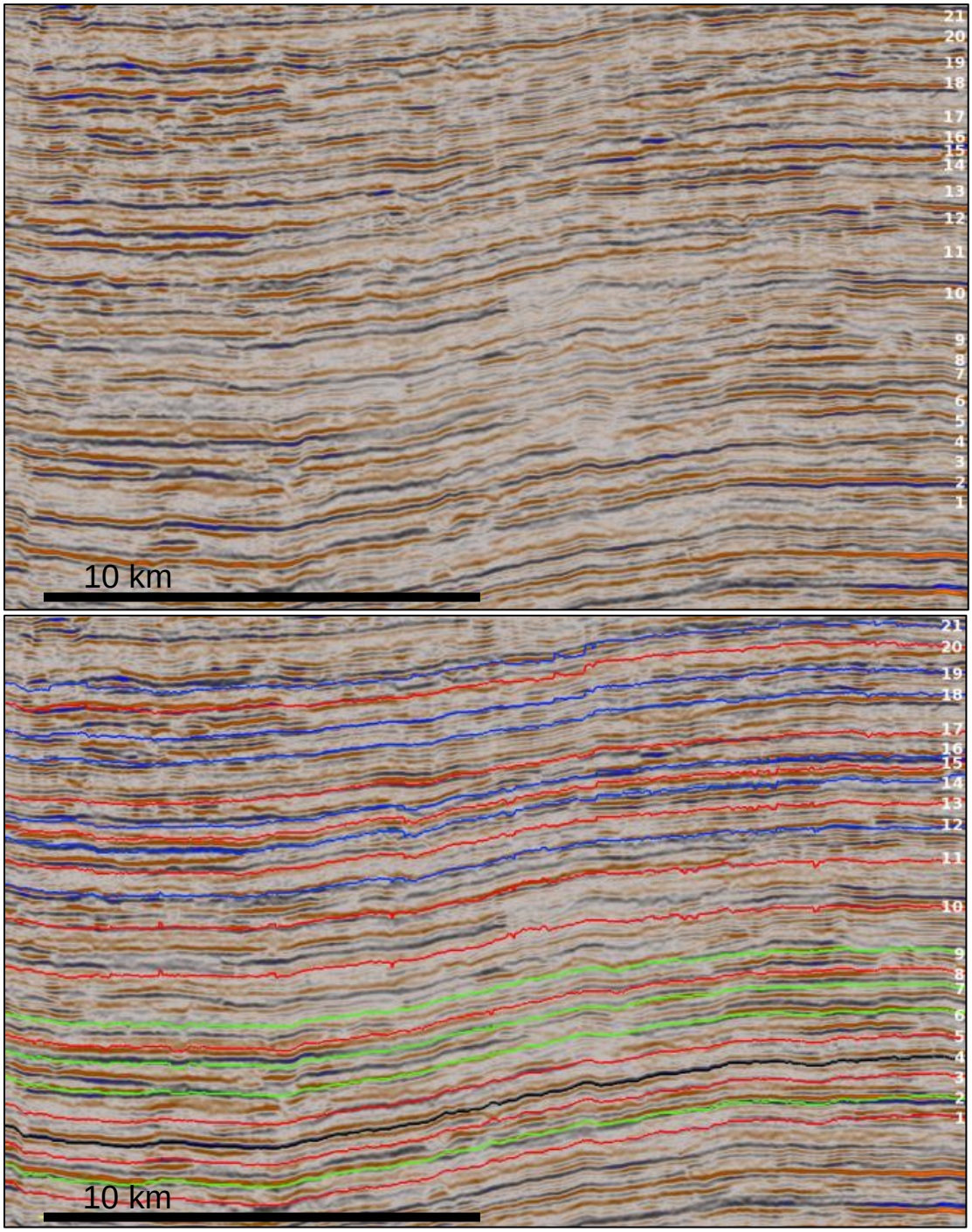

Figure 3.22: A representative east-west oriented strike section through the amplitude volume. The upper image is a cross section without stratal slices overlain and the lower image is the same cross section with outlines of stratal slices shown. The color-coding for the stratal slices is as follows: red indicates valley, green indicates channel-belt, blue indicates distributive channel network, and black indicates a hiatus. Slices are numbered from 1 to 21 with 1 being the oldest and deepest. Cross section location is shown in Figure 3.23 (blue line on each image).

The following set of images (Fig. 3.23) shows the map-view stratigraphy corresponding to each of the 21 stratal slices shown in cross section in Figure 3.22. Image numbers correspond to stratal slice numbers. All images are from directly overhead and are only displayed using the amplitude volume. Scale is approximately 45 km east-west and 25 km north-south (1,125 km^2) for each surface shown. This set of images provides documentation of the evolution of Mississippi River Delta surface morphology over an approximately 5 Myr period from the late Miocene to Pliocene. Image 1 is the oldest at ~ 1900 m depth and image 21 is the youngest at ~ 670 m depth (ages of 8.3 Myr and 2.9 Myr, respectively). The start of the Pliocene is slightly deeper (~ 10 m) than image 11. The type examples discussed in the section above (Fluvial styles by surface) come from slices 13, 7, and 14 (valley, channel-belt, and distributive channel network surfaces, respectively). Slice number 4 shows a rare example of a relatively unchannelized negative amplitude “hiatal” surface.

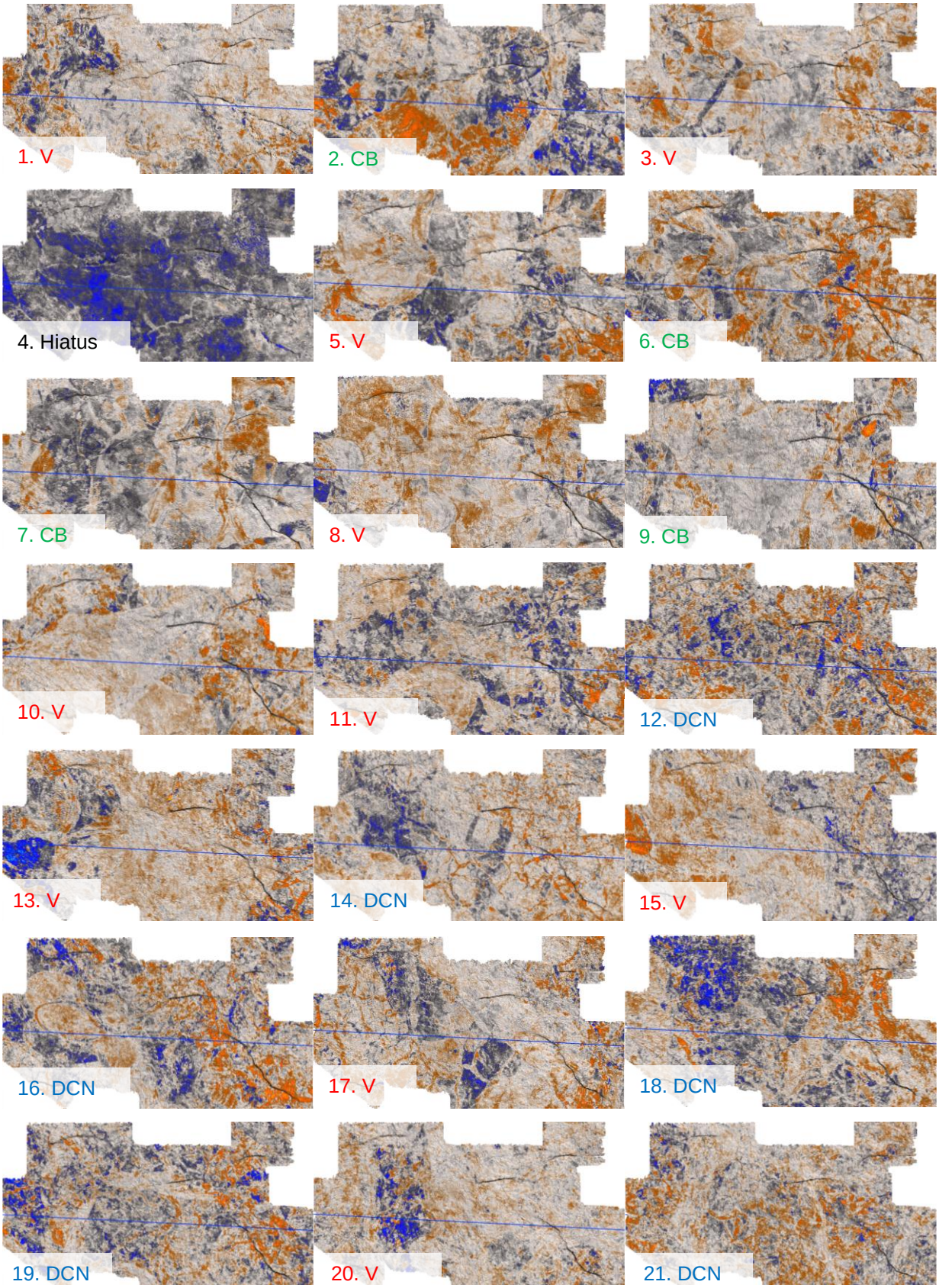

Figure 3.23: 21 Depositional events. V = Valley, CB = Channel-belt, DCN = Distributive channel network system.

The average spacing between each surface can be used to define a fundamental "seismic-stratigraphic interval" for this dataset. For the measured ~ 1300 m section, this length scale is 62 m, (representing an average time period of 270,000 years). The range in spacing between adjacent surfaces is 25 m to 125 m (or 110,000 years to 530,000 years). Figure 3.24 summarizes this information visually and compares interval thickness between the 21 stratal slices to the thickness of 43 channelized bodies also measured in the study volume.

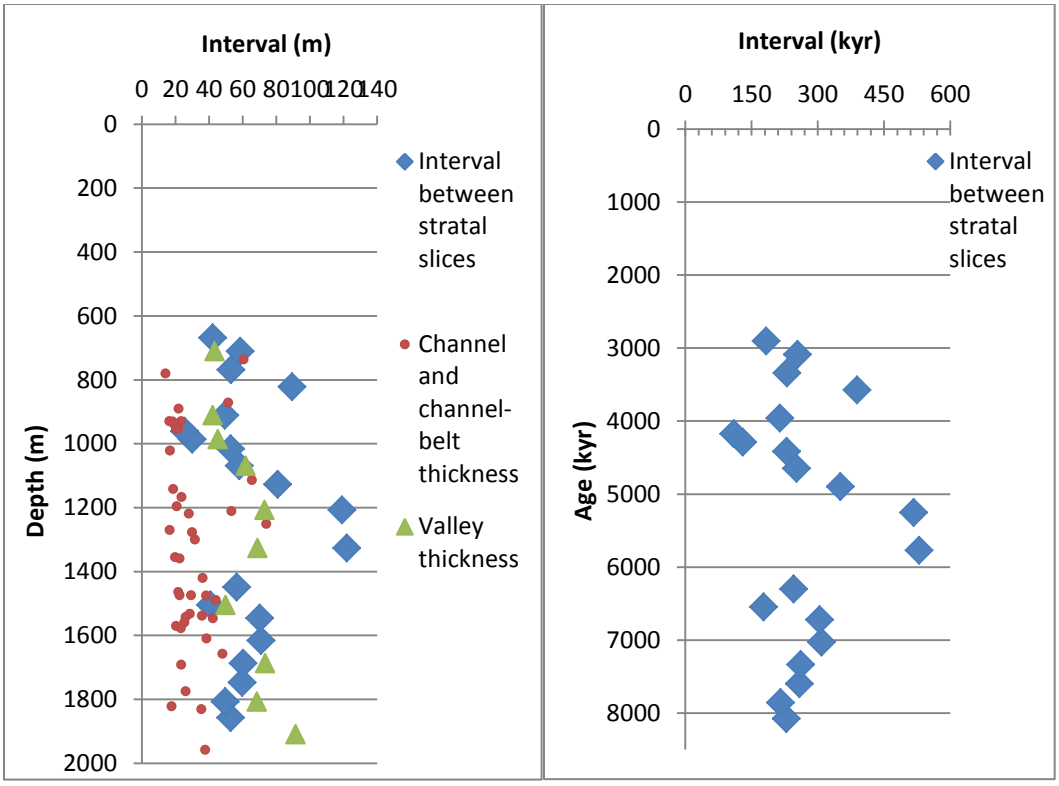

Figure 3.24: (Left) Seismic-stratigraphic interval thickness as a function of burial depth. Each interval represents the average distance between the adjacent significant stratal surfaces. The thicknesses for 43 measured channelized bodies within the study volume are also plotted here. (Right) Estimated durations for the seismic-stratigraphic intervals shown to the left.

Two clusters are apparent in Figure 3.24; a late Miocene cluster and a Pliocene cluster, each consisting of 9 significant surfaces and 8 intervening intervals. The average seismic-stratigraphic interval for each cluster is close to the seismic wavelength at that burial depth, within ~ 3 meters.

Figure 3.25 shows the seismic amplitude spectrum for the same survey interval that contains the lower cluster. Frequency rollover occurs at ~ 45 Hz and P-wave velocity for the midpoint of this interval is 2,545 m/s resulting in a wavelength of about 56.5 m. The seismic-stratigraphic interval for this cluster is 58 m. Figure 3.26 shows the seismic amplitude spectrum for the same survey interval that contains the upper cluster. Frequency rollover occurs at ~ 50 Hz and P-wave velocity for the midpoint of this interval is 2,162 m/s resulting in a wavelength of about 43 m. The seismic-stratigraphic interval scale for this is 46 m.

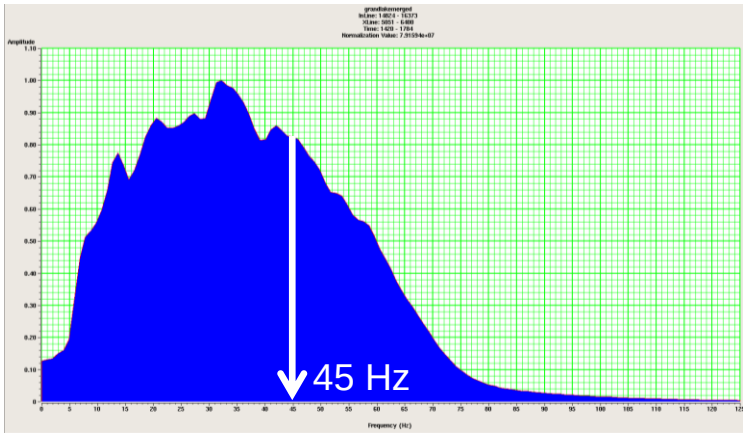

Figure 3.25: Amplitude spectrum from 1420 ms to 1784 ms. Frequency rollover is at ~ 45 Hz.

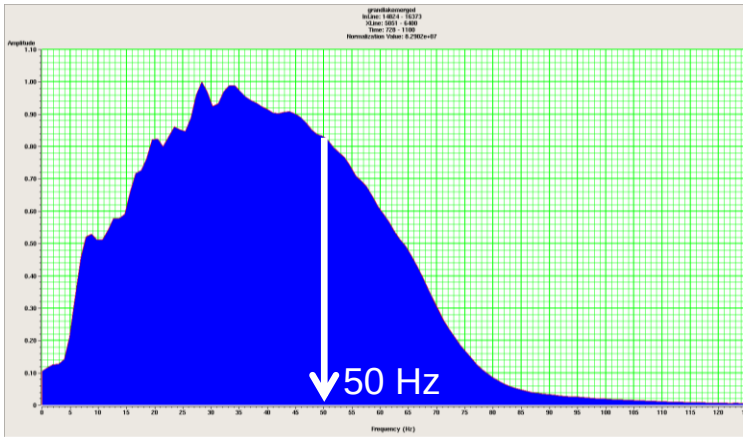

Figure 3.26: Amplitude spectrum from 728 ms to 1100 ms. Frequency rollover is at ~ 50 Hz.

3.3 Discussion

3.3.1 Interpretation of styles of stratigraphy

Changes in fluvial stratigraphy can be caused by both allogenic and autogenic processes. If change is allogenic, then the forcing mechanism may be due to changes in the rate of sea-level rise or fall, changes in the rate of subsidence or uplift, or variations in sediment supply. If autogenic, then changes in sedimentation are due to the non-equilibrium response of sediment transport processes under statistically steady external forcing conditions (Muto et al., 2007). While some of the changes in fluvial style in this dataset may be due to autogenic processes, because of the significant time period (4th order or several hundred thousand years) represented by each seismic-stratigraphic interval and the repetitive nature of the stratigraphy over the more than five million year period studied, the major changes in fluvial style are interpreted mainly as a response to changes in external forcing. Due to the relatively basinward survey location and the quiescent passive margin setting, changes in sediment supply and subsidence are unlikely to significantly contribute to allogenic forcing, leaving sea-level variation as the main driver of changes in fluvial style. Additionally, based on paleogeographic maps for the Miocene and Pliocene Gulf of Mexico basin (Salvador, 1991), the survey is likely located near the highstand shoreline or in-between the highstand and lowstand shorelines where the potential is great for sea-level change to exert a strong influence on surface morphology (the terms highstand and lowstand should most properly be used to refer only to the geometrical arrangement of stacking patterns [Neal and Abreu, 2009]; however, their meaning here refers to position along the relative sea-level curve).

Three distinct fluvial styles were identified in this study: 1) incised valleys, 2) channel-belts, and 3) distributive channel networks. Each of these can be related to a position on the relative sea-level curve.

3.3.1.1 Incised valleys

Incised valleys are interpreted as initiating during relative falls in sea-level. A basic model for the evolution of a valley is that incision occurs through fluvial processes during fall in sea-level and filling occurs through estuarine processes during transgression. The amount of fluvial fill vs. estuarine fill is, among other factors, dependent on distance updip from the lowstand shoreline. Closer to the lowstand shoreline, the fill can be expected to consist of primarily estuarine and reworked fluvial deposits. The amount of estuarine fill is expected to decrease and fill becomes more fluvial towards the highstand shoreline (Zaitlin et al., 1994).

In a 2001 paper, Posamentier asserts that the presence of incised tributary valleys is a key criterion for the identification of incised valleys. Valleys in the Breton Sound dataset do not show any clear incised tributary valleys. However, Maynard et al. (2010) provide examples of incised valleys from 3D seismic data that do not show incised tributary valleys. They go on to qualify Posamentier's statement by observing that most examples of valleys in the literature come from laterally limited well log or outcrop data and do not document incised tributary valleys. Instead, Maynard et al. (2010) suggest that incision bounded at the base by a sequence boundary is the primary factor in valley recognition. It is this criterion that is used here.

Incised valleys and associated sequence boundaries can be identified by several indirect lines of evidence (Zaitlin et al., 1994; Maynard et al., 2010): 1) fluvial incision into marine facies (or an overall basinward shift in facies), 2) onlap onto the valley walls, 3) the large extent to which an incision can be mapped, and 4) the presence of more than one channel fill confined within a thick (relative to other channels) valley. Examples for each criterion are provided here:

1) Fluvial incision into shallow marine facies is difficult to prove without core data; however, many of the interpreted valleys overly regionally extensive negative reflections that, in well log, correspond with ~ 5 m to 20 m high gamma ray value fills (see Figure 3.27 below or Figure 3.12 for examples) which could be muddy shallow marine deposits. Additionally, an overall basinward shift in facies can be seen in some of the valley surfaces where they cut into distributive channel networks.

2) Onlap onto valley walls is demonstrated in Figure 3.27 where two internal reflections are clearly onlapping onto the east side of the valley. The cross section also shows three external reflections terminating against the east edge of the valley and one external reflection

terminating against the west edge of the valley as would be expected from incision into underlying strata.

3) An example of the large aerial extent of valleys is shown in Figure 3.27 (below). Here, a well-defined valley mappable for tens of kilometers is shown covering a significant portion of the ~ 1370 km^2 survey area.

4) Multi-story valley fill is shown in Figure 3.27 (below). Valley fill is generally blocky and consists of several stacked units, each with sharp bases and caps (as seen in gamma ray curves).

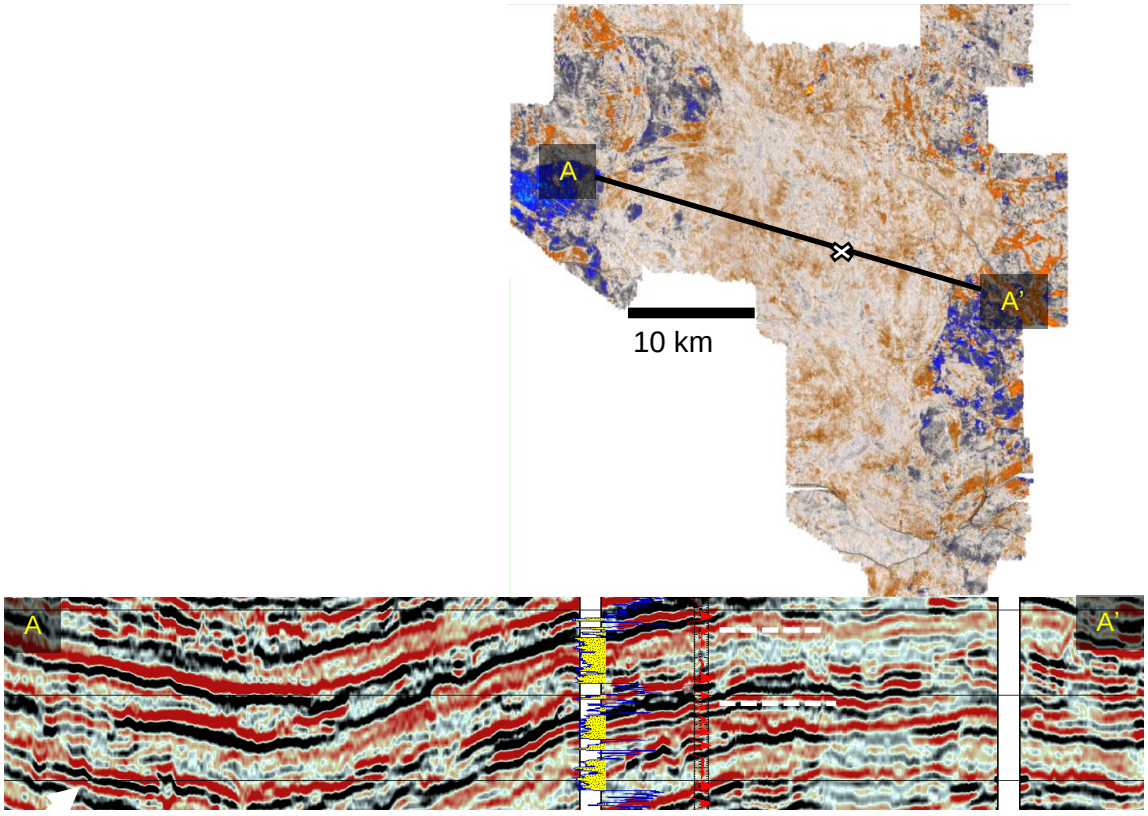

Figure 3.27: Map view and cross section of a valley (previously discussed in data analysis) showing all 4 criteria for valley recognition. White arrows point to edges of valley. Dotted white lines connect well intersection to curve projection.

3.3.1.2 Channel-belts

Though the relationship between channel-belts and sea-level is not as clear as it is for valleys, channel-belts likely represent a form of lowstand deposition. Evidence for this comes from the observation that 100% of interpreted channel-belts extend roughly basinward across the entire survey. Channel-belt fill tends to be single story and is interpreted as a result of lateral channel migration which often leads to a “scoop-shaped” planform character as preserved in the seismic data. An analogue for this planform geometry can be seen in the modern Mississippi River a few hundred kilometers upstream of the survey area (Fig. 3.28, right image).

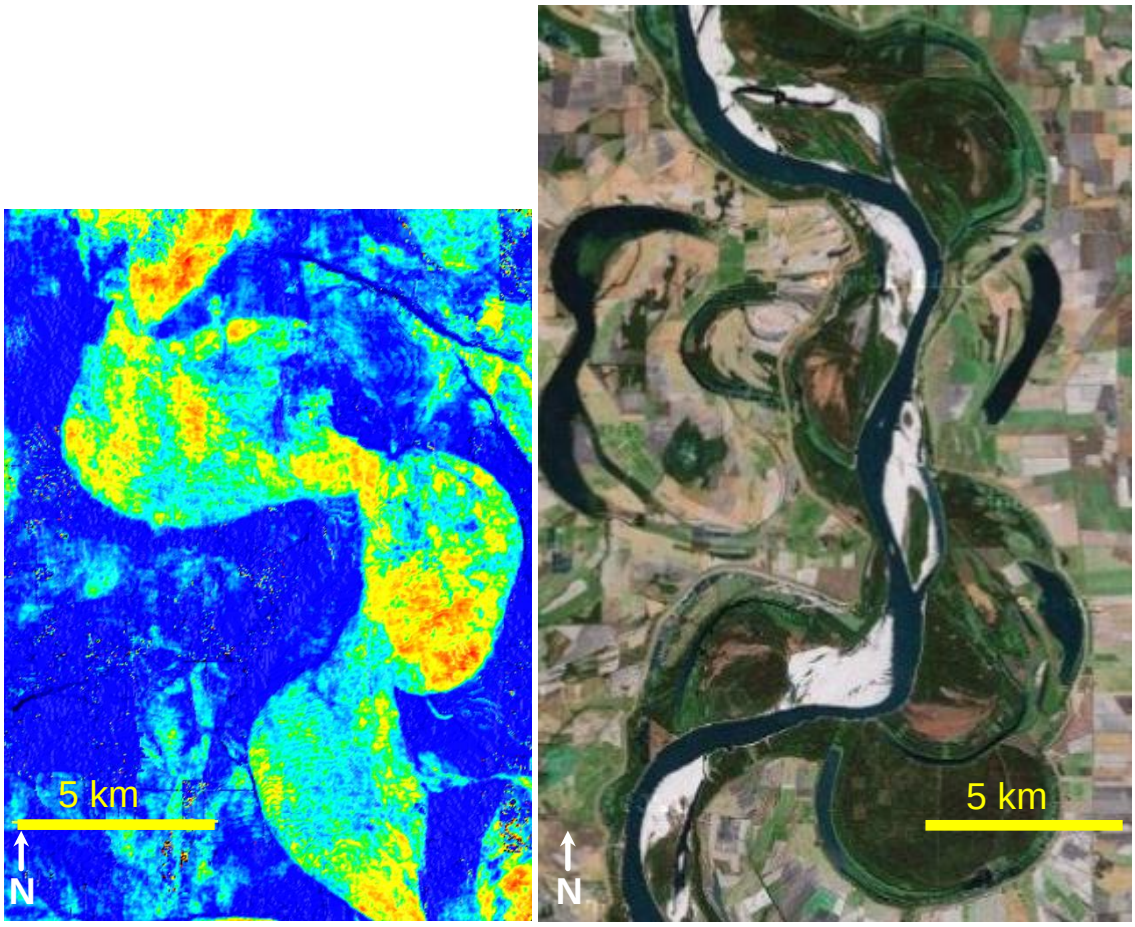

Figure 3.28:. Channel-belt from seismic (left image, sweetness shown) and a modern Mississippi River analogue for formation of a channel-belt (right image). Scale is the same in both images.

3.3.1.3 Distributive channel networks

Distributive channel networks are interpreted as highstand deposits. Planform geometry appears as a “rat’s nest” of narrow, highly distributive channels. An analogue for this fluvial style can be found in the surface morphology of areas of the modern Mississippi River Delta (Fig. 3.29). Distributive channel networks tend to have the highest density of individual channels (with up to several dozen) preserved on a single surface. This is interpreted as either a result of high avulsion frequencies in a limited number of channels or as a result of a high number of concurrently active channels or perhaps a mix of both factors. Some of the Pliocene valley surfaces appear to be incised into distributive channel networks (e.g., surfaces 15 and 17) which is consistent with the sea-level associations for each (i.e. a basinward shift in facies from distributive channel networks to valleys).

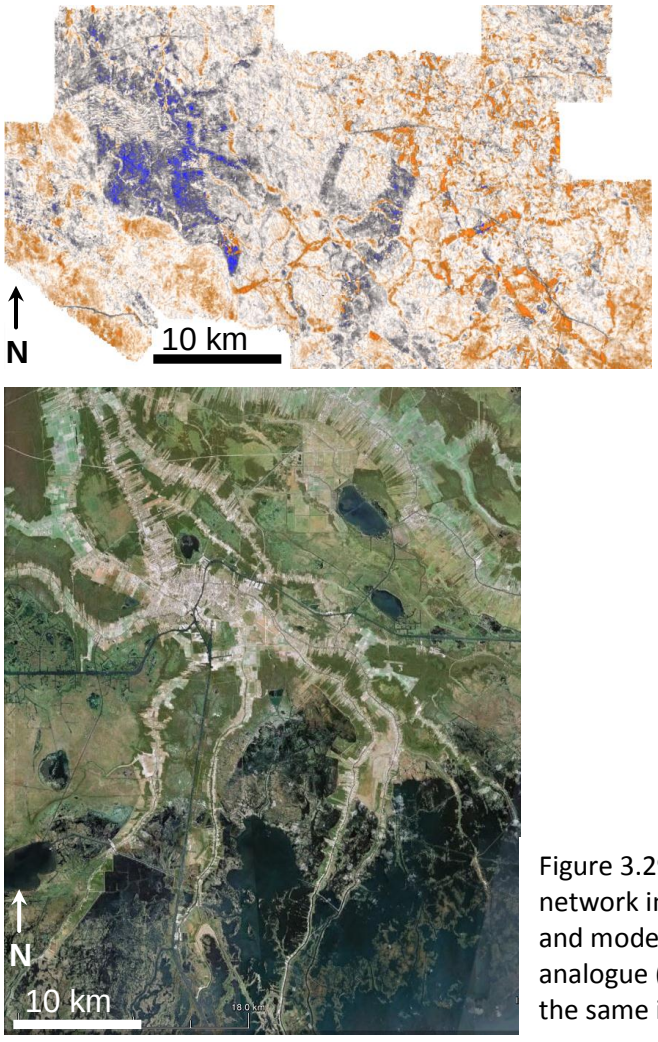

Figure 3.29: Distributive channel network in seismic (upper image) and modern Mississippi River Delta analogue (lower image). Scale is the same in both images.

3.3.2 Sea-level curve construction and comparison

While constraining the absolute magnitude of sea-level fall or rise is not attempted from this dataset (though it is likely related to the depth of valley incision), a 4th order relative sea-level curve was estimated for the late Miocene to Pliocene Mississippi River Delta based on the sequence stratigraphic interpretation of each fluvial style (Fig. 3.30).

Valleys represent relative lows in sea-level and distributive channel networks represent relative highs in sea-level. Sea-level during channel-belt periods is interpreted as being higher than during valley periods but lower than during distributive channel network periods. The hiatal point (surface 4 in Figure 3.23) is interpreted as shallow marine deposition representing a relative high in sea-level.

The Abreu and Anderson (1998) eustatic sea-level curve (constructed from the oxygen isotope record) is shown against the Breton Sound relative sea-level curve in Figure 3.30. As no absolute magnitude of change was established from Breton Sound, for comparison purposes the relative changes were adjusted to appear similar in magnitude to the absolute sea-level (valleys were placed at - 30 m, channel-belts at + 15 m, the hiatus at + 25 m, and distributive channel networks at + 60 m).

The frequency of Breton Sound events (averaging 270 kyr) is higher than the frequency of events shown in the Abreu and Anderson (absolute change) curve for the late Miocene to Pliocene period (roughly 4^{th} order for Breton Sound curve vs. 3^{rd} order for Abreu and Anderson curve). The rise in sea-level shown in the absolute curve near the start of the Pliocene corresponds with the change away from Breton Sound channel-belt and valley repetition in the late Miocene to Breton Sound distributive channel network and valley repetition in the Pliocene. This also corresponds with the southwest shift in depocenter location during the Pliocene. The Pliocene portion of the Breton Sound curve correlates with the absolute curve to a greater extent than does the late Miocene portion of the Breton Sound curve. The shapes of the two curves match well from about 4,200 kyr to 3,000 kyr. The nearly 1 Myr period of high sea-level shown in the absolute curve near the start of the Pliocene contains three distributive channel networks and two valleys as interpreted from the Breton Sound dataset. While this is an overall high in the absolute curve, it does show some variation with a fall and a rise in sea-level at about

4,300 kyr. Though some events in the late Miocene match between the two curves (e.g., the high at 7,600 kyr and the high at 4,200 kyr), the overall match is poor for this period.

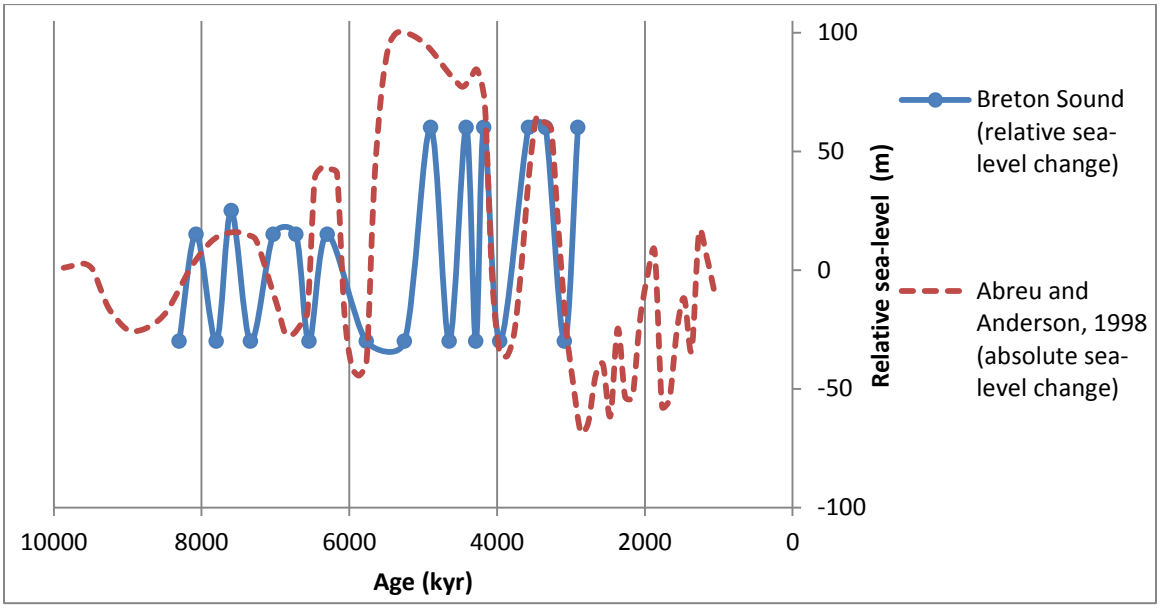

Figure 3.30: The Breton Sound relative sea-level curve compared to the Abreu and Anderson (1998) sea-level curve. The Breton Sound curve is only intended to show relative change, not its absolute magnitude.

3.3.3 A seismic-stratigraphic filter of sea-level change

Figure 3.31 shows the Miller et al. (2005) sea-level curve constructed using oxygen isotope data from the New Jersey shelf plotted against the Breton Sound relative sea-level curve. The frequency of sea-level change in the Miller et al. curve is over an order of magnitude higher than the frequency defined by the Breton Sound curve, as well as the Abreu and Anderson curve. This difference in frequency content between the stratigraphically derived relative sea-level curve and the high resolution oxygen isotope proxy curve can be attributed to both the attenuation of the high frequency signal within the stratigraphic record and the further attenuation of that signal due to the band-limited nature of seismic data.

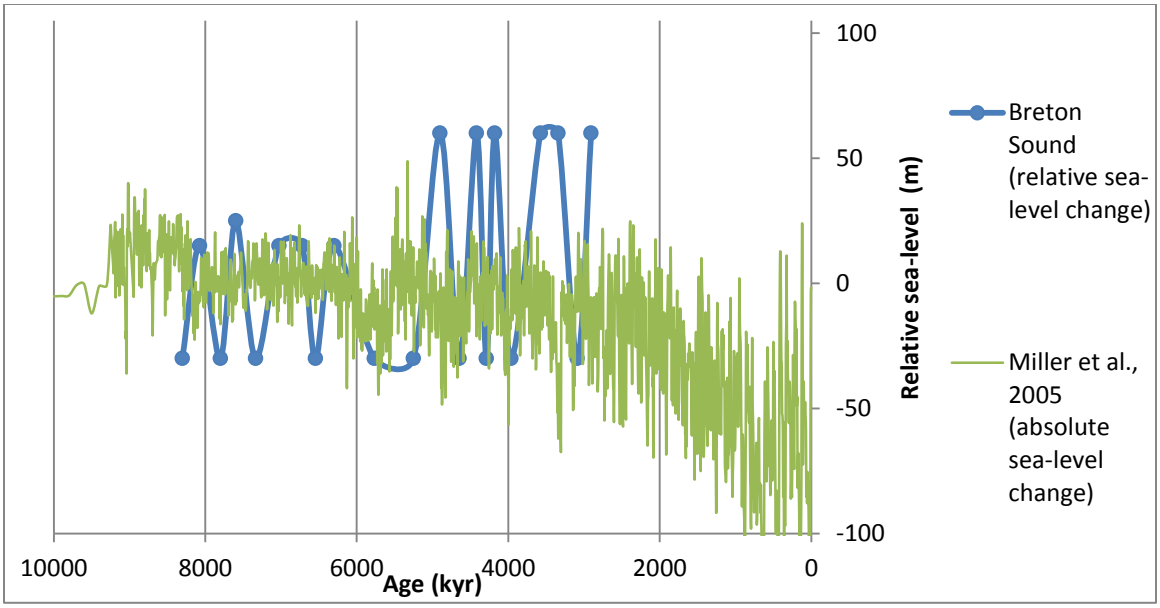

Figure 3.31: The arbitrarily scaled Breton Sound curve compared to the Miller et al. (2005) sea-level curve from oxygen isotope data.

The potential for high frequency sea-level change to be recorded in the seismic-stratigraphic record is likely related to a wide number of factors. If the change is rapid enough, then fluvial systems may not have time to respond. If the magnitude of change is small, then the fluvial systems may not measurably respond to the change, especially during lowstand times where the survey may be significantly updip of the shoreline. If stratigraphy is affected, many of the high frequency sea-level change events may be removed by subsequent erosive events, resulting in an overall low preservation potential within the stratigraphic record.

Alternatively, the events may be recorded in the stratigraphy but fall below seismic resolution, resulting in multiple sequences being contained within a single reflection. Seismic resolution is limited to ~ ¼ of a seismic wavelength (Brown, 2004). Seismic wavelength increases with depth from about 45 m in the shallow Pliocene portion of the dataset to about 60 m in the late Miocene portion, leading to resolution limits of about 11 m to 16 m. These seismic resolution limits act as a low-pass filter, allowing low frequency changes in sea-level to pass through but removing any frequency higher the time period set by the seismic resolution limits (~ 50 to 70 kyr).

The average seismic-stratigraphic interval for this dataset (derived from thicknesses between the 21 fluvial events) is 62 m, representing a time period of about 270 kyr. As these numbers are about 5 times the limits presented by seismic resolution, the seismic-stratigraphic filter appears to be controlled by fluvial processes. Average thickness from the 43 fully mapped fluvial systems and the 10 partially mapped valley systems is 36.5 m, about twice the seismic resolution and 60% of the seismic-stratigraphic interval. However, thicknesses in this dataset vary by almost an order of magnitude depending on fluvial style (from about 11 m to 90 m). If only the average thickness of the 10 valleys (which make up nearly 50% of the events on the Breton Sound relative sea-level curve) is considered, then the average seismic-stratigraphic interval of 62 m is close to the average valley thickness of 63 m. As the seismic-stratigraphic interval generally measures a repetitive alternation between valleys and channel-belts or distributive channel networks and only once measures the interval between two valleys, the close agreement between the average seismic stratigraphic interval and the average valley thickness is remarkable and appears to represent fundamental filtering of stratigraphy in this dataset.

In this study, the 21 depositional events are considered individually. However, they may also be interpreted as coupled events with each valley (representing a low in sea-level) paired with either a distributive channel network or a channel-belt (deposited during higher sea-level positions). As such, the interval represented by each cycle would be about 120 m or 540 kyr. The relatively low number of cycles (~ 10) for the interval studied is likely a result of the limited seismic resolution. If the higher resolution well log data were used instead, then the number of cycles would presumably increase. As this project was primarily a seismic based study of stratigraphy, the well logs were mainly used to determine lithology and to constrain inversions. Detailed correlation and study of cycles within the well logs was considered beyond the scope of the project but may be a direction for future work on the dataset.

3.4 Conclusions

1) The average, minimum, and maximum width and depth (thickness) for fluvial stratigraphy in this dataset follow power-law scaling relationships. The majority (90%) of the non-valley systems have aspect ratios below 100.

2) The fill within these systems is generally sandy with porosities of around 35%. There is, however, heterogeneity within each system. This variability in fill appears to be highest in valley systems which are composed of stacked units of sand that are generally blocky but may be coarsening or fining upwards.

3) Breton Sound late Micoene to Plicoene fluvial stratigraphy can generally be categorized as one of three types: incised valleys, channel-belts, and distributive channel networks. Based upon the sequence stratigraphic interpretation of each fluvial style, a 4^{th} order relative sea-level curve can be constructed, but in general agrees poorly with other sea-level curves.

4) A seismic-stratigraphic interval that separates major changes in fluvial style is found to scale with the average valley thickness.

Chapter 4: Influence of Faults

4.1 Background

A basic principle in the study of interactions between fluvial systems and spatially varying subsidence is that rivers can be preferentially attracted to areas of high subsidence (Alexander and Leeder, 1987). The potential for variations in subsidence to affect fluvial stratigraphy has been documented in numerous field studies (e.g., DeCelles, 1986; Mack and Seager, 1990; Peakal, 1998; Mack and Leeder, 1999; Peakal et al., 2000). Fluvial sensitivity to subsidence is, however, dependent on the interplay of a number of different factors. In a simulation model of alluvial stratigraphy, Bridge and Leeder (1979) found a strong clustering trend in areas of high tectonic tilting due to a fault-created, transverse floodplain slope. In their model, this only occurred when tilting was maintained for a prolonged period of time. Mackey and Bridge (1995) found that tectonic tilting caused channel-belts to shift away from zones of uplift and towards zones of maximum subsidence. However, in their model, if the aggradation rate is high enough to keep up with subsidence, no fault effect was seen. Kim et al. (2010) experimentally demonstrated the importance of tectonic timescale and avulsion frequency. In their flume experiment, channels were most influenced by variations in subsidence if channel mobility was low relative to subsidence rates.

The majority of studies have focused on the effects of large scale extensional tilting on fluvial systems in half-graben settings. Only a few workers have looked at the extent to which more local scale faulting can influence stratigraphy. Maynard (2006) used relatively high resolution 3D seismic data to document fluvial response to the development of a growth fault related rollover anticline. The data imaged, over a series of time slices, the evolution of a series of narrow (100's of meters wide) channels on the hanging-wall side of a growth fault. The fluvial system underwent an increase in sinuosity and avulsion frequency in response to the increase in slope created by faulting. Taha and Anderson (2008) studied avulsion frequency of the Brazos incised valley. Using core, radiocarbon, aerial photo, and digital elevation model data, they examined the effect of tilting due to a growth fault on avulsion history of the valley. Their results showed that a late Pleistocene nodal avulsion point was located at the site of active movement on the growth fault.

This study uses an industry 3D seismic volume to examine the effect of local growth faults on fluvial stratigraphy in the late Miocene to Pliocene Mississippi River Delta. The seismic volume contains several dozen examples of paleo-channels, channel-belts, and valleys that cross growth faults. Many of these growth faults are active for the entire Miocene to Pliocene interval and so fluvial systems crossing these faults may have been subject to significant variations in subsidence.

Previous work (Mohrig et al., 2010) and part of this study examined the relationship between relatively small channels (with 75% of measured widths falling below 400 m and 90% falling below 1 km) and growth faults. The results show that geometry (width and depth) and planform for the majority of the mapped small channels that intersect growth faults are not affected. Width and depth for 100% of the 54 mapped paleo-channels were not affected by faults. In only two cases was channel planform clearly redirected by faults. Figure 4.1 shows a rare example where the planform of an approximately 250 m wide channel is aligned along the downthrown side of a fault.

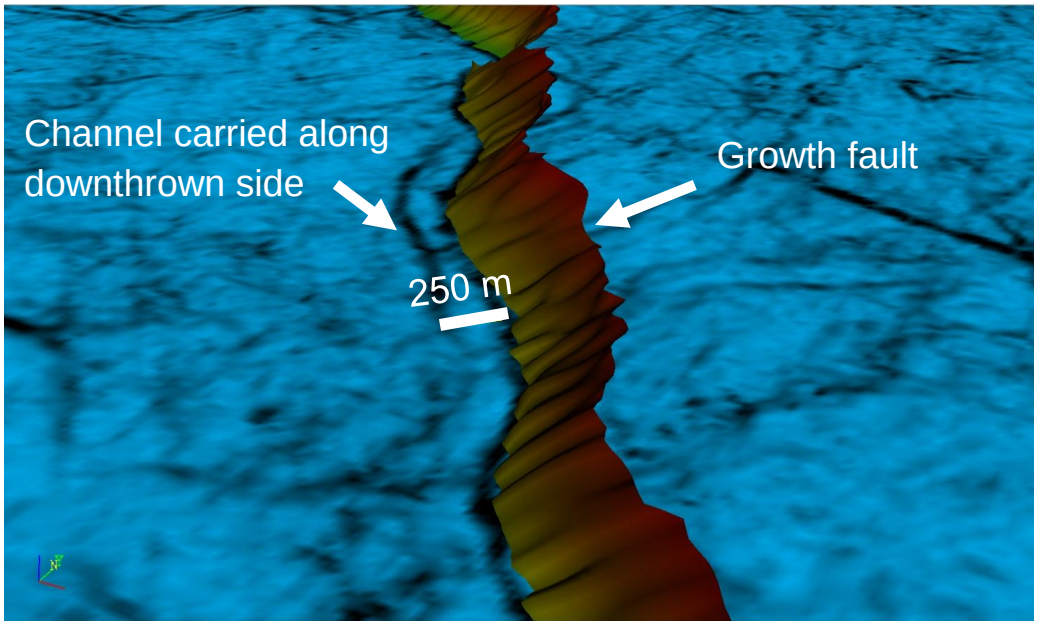

Figure 4.1: Perspective view of a narrow channel aligned with the hanging wall of a growth fault for a distance exceeding 1 km. The growth fault is dipping to the left (red indicates shallowest level of the mapped fault). The channel is imaged here on a similarity stratal slice.

The relative cross stream versus downstream gradient has been proposed (Peakal et al., 2000; Kim et al., 2010) as a primary control on whether fluvial stratigraphy is influenced by subsidence. If the cross stream slope created by growth faulting is much lower than the downstream slope, then growth faults would not be expected to influence channels. Downstream slopes in this study are low ($< 10^{-4}$) due to the passive margin setting. Field data (Gagliano, 2003) show that short term fault displacement rates can be on the order of 10^2 mm/yr. As a result, local cross-stream gradients are likely to be greater than the downstream slope, yet small channels appear relatively insensitive to faulting. As demonstrated by Kim et al. (2010), channel mobility is also an important factor in fluvial sensitivity to growth fault created subsidence. If the time scale for channel avulsion is short relative to the frequency of faulting events, then an individual channel may avulse before feeling the effect of a fault. The relative timescales of faulting and channel avulsion appears to be an important control for small channels in this dataset.

In addition to the many small channels, the seismic volume also images ten channel-belt systems (with widths ranging from 1.5 to 4 km) that cross growth faults. The relationship between these larger systems and faults has not been previously addressed. While exact avulsion frequencies cannot be constrained from this dataset, channel-belts are relatively long lived features with avulsion frequencies that are likely lower than small channels. It follows that for channel-belt systems, the ratio of the time scale of avulsion to faulting is higher than for small channels. This allows the relative importance of time scales on the potential for fault influence to be examined.

4.2 Data analysis

Descriptions of one small channel and seven large fluvial systems are presented here. All of these systems intersect and appear to be affected by one or more growth faults.

4.2.1 Example A

Figure 4.2 shows a rare example where positioning of a small channel appears to be influenced by a fault. Example A is a narrow (average channel width is 120 m) Pliocene age channel located in the eastern portion of the survey. The channel can be followed southwest across the eastern part of a basinward dipping growth fault. Upstream of the fault, the channel has a low sinuosity (1.09) and its course trends to the southwest. Less than 50 m downstream of the fault, the channel abruptly turns and flows northwest along the downthrown side of the fault for over 500 m. It then turns sharply back to the southwest and continues on its course for about 500 m until it can no longer be imaged in the seismic volume. The channel width near the fault averages 100 m and there is no clear change in width or thickness across the fault. Upstream of the fault, the channel position is approximately 780 m beneath the surface; downstream of the fault, the channel is approximately 822 m beneath the surface. The fault offset ratio with this 42 m channel displacement is about 5%.

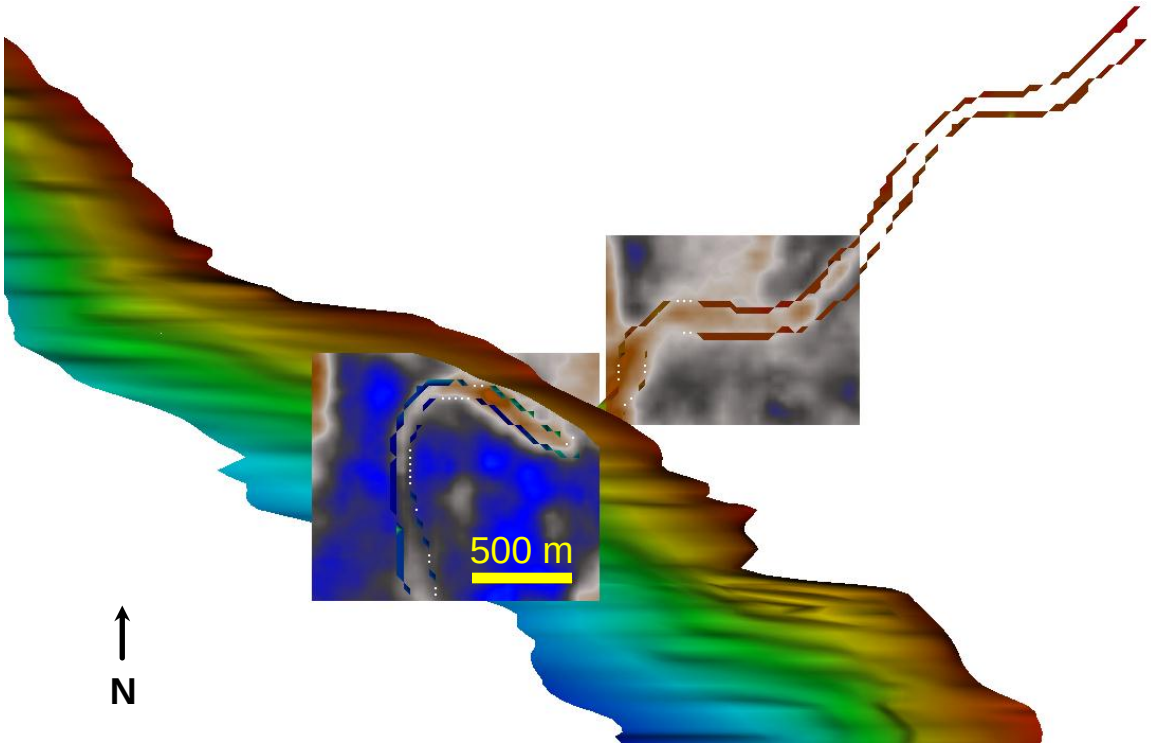

Figure 4.2: A narrow Pliocene channel aligned with the downthrown side of a mapped fault. The two probes (rectangular boxes) show the channel planform as it appears in the amplitude volume. View is from directly overhead; hotter colors define shallower depths for the fault plane which is dipping to the left-hand side of the figure.

Overlaying the channel on the time-structure map (Fig. 4.3) for the connected stratal slice shows that the channel is located over the subsidence maximum on the downthrown side of the fault. The channel turns to the south before reaching a local topographic high (point 1 on Fig. 4.3) and then flows through an area between high points 2 and 3.

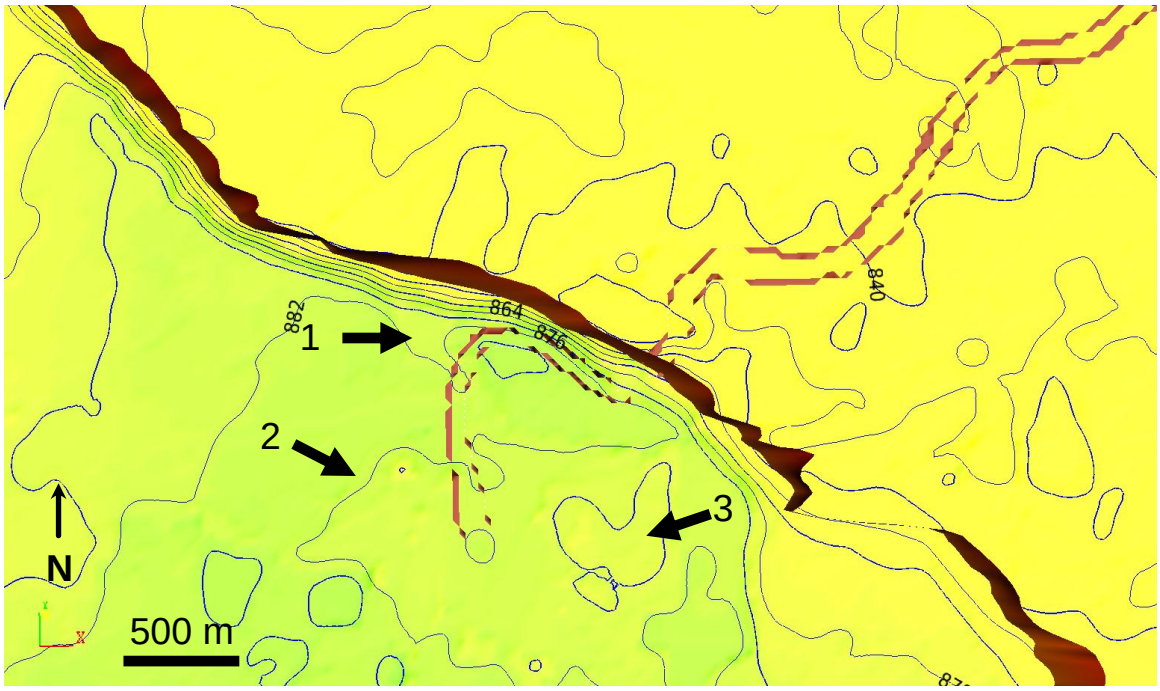

Figure 4.3: Time-structure map of a surface that images the channel. Numbered points indicate topographically high areas on the hangingwall of the mapped fault (shown here in brown). Contour interval is 6 ms; yellows are high. View is from directly overhead.

4.2.2 Example B

This southwest trending Miocene age channel-belt (Fig. 4.4) is located in the eastern portion of the survey and was mapped for over a 19 km distance. The channel-belt is completely cut by one southeast striking growth fault and partially intersects a second growth fault that cuts the east side of the channel-belt about 200 m downstream of the main fault. Only the relationship between the channel-belt and the main fault is considered here. The channel-belt approaches the fault zone at an angle of 15 degrees from normal to strike of the fault and exits the zone oriented about 2.5 degrees from normal to the strike of the fault. The channel-belt is low sinuosity (1.08) and has an average width of 2.7 km and an average thickness of 35 m. Width is 2.2 km near the upstream side of the fault and increases to 2.8 km downstream of the fault. The channel-belt crosses the fault at a depth of approximately 1800 m and is displaced 62 m for an offset ratio of 3.4%.

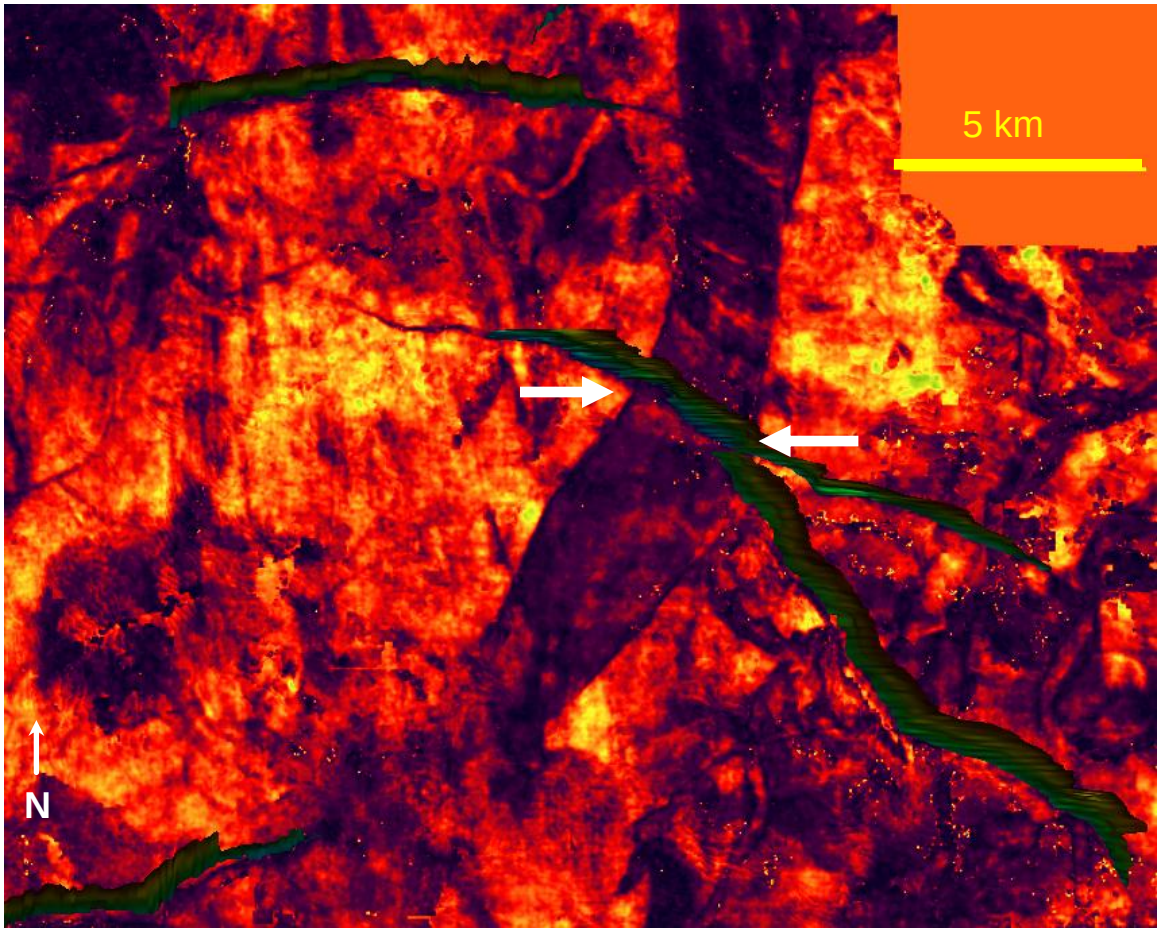

Figure 4.4: Example B, a Miocene channel-belt system. View is from directly overhead with sweetness attribute shown. Hotter colors indicate higher sweetness. Arrows point to the fault with the channel-belt imaged as the dark area in between the two arrows.

4.2.3 Example C

Example C (Fig. 4.5), a late Miocene channel-belt, is located in the central portion of the survey and was mapped for over 21 km distance. The channel-belt has a sinuosity of 1.2 and crosses an east-west trending counter regional (dipping to the north) growth fault near the middle of the mapped portion of the channel-belt. Over a distance of approximately one channel-belt width upstream of the fault, the channel-belt approaches the structure at 40 degrees from normal to the strike of the fault. Downstream of the fault, the channel-belt is oriented approximately 14 degrees from normal to the strike of the fault over the same measurement length. Over the same distances, the channel-belt increases in width across the fault from an average of 550 m upstream to 970 m downstream of the fault. No corresponding

change in thickness is resolved. The channel-belt crosses this fault at approximately 1600 m depth and displacement across the fault is 75 m giving an offset ratio of about 4.7%.

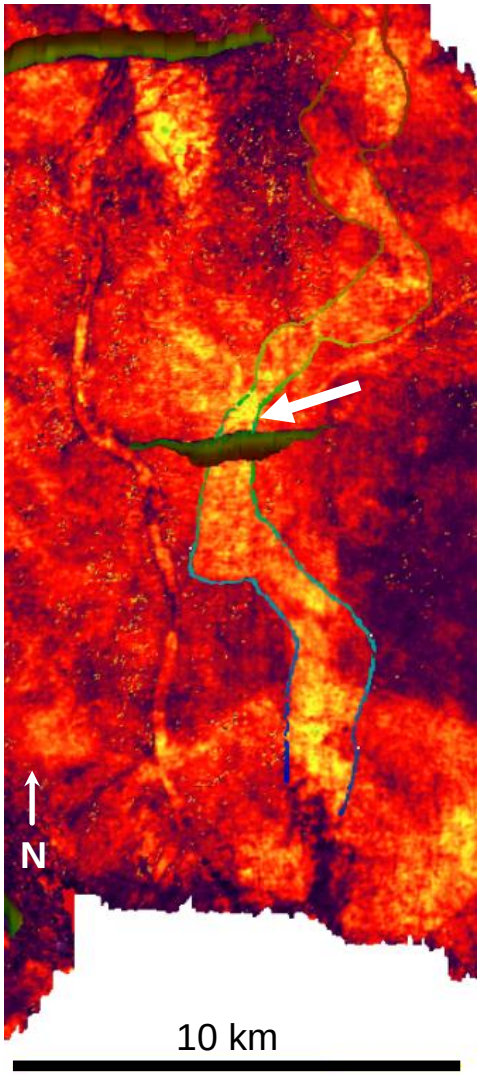

Figure 4.5: Example C, a late Miocene channel-belt system. View is from directly overhead with sweetness attribute shown. Hotter colors indicate higher values for the sweetness attribute.

4.2.4 Example D

This south trending, late Miocene low-sinuosity channel-belt (Fig. 4.6) is located in the central portion of the survey and crosses two growth faults about 15 km apart. The fault to the south has no apparent effect on the channel-belt. This may be because the fault only intersects the western-most portion of the channel-belt. The fault to the north, however, does seem to influence channel-belt positioning across structure. For a distance of approximately one channel-belt width upstream of the fault, the channel-belt approaches at an angle of 12 degrees away from normal to the strike of the fault. Downstream of the fault, for a distance of approximately one channel-belt width, the channel-belt is oriented less than 3 degrees from perpendicular to the strike of the fault. For the same length scales there is a slight narrowing of the channel-belt across the fault. Channel-belt width upstream of the fault averages 1400 m while channel-belt width downstream of the fault averages 1200 m. No apparent change in thickness across the fault is resolved. The channel-belt crosses this fault at approximately 1300 m depth and displacement across the fault is 33 m giving an offset ratio of 2.5%.

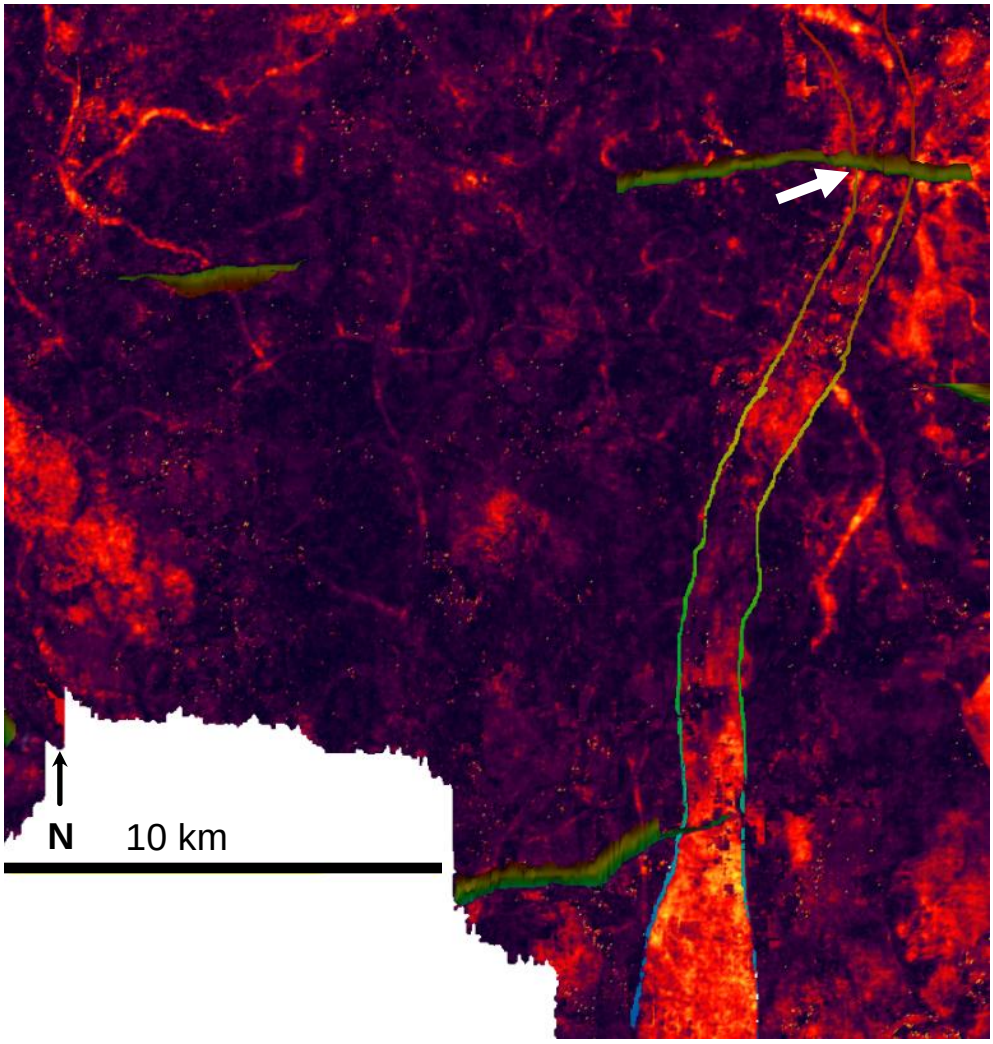

Figure 4.6: Example D, a late Miocene channel-belt system. View is from directly overhead on a map of the sweetness attribute. Hotter colors indicate higher sweetness values.

4.2.5 Example E

Example E is a south trending Mio-Pliocene age channel-belt located in the eastern portion of the dataset that was mapped for over 20 km channel-belt distance. Average width is about 2000 m and average thickness is about 38 m. The channel-belt tends to widen downstream until, near the southern end of the channel-belt, it bifurcates into a narrow western segment and a wider eastern segment (Fig. 4.7). The channel-belt is fully intersected by two faults, one near its northern end at about 1415 m below the surface and one near the center of the channel-belt at about 1530 m depth. Vertical displacement of the belt by the north

fault is 44 m and displacement across the south fault is 64 m leading to offset ratios of about 3 and 4 percent, respectively. Upstream of the bifurcation, the channel-belt is very straight and trends almost directly to the south while the faults strike roughly east-west, with the southern fault having a more southeast-northwest oriented strike. Measurements show some redirection of the channel-belt by the faults. For the northern fault, the channel-belt approaches at 5 degrees and leaves at about 4 degrees from normal to the strike of the fault. For the southern fault, the channel-belt approaches at 38 degrees and leaves at 29 degrees from normal to the strike of the fault. This redirection of the channel-belt by the southern fault occurs even though the channel-belt crosses near the western edge of the fault where its displacements become very low.

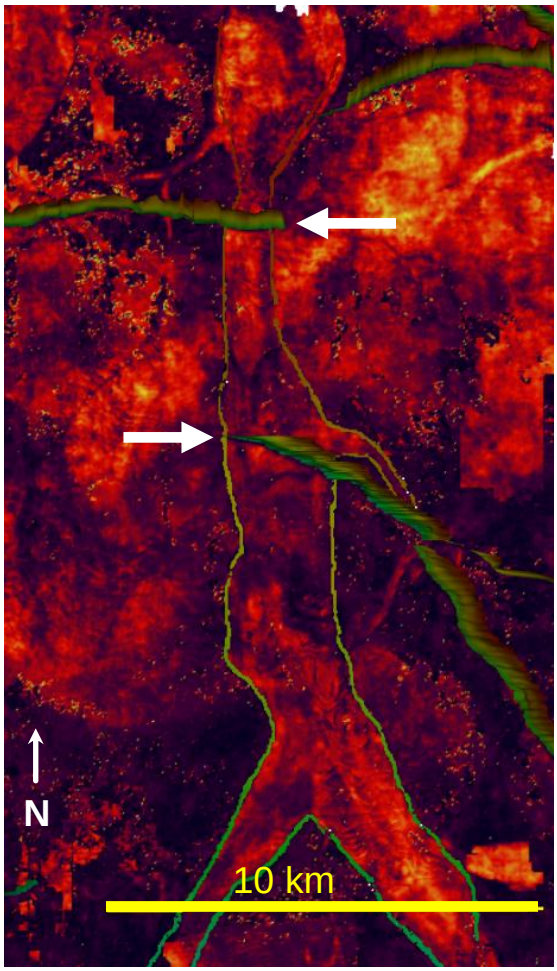

Figure 4.7: Example E, a Mio-Pliocene channel-belt. View is from directly overhead with sweetness attribute shown. Hotter colors indicate higher sweetness.

4.2.6 Example F

This south trending late Miocene to earliest Pliocene age channel-belt is located in the west portion of the dataset and was mapped over a 20 km distance. The channel-belt has low sinuosity (1.16) and average width of 2800 m with an average thickness of about 19 m. At about 1330 m depth, the channel-belt is intersected by one east-west trending fault near the northern end of the channel-belt. For a distance of about one channel-belt width upstream of the fault, the channel-belt approaches the fault at an angle of about 21 degrees normal to the strike of the fault. For the same distance downstream of the fault, the channel-belt is oriented less than 6 degrees from normal to the strike of the fault. There is no systematic change in channel-belt width or thickness across the fault. Total displacement across the fault is 52 m leading to an offset ratio of about 4%.

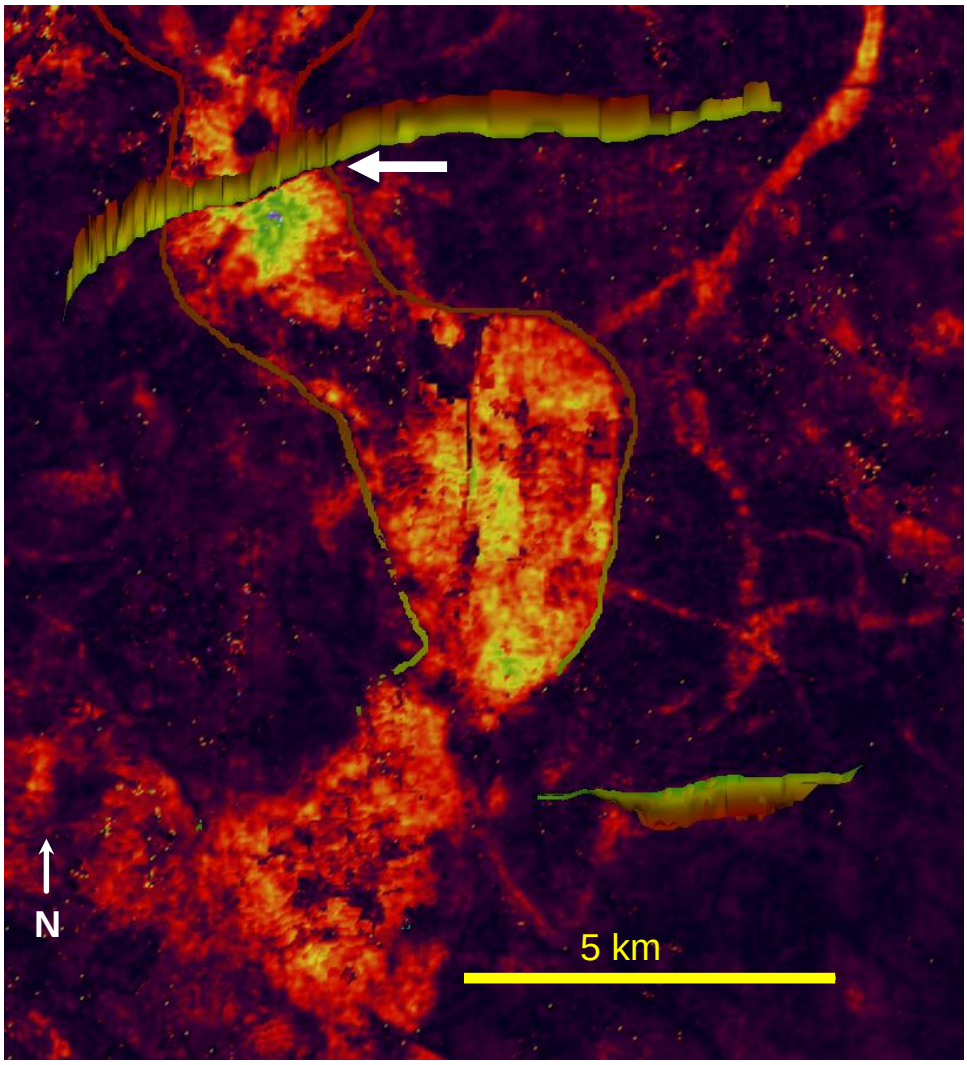

Figure 4.8: Example F, a Mio-Pliocene channel-belt. View is from directly overhead with sweetness attribute shown. Hotter colors indicate higher sweetness.

4.2.7 Example G

This south-southwest trending Pliocene channel-belt is located in the eastern portion of the survey and was mapped for over a 23 km distance. The channel-belt crosses two southeast-northwest trending faults near the center of the mapped channel-belt. Within most of the channel-belt, the two faults are separated by only a few hundred meters and so are measured as a single faulting event. Upstream of the fault, the channel-belt approaches at an angle 18 degrees normal to the strike of the fault. Downstream of the fault, the channel-belt is oriented less than 1 degree normal to the strike of the fault. The average width is 3400 m and average

thickness is 32 m; there is no systematic change in channel-belt geometry across the fault. The channel-belt intersects the faults at about 1400 m depth and is displaced a total of 96 m for an offset ratio of about 7 percent. This high offset ratio is a result of the channel-belt being displaced by both faults.

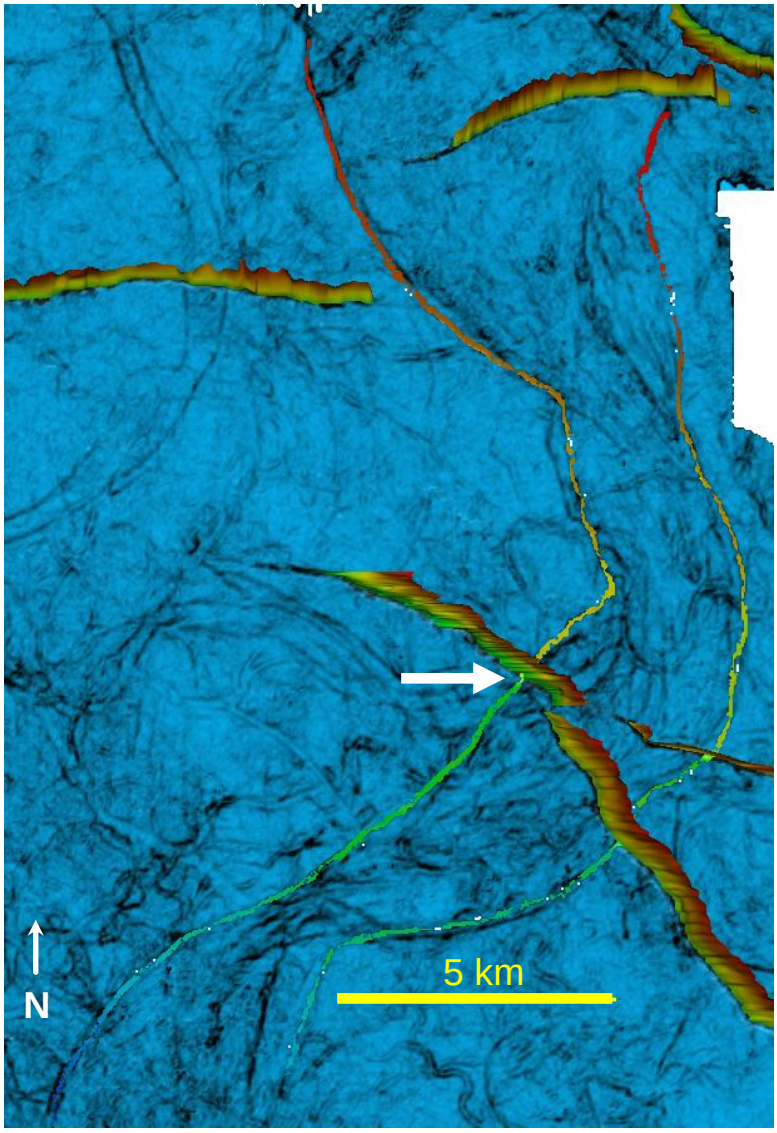

Figure 4.9: Example G, a Pliocene channel-belt. View is from directly overhead with similarity attribute shown. Darker colors indicate lower similarity.

4.2.8 Example H

Example H is a Pliocene age south trending channel-belt located in the central portion of the dataset that has very low sinuosity at 1.03 over 10 km channel-belt distance. The channel-belt crosses near the center of an east-west trending growth fault and positioning appears to be influenced by the fault. For one channel-belt width upstream of the fault, the channel-belt approaches at an angle 24 degrees normal to the strike of the fault. For the same distance downstream of the fault, the channel-belt is oriented less than 1 degree from normal to the strike of the fault. Width increases from an average of 1600 m at the fault to 2 km approximately 1 km downstream of the fault. Average width for the entire mapped system is 1700 m. The channel-belt crosses the central portion of the fault at a depth of about 920 m and is displaced 44 m leading to an offset ratio of 5.1%.

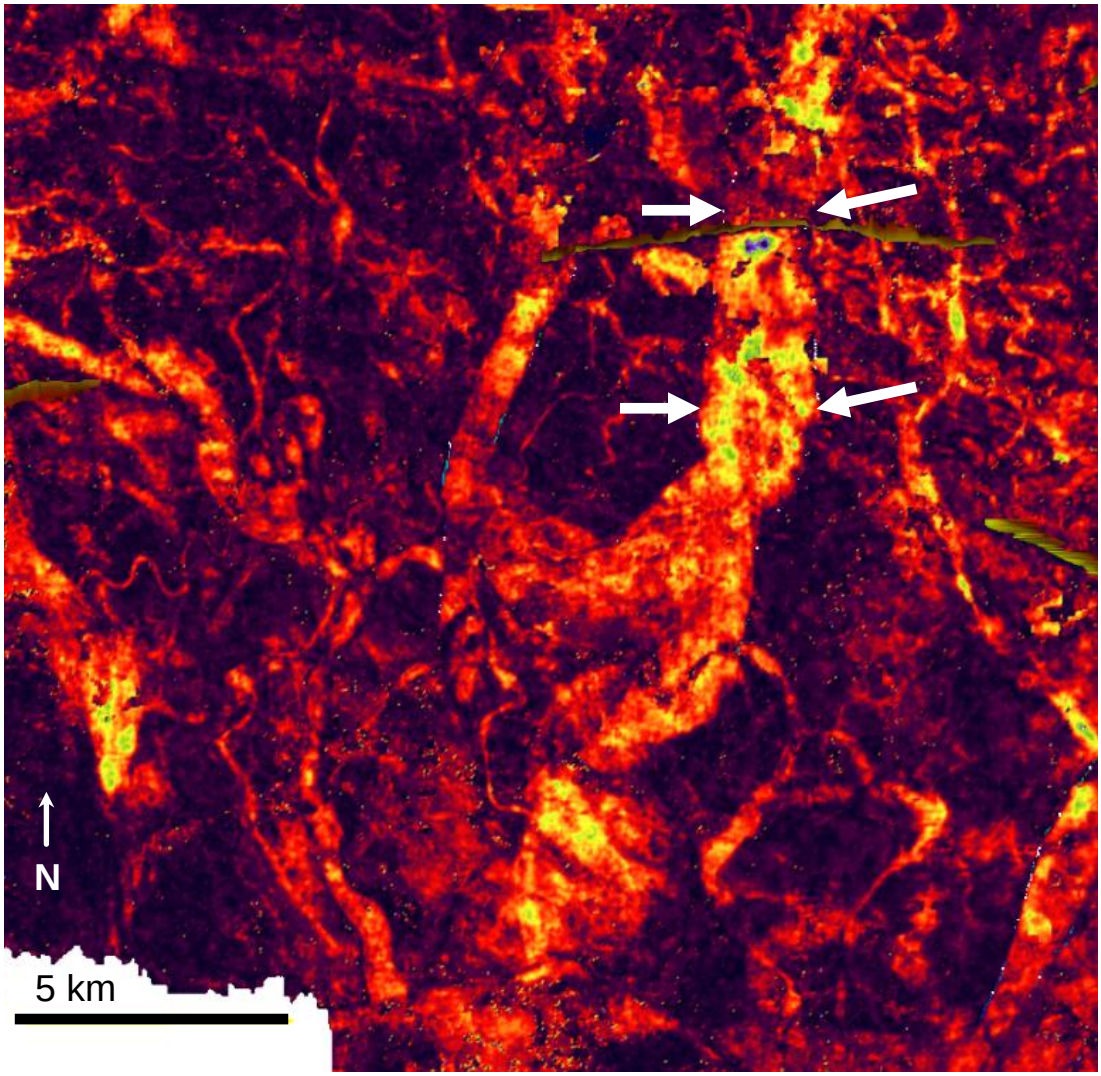

Figure 4.10: Example H, a Pliocene channel-belt. View is from directly overhead with sweetness attribute shown. Hotter colors indicate higher sweetness. The north set of arrows points to the fault with the channel-belt imaged as the high sweetness area between both sets of arrows.

4.2.9 Channel-belt reorientation vs. offset ratio

A plot of reorientation angle (equal to the angle of the channel-belt away from perpendicular to the strike of the fault of the upstream side minus the downstream side) versus the offset ratio (equal to the displacement of the channel-belt due to the fault divided by depth to the fault) shows a trend of increasing reorientation with increasing offset ratio (Fig. 4.11). The high offset ratio of 7% for one channel-belt is due to offset across two nearby faults, which leads to a greater offset ratio than typical.

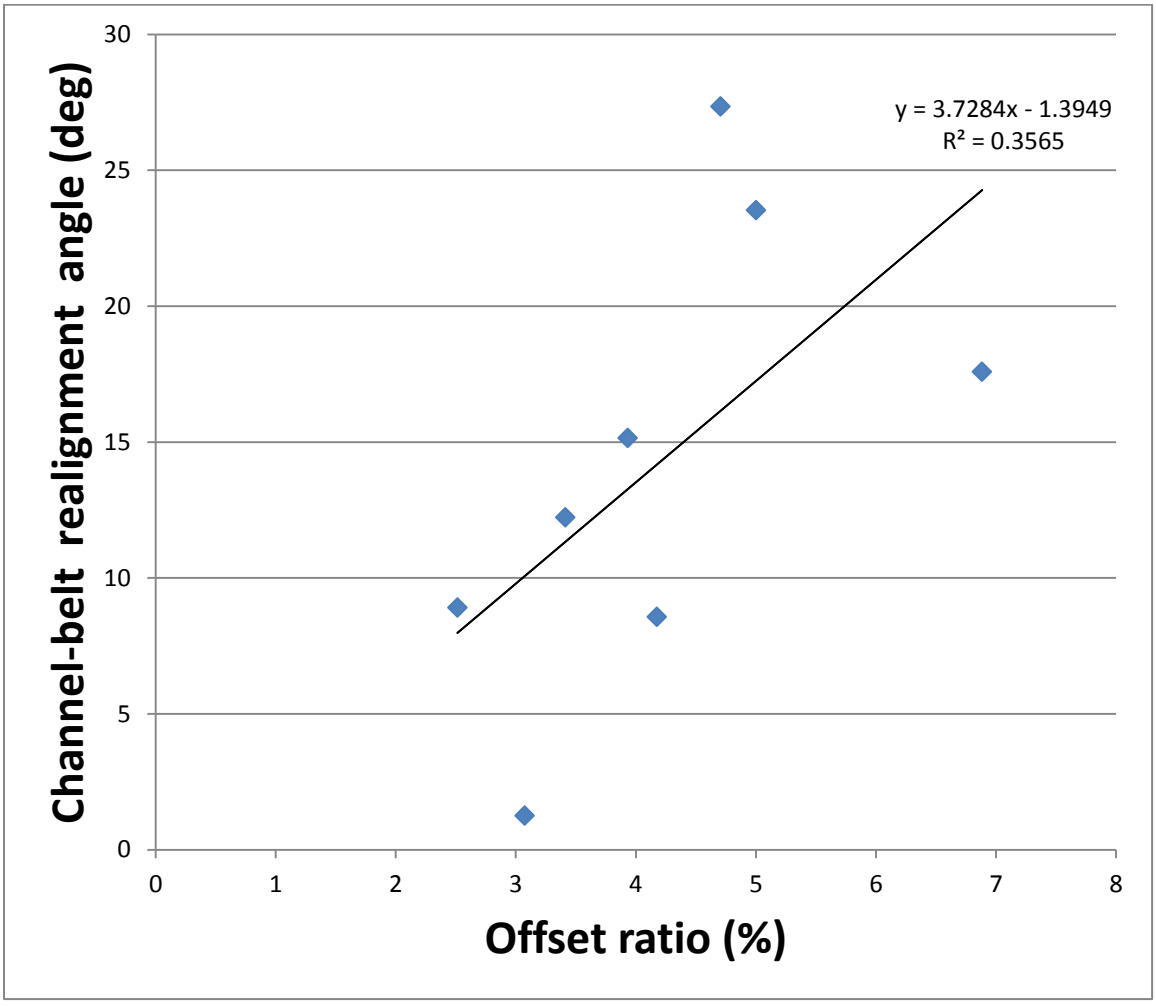

Figure 4.11: Degree of channel-belt realignment by faults as a function of the fault offset ratio.

4.3 Discussion

In general, when a channel-belt emerges downstream of a fault, it is oriented roughly perpendicular to the strike of the fault. This has been demonstrated for 7 channel-belts that intersect faults. These channel-belt systems have widths ranging from about 1.7 km to 3.3 km. In contrast, small channels (those with widths < 1 km) are rarely affected by faults. For over 50 examples of small channels within the dataset, only 2 are clearly redirected by faults. In addition, the small channels that are influenced by faults are not affected in the same way as channel-belts. Instead of an orientation perpendicular to the strike of the fault, as in channel-belts, small channels appear directed parallel to the strike of the fault along the zone of greatest fault displacement.

The sensitivity of fluvial stratigraphy to faulting is interpreted mainly as a function of faulting timescale versus avulsion timescale. Long term (~ 10^5 yr) vertical displacement rates for faults in this dataset are on the order of 10^{-2} mm/yr (George, 2008). However, recent short-term displacement rates for these same faults can be significantly higher. For two faults within the survey bounds, Gagliano (2003) reported displacements of up to 1.4 m over a two year time period. Rationalizing the short and long-term displacement rates on these same faults leads to a characteristic recurrence interval for punctuated, geologically instantaneous faulting on the order of 10^4 to 10^5 years (Fig. 4.12). If a fluvial system avulses more frequently than this, it is unlikely to be affected by faulting. While information on common avulsion frequencies for the late Miocene to Pliocene period studied is not available, avulsion frequencies ranging from 500 years to 5000 years have been found for Holocene channels and delta lobes (Tornqvist, 1994).

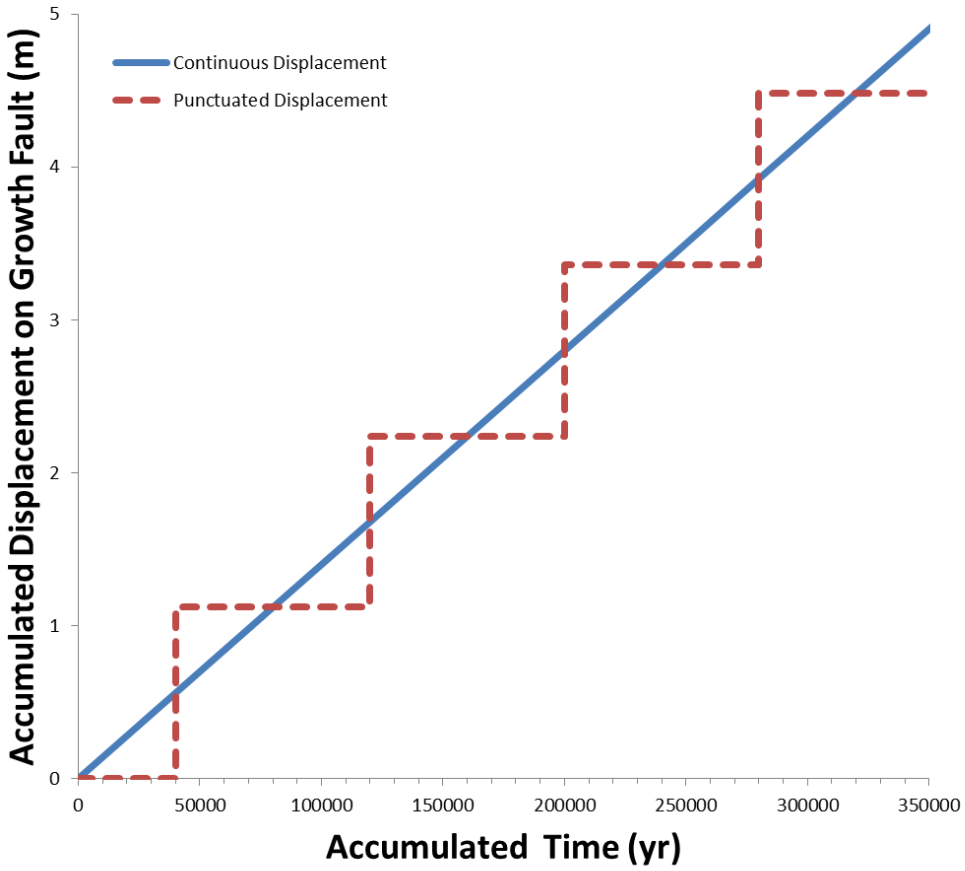

Figure 4.12: Illustration of continuous fault displacement (blue line) with a rate of 0.014 mm/yr versus punctuated displacement (red line) with an infrequently occurring ~ 1 m displacement.

Channel-belts are interpreted to be longer lived features than small channels and as a result are less likely to avulse than small fluvial systems. These channel-belts are interpreted to be more likely to experience faulting events than the smaller channels because of their lower mobility and so are more likely to be influenced by faults. The few small channels that are directed by faults most likely experienced a significant faulting event prior to avulsing.

Any alteration of fluvial orientation across a fault can be interpreted as a function of the length scale for enhanced subsidence with distance from a fault (Fig. 4.13) and the channel or channel-belt width. Fault induced subsidence is highest at the fault and decreases to zero at some distance from the fault. This length scale tends to be on the order of a few hundred meters for faults in this dataset. The width of channel-belt systems can be over an order of magnitude larger than the length scale of fault displacement; because of this, channel-belts

appear to be too large to be carried along the hangingwall of faults and instead emerge downstream oriented perpendicular to the fault. The mechanism for this arrangement has not been identified, but the configuration likely represents a steepest line of decent across the faulted surface. Valley systems can be tens of kilometers wider than the width of growth faults and appear to be too large to be affected by fault displacement events. Small channels, with widths similar to or less than the fault displacement length, do have the potential to be carried along the hangingwall of the fault if they experience a faulting event before avulsing.

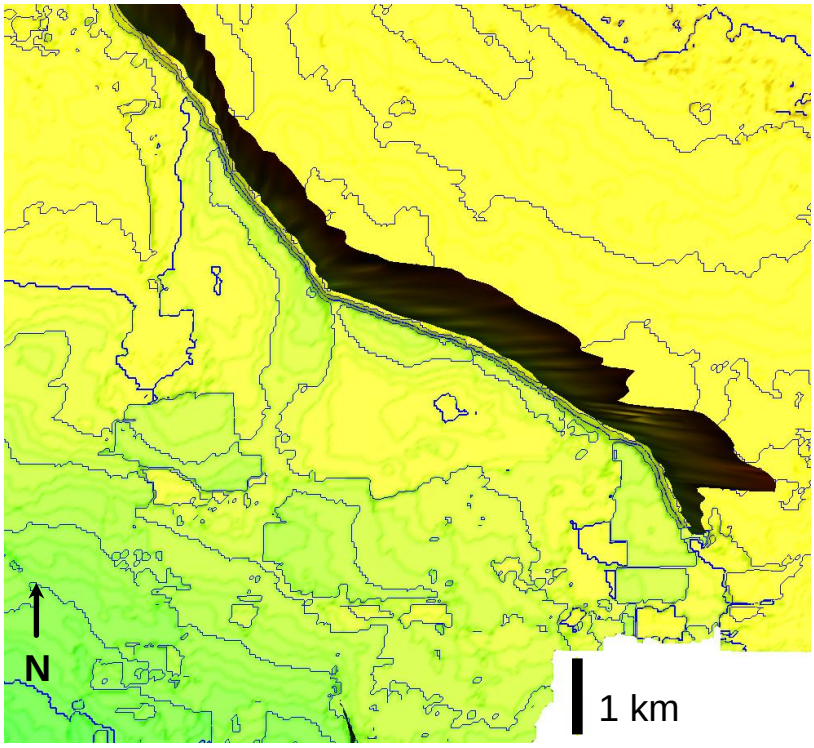

Figure 4.13: Time map of surface around a fault with a 16 ms contour interval. The zone of enhanced, fault-created subsidence decreases to zero within ~ 500 m of the fault. Yellows are shallowest parts of the mapped horizon.

In large scale half-graben extensional settings, the subsidence length scale can be orders of magnitude greater than channel-belt width and so channel-belts are commonly carried along the subsidence maximum. In the dataset used for this study, channel-belts are much wider than fault displacement lengths so the traditional model is not appropriate. Fault displacement length

scale, fluvial mobility, and channel width emerge as fundamental controls on the effectiveness and style of fault influence on fluvial stratigraphy.

4.4 Conclusions

1) On the hangingwall side of growth faults, the orientation of channel-belts appears to be affected by faulting. When a channel-belt approaches a fault at an oblique angle to the strike of the fault, the channel-belt tends to emerge downstream of the fault roughly perpendicular to the strike of the fault.

2) This channel-belt redirection by growth faults is loosely correlated with the offset ratio of the channel-belt. As offset ratio increases, the redirection of the channel-belt course appears to increase. However, if a channel-belt already approaches a fault close to perpendicular to the strike of the fault, realignment and apparent fault control will be low even with a high offset ratio.

3) The potential for growth fault influence on fluvial stratigraphy is related to the relative timescales of avulsion and faulting. Channel-belts are long lived features with avulsion timescales longer than faulting timescales. Channel-belts are more likely to be influenced by faults than small channels with higher avulsion frequencies.

4) The style of fault control is dependent on the width of the fluvial system. The few small channels that are affected by faults are directed along the hanging wall of the fault. This is not seen in larger systems. Instead, channel-belt systems are directed perpendicular to the strike of the fault. This is likely a function of the fault displacement length compared to the width of the channel or channel-belt. Fluvial systems with small ratios (low channel width and high displacement length) are more likely to be steered along the hanging wall of the fault than perpendicular to the fault.

Chapter 5: Summary

5.1 Conclusions and implications

This work provides a window into the ancient Mississippi River Delta. Late Miocene to Pliocene fluvial stratigraphy is shown to be highly variable with distinct planform styles and a range of geometries that spans an order of magnitude in thickness and several orders of magnitude in width. The variety of styles can be related to variations in sea-level, with a fall in sea-level resulting in valleys that are sometimes seen to incise into deposits of distributive channel networks that formed during an earlier highstand. Though there is certainly heterogeneity within fluvial fill, deposits can be generalized as low impedance, low gamma ray, high porosity sands. Taken as a whole, the late Miocene to Pliocene interval is remarkably sandy with a conservative estimate of 40% sand content. The repetitive nature of changes in fluvial style leads to a characteristic seismic-stratigraphic interval that measures the separation in space or time between the major fluvial events. This interval is very close to the average valley thickness and appears to represent a fundamental filtering of stratigraphy in this dataset.

Fluvial systems do not exist in isolation and interact with and are affected by other elements in the landscape. Inherited topography as well as growth fault activity can affect the course of rivers. In particular, spatially varying subsidence created by growth faults has the potential to cause significant redirection of channel planform orientation for relatively large channel-belt systems. Smaller systems, because of their high avulsion potential compared to larger channel-belt systems, are generally unaffected by infrequent displacement events along growth faults.

Hydrocarbon exploration in fluvial reservoirs may often rely on spatially limited data, and accurate assumptions about fluvial planform and geometry are valuable. This work provides dimensional specifics for dozens of fluvial systems in the late Miocene to Pliocene Mississippi River Delta. As petroleum companies are very active in the greater Gulf of Mexico basin, this work may provide useful analogues for exploration targets. Additionally, because growth faults can create structural traps, an understanding of the dynamic between faults and fluvial systems may allow more accurate predictions to be made concerning reservoir potential near faults.

The relationship between faults and rivers is also of interest to the civil engineer. Kim et al. (2009) discussed the feasibility of creating new land by cutting Mississippi River levees and opening flow to parts of the Mississippi River Delta. Growth faults are common in the area and knowledge of the ways in which sediment pathways may be affected by growth faults is important in engineering the creation of this new land.

3D seismic data has been called a geological 'Hubble' (Cartwright and Huuse, 2005), allowing geoscientists to visualize and explore significant portions of the subsurface in relatively high detail. The tools of 3D seismic geomorphology allow the interpreter to take advantage of the ways that even small changes of impedance within a 3D seismic volume can indicate discrete depositional systems. When integrated with other geological data (e.g., well logs, inversions, biostratigraphy), 3D seismic can provide a particularly potent medium for exploring subsurface stratigraphy. This work illustrates the potential for 3D seismic data and the techniques of 3D seismic geomorphology to provide a detailed, sometimes spectacular documentation of paleo-rivers as well as the usefulness of this data towards the goal of unraveling some of the complexities of fluvial stratigraphy.

References

Abreu, V. S., & Anderson, J. B. (1998). Glacial Eustasy During the Cenozoic: Sequence Stratigraphic Implications. *AAPG Bulletin, 82*(7), 1385-1400.

Alexander, J., & Leeder, M. R. (1987). Active tectonic control on alluvial architecture. *Recent Developments in Fluvial Sedimentology, Edited by Frank G. Ethridge, Romeo M. Flores, and Michael D. Harvey, 39*, 243-252.

Bridge, J. S., & Leeder, M. R. (1979). A simulation model of alluvial stratigraphy. *Sedimentology 26*, 617-644.

Bridge, J. S., & Tye, R. S. (2000). Interpreting the Dimensions of Ancient Fluvial Channel Bars, Channels, and Channel Belts from Wireline-Logs and Cores. *AAPG Bulletin, 84*(8), 1205-1228.

Brown, A. R. (2004). Interpretation of three-dimensional seismic data. 6th ed. *American Association of Petroleum Geologists and the Society of Exploration Geophysicists*.

Cartwright, J., & Huuse, M. (2005). 3D seismic technology: the geological 'Hubble'. *Basin Research, 17*(1), 1-20.

DeCelles, P. G. (1986). Sedimentation in a tectonically partitioned, nonmarine foreland basin: The Lower Cretaceous Kootenai Formation, southwestern Montana. *Geological Society of America Bulletin*, 97, 911-931.

Gagliano, M. S., Burton Kemp III, E., Wicker, K. M., Wiltenmuth, K. S., & Sabate, R. W. (2003). Neo-Tectonic Framework of Southeast Louisiana and Applications to Coastal Restoration. *GCAGS/GCSSEPM Transactions*, 53, 262-276.

Galloway, W. E., Bebout, D. G., Fisher W. L., Cabrera-Castro,R., Lugo-Rivera, J. E., and Scott, T. M. (1991a). Cenozoic, *in* A. Salvador, ed., *The geology of North America: the Gulf of Mexico basin, v. J: Boulder, Colorado, Geological Society of America*, p. 245-324.

George, T. (2008). 3-D Seismic Evaluation of Fault Control on Quaternary Subsidence Patterns, Rates, and Related Surface Morphology in Southeastern Louisiana*. MS Thesis*, 168.

Gibling, M. R. (2006). Width and Thickness of Fluvial Channel Bodies and Valley Fills in the Geological Record: A Literature Compilation and Classification. *Journal of Sedimentary Research, 76*(5), 731-770.

Hacikoylu, P., J. Dvorkin, and G. Mavko. (2006). Resistivity-velocity transforms revisited. *The Leading Edge*, 25, 1006-1009.

Hampson, D. P., Schuelke, J. S., & Quirein, J. A. (2001). Use of multiattribute transforms to predict log properties from seismic data. *Geophysics, 66*(1), 220-236.

Hart, B. S. (2008). Channel detection in 3-D seismic data using sweetness. *AAPG Bulletin, 92*(6), 733-742.

Kim, W., Mohrig, D., Twilley, R., Paola, C., & Parker, G. (2009). Is it feasible to build new land in the Mississippi River Delta? *EOS, Transactions, American Geophysical Union*, 90(42), 373-374.

Kim, W., Sheets, B. A., & Paola, C. (2010). Steering of experimental channels by lateral basin tilting. *Basin Research, 22*(3), 286-301.

Krynine, P. D. (1948). The Megascopic Study and Field Classification of Sedimentary Rocks. *The Journal of Geology, 56*(2), 130-165.

Mack., G. H., Leeder, M. R. (1999). Climatic and tectonic controls on alluvial-fan and axial-fluvial sedimentation in the Plio-Pleistocene Palomas half graben, southern Rio Grande rift *Journal of Sedimentary Research*, 69 (1999), pp. 635–652

Mack, G. H., & Seager, W. R. (1990). Tectonic control on facies distribution of the Camp Rice and Palomas Formations (Pliocene-Pleistocene) in the southern Rio Grande rift. *Geological Society of America Bulletin, 102*(45-53).

Mackey, S. D., & Bridge, J. S. (1995). Three-dimensional model of alluvial stratigraphy: theory and application. *Journal of Sedimentary Research, B65*(1), 7-31.

Maynard, J. R. (2006). Fluvial response to active extension: evidence from 3D seismic data from the Frio Formation (Oligo-Miocene) of the Texas Gulf of Mexico Coast, USA. *Sedimentology, 53*(3), 515-536.

Maynard, J. R., Feldman, H. R., & Alway, R. (2010). From Bars to Valleys: The Sedimentology and Seismic Geomorphology of Fluvial to Estuarine Incised-Valley Fills of the Grand Rapids Formation (Lower Cretaceous), Iron River Field, Alberta, Canada. *Journal of Sedimentary Research, 80*(7), 611-638.

Miall, A. D. (1988). Reservoir heterogeneities in fluvial sandstones: lessons from outcrop studies, *AAPG Bulletin,* 72(31), 682-697.

Miall, A. D. (1994). Reconstructing fluvial macroform architecture from two-dimensional outcrops: examples from the Castlegate Sandstone, Book Cliffs, Utah. *Journal of Sedimentary Research,* B64, 146-158.

Miller K.G., Kominz M.A., Browning J.V., Wright J.D., Mountain G.S., Katz M.E., Sugarman P.J., Cramer B.S., Christie-Blick N., Pekar S.F. (2005). The Phanerozoic record of global sea-level change: *Science*, v. 310, p. 1293–1298

Mohrig, D., Heller, P. L., Paola, C., & Lyons, W. J. (2000). Interpreting avulsion process from ancient alluvial sequences: Guadalope-Matarranya system (northern Spain) and Wasatch Formation (western Colorado). *Geological Society of America Bulletin, 112*(12), 1787-1803.

Mohrig, D., Straub, K. M., & De la Rosa Illescas, A. C. (2010). When does spatial variation in subsidence rate influence the positioning of channels within Quaternary strata of the Mississippi River Delta? *AAPG Annual Convention Session: Autogenic and Allogenic Controls on Sedimentary Successions: Modern and Ancient, Clastic and Carbonate*.

Muto, T., Steel, R. J., & Swenson, J. B. (2007). Autostratigraphy: A Framework Norm for Genetic Stratigraphy. *Journal of Sedimentary Research, 77*(1), 2-12

Neal, J., & Abreu, V. (2009). Sequence stratigraphy hierarchy and the accommodation succession method. *Geology, 37*(9), 779-782.

Nelson, T. H. (1991). Salt tectonics and listric-normal faulting, in Salvador, A., ed, *The Gulf of Mexico Basin. Geological Society of America, The Geology of North America*, v. J, 73-89

Partyka, G.A., Gridley, J.M., and Lopez, J. (1999). Interpretational Applications of Spectral Decomposition in Reservoir Characterization, *The Leading Edge*, vol. 18, No. 3, 353-360.

Peakall, J. (1998). Axial river evolution in response to half-graben faulting: Carson River, Nevada, U.S.A. *Journal of Sedimentary Research*, 68, 788-799.

Peakall, J., Leeder, M. R., Best, J., & Ashworth, P. (2000). River response to lateral ground tilting: a synthesis and some implications for the modeling of alluvial architecture in extensional basins. *Basin Research*, 12, 413-424.

Posamentier, H. W. (2001). Lowstand alluvial bypass systems: Incised vs. unincised. *AAPG Bulletin, 85*(10), 1771-1793.

Reynolds, A. D. (1999). Dimensions of Paralic Sandstone Bodies. *AAPG Bulletin, 83*(2), 211-229.

Salvador, A. (1991). Origin and development of the Gulf of Mexico basin, in Salvador, A., ed., *The Gulf of Mexico Basin. Geological Society of America, The Geology of North America*, v. J, 389-444

Straub, K. M., Paola, C., Mohrig, D., Wolinsky, M. A., & George, T. (2009). Compensational Stacking of Channelized Sedimentary Deposits. *Journal of Sedimentary Research, 79*(9), 673-688.

Taha, Z. P., & Anderson, J. B. (2008). The influence of valley aggradation and listric normal faulting on styles of river avulsion: A case study of the Brazos River, Texas, USA. *Geomorphology, 95*(3-4), 429-448.

Tingdahl, K. M. and De Rooij, M. (2005). Semi-automatic detection of faults in 3D seismic data. *Geophysical Prospecting*, 53: 533–542

Tornqvist, T. E. (1994). Middle and late Holocene avulsion history of the River Rhine (Rhine-Meuse delta, Netherlands). *Geology, 22*, 711-714.

Wood, L. J. (2007). Quantitative Seismic Geomorphology of Pliocene and Miocene Fluvial Systems in the Northern Gulf of Mexico, U.S.A. *Journal of Sedimentary Research, 77*(9), 713-730.

Zaitlin, B. A., Dalrymple, R. W., & Boyd, R. (1994). The stratigraphic organization of incised-valley systems associated with relative sea-level change. *Incised-valley systems: origin and sedimentary sequences, SEPM special publication No. 51*, 45-60.

Zeng, H. (2010). Stratal slicing: Benefits and challenges. *The Leading Edge,* September 2010, 1040-1047.

Zeng, H., & Hentz, T. F. (2004). High-frequency sequence stratigraphy from seismic sedimentology: Applied to Miocene, Vermilion Block 50, Tiger Shoal area, offshore Louisiana. *AAPG Bulletin, 88*(2), 153-174.

Strata Software Documentation, Theory of the Strata Program. (1999). *CGG Veritas*.

Emerge Software Documentation. (2006). *CGG Veritas*.